Fall 2013

Peridynamic Modeling of Coupled Mechanical Deformations and Transient Flow in Unsaturated Soils

Rami Jabakhanji
Purdue University

Graduate School ETD Form 9
(Revised 12/07)

PURDUE UNIVERSITY
GRADUATE SCHOOL
Thesis/Dissertation Acceptance

This is to certify that the thesis/dissertation prepared

By Rami Jabakhanji

Entitled
Peridynamic modeling of coupled mechanical deformations and transient flow in unsaturated soils.

For the degree of Doctor of Philosophy

Is approved by the final examining committee:

Rabi Mohtar Chair	Antonio Bobet
Indrajeet Chaubey	Venkatesh Merwade

To the best of my knowledge and as understood by the student in the *Research Integrity and Copyright Disclaimer (Graduate School Form 20)*, this thesis/dissertation adheres to the provisions of Purdue University's "Policy on Integrity in Research" and the use of copyrighted material.

Approved by Major Professor(s): Rabi Mohtar

Approved by: Bernard Engel 10/07/2013
Head of the Graduate Program Date

PERIDYNAMIC MODELING OF COUPLED MECHANICAL DEFORMATIONS AND TRANSIENT FLOW IN UNSATURATED SOILS

A Dissertation

Submitted to the Faculty

of

Purdue University

by

Rami Jabakhanji

In Partial Fulfillment of the

Requirements for the Degree

of

Doctor of Philosophy

December 2013

Purdue University

West Lafayette, Indiana

To my parents, Nibal and Ibrahim, and to Ghenwa

ACKNOWLEDGMENTS

I would like to thank my advisor, Professor Rabi Mohtar, and my committee members, Professors Antonio Bobet, Indrajeet Chaubey and Venkatesh Merwade for their patience and support during this project. Rabi's excitement and honest dedication to making this world a better place is humbling and inspiring. I will always be grateful for our animated discussions, his unwavering support and the space he has given me to freely explore and push my limits. Antonio's help and guidance were essential for the completion of this project, it was a joy working with him and I am very grateful for his mentorship, while Indrajeet's scientific rigor kept me on my toes. I am also very grateful for Venkatesh's counsel during a very critical phase.

I am extremely grateful to Professor Sabre Kais for giving me access to his lab computing resources at the Rosen Center for Advanced Computing. This project would not have been possible without his help. Thank you, too, to Julie Jesiek for being the rational voice in the lab and her help and assistance in my project.

Thank you to Charles Armstrong, Gail Biberstine, Barbara Davies, Constance Mcmindes, Rebecca Peer and Carol Weaver for being so welcoming, kind and supportive during my years at Purdue, and for making Indiana my second home.

Thank you to Mary Schweitzer for the friendship, wise and honest advice, and for always looking out for me. I love you dearly. Thank you as well to Ghadir Haikal for your encouragement and support, and for the hours of fun and laughter I shared with you and Mary.

Thank you to my fellow graduate students, Majdi, Mohamad, John, Margaret, Bassel and Amjad for their companionship and their willingness to lend a listening ear to my occasional rants. A big thank you to Kingsly Ambrose for the countless cigarettes breaks, motivating discussions and his ever-calm disposition.

Thank you to Emily Sanders for the good days and the bad days that we shared. You were a special part of my years at Purdue and in Lafayette, and you still are a special part of my life now.

Thank you to Abrar Hammoud, for your friendship, support, your delicious meatloaf, and for putting up with my annoying self throughout.

A very big thank you to my friends, Madiha, Bashar, Nada, John, Lana, Dia, Paula, Yara, Helena, Lara, Haitham, Samia, Hatem, Qutayba, Rami, Roger, and Youssef. Their love and friendship have, paradoxically, made it tolerable to be away from them and away from home and continue to sustain me.

Thank you to Mounir Mabsout, my Masters adviser and my first mentor, who gave me my first taste of research and teaching, and who has continued to encourage me on my long journey since.

Thank you to Apkar Vania Apkarian and to Dante Chialvo, my mentors at Northwestern University. I am grateful for the opportunity Vania gave me to experience first hand serious scientific research. Few people have had as great an impact on me as Dante has, and I am forever indebted to him for teaching me how to ask big questions simply.

A very special thank you to my parents, Ibrahim and Nibal, to my sister Ursula, and to my aunt Murad for their unconditional support and infinite encouragement. Their faith in me has been a source of strength and constant motivation. I am grateful to my father for encouraging and nurturing my curiosity, to my mother for the endless evenings she spent tutoring me and helping with my homework, and to my sister for her love and for the support she gave my parents during the years when I was away from home.

Finally, I would like to express my eternal gratitude to Ghenwa, my love, my friend and my inspiration. I would not have embarked on, nor finished, this project without her unconditional support and encouragement, and her infinite patience with my bad moods. She brings peace and order to my mind, and passion to my soul.

TABLE OF CONTENTS

Page

Page

LIST OF TABLES

LIST OF FIGURES

Figure Page

Figure Page

ABSTRACT

Jabakhanji, Rami Ph.D., Purdue University, December 2013. Peridynamic Modeling of Coupled Mechanical Deformations and Transient Flow in Unsaturated Soils. Major Professor: Rabi Mohtar.

A coupled peridynamic model for mechanical deformations and transient moisture flow in unsaturated soils is developed. The model is capable of simulating the emergence and evolution of cracks triggered by volumetric strains in the soil which are associated with changes in moisture content. The development of our model is motivated by the need for a tool to analyze and evaluate the impact of dessication cracks on the movement of moisture and the mechanical properties of soils at the field scale. The model is based on the peridynamic reformulation of elasticity proposed by Silling for simulating the deformation of bodies with evolving discontinuities, where the classic continuum mechanics differential equation of motion is replaced by a non-local, derivative free, functional integral. The absence of spatial derivatives leads to a model that is valid everywhere in the simulation domain, including points of discontinuities. Following a similar approach, we developed a moisture flow model where the classic Richard's differential equation for moisture flow in soils is replaced by a non-local, derivative free, functional integral. The flow model is capable of simulating transient moisture flow in homogeneous or heterogeneous soils with isotropic or anisotropic hydraulic conductivities. The coupled model is obtained by combining the developed moisture flow model with the peridynamic model for solid mechanics. The validation of the flow model is carried out by comparing the results of simulations of various flow scenarios using the peridynamic formulation as well as the classic Richard's equation. In order to validate the coupled model, a simulation

of a laboratory restrained ring experiment is performed, and the results are compared to the laboratory results.

CHAPTER 1. INTRODUCTION

1.1 Research justification

Naturally occurring soils, especially fine-textured ones, may exhibit shrinking and swelling behavior (Davidson and Page, 1956, Dinka, 2012). These soils tend to swell when their moisture content increases, and shrink when it decreases. At the field scale, this behavior leads to tensile stresses that may exceed the soil's failure limit and trigger the formation and evolution of cracks during drying phases. Cracks may in turn close during infiltration phases when the soil becomes wetter and swells (Chertkov, 2002, Greco, 2002, Jarvis, 2007).

This phenomenon has a wide spectrum of engineering, environmental, agricultural, and hydrological impacts. For example, dessication cracks developing at the surface of a slope may trigger the onset of a landslide. If they develop in the core of an earth dam, cracks act as preferential moisture flow paths, increasing the moisture content of the dam and, with it, the pore water pressure which eventually leads to its failure (Wang et al., 2007). Clay barriers used in landfills and nuclear waste disposal sites are also subject to dessication cracking which reduces the barrier's containment effectiveness (Albrecht and Benson, 2001, Dixon et al., 2002) with potentially very serious environmental and public safety impacts.

Dessication cracks have also environmental and agricultural impacts. The movement of moisture and solutes into and within the soil increases due to the presence of these cracks that act as preferential pathways for rapid water movement to deeper layers (Greve et al., 2010, Kosmas et al., 1991, Harris et al., 1994, Lin and Mcinnes, 1995, **?**). This rapid movement lowers the effectiveness of irrigation (Smith et al., 2005) and causes fast seepage of nutrients and pesticides

away from the plants into deeper layers. This reduces the contaminants' residence time in the unsaturated zone where they are usually absorbed by the plants and degraded by bacteria, and increases the probability of ground water and/or surface water contamination, depending on the relief.

In addition, dessication cracks can have a dramatic effect on processes of surface water movement and flood dynamics by altering the partitioning of rainfall between infiltration and runoff, which is an important issue to consider when modeling and forecasting flood events.

Currently, there are several attempts to address the modeling of some aspects of soil dessication cracking and moisture flow in cracked soil. Some moisture flow models indirectly account for the impact of cracks on flow. These models lump the dessication cracks with all other sources of preferential flow such as worm and decaying roots channels and represent the soil as a system of two uniform media with different porosities. The first porosity is that of the soil matrix, and the second is that of the preferential flow channels (Gerke and van Genuchten, 1993, Germann and Beven, 1981a, Beven and Germann, 1981, Germann and Beven, 1981b, Genuchten et al., 1976, Genuchten et al., 1977b, Genuchten et al., 1977a). Model parameters are obtained using homogenization and volume averaging techniques and require extensive field calibration that depends on the process of interest, whether it is moisture flow or solute transport. This leads to models that cannot capture the horizontal variability of the variables of interest introduced by crack networks and, although they constitute good forecast tools, are not suitable to study explicitly the effects of dessication cracks.

Other models attempt to explicitly model the effects of dessication cracks on moisture flow (Bronswijk, 1988b, Bronswijk, 1988a, Braudeau et al., 2009, Braudeau and Mohtar, 2009, Singh et al., 2012). They go about it by calculating the moisture content dependent total crack volume per layer from the difference between the volume of the soil at saturation and its volume at the current moisture

content given by the soils shrinkage curve, disregarding any kinematic constraints in the field and tensile strength capacity that could resist the deformation and cracking of the soil. Using the calculated total crack volume, and assuming a certain crack geometry, rectangular or triangular, the models calculate the depth of the crack and its associated surface area, which is now part of the infiltration, or evaporation, boundary. However, these models also lack the ability to capture the morphology of the crack network which is essential for accurately assessing the cracks surface area as different number of cracks per layer could lead to different surface area values for the same total volume.

From a solid mechanics perspective, models using the discrete element method (DEM) (Peron et al., 2009, Amarasiri and Kodikara, 2011), linear elastic fracture model (LEFM) (Ayad et al., 1997, Wang et al., 2007), and the cohesive crack method (Amarasiri and Kodikara, 2011, Amarasiri and Kodikara, 2013) have been proposed for modeling dessication cracks. However, these models require extensive parameter calibration and, with the exception of DEM, require elaborate failure criteria and separate crack initiation and propagation laws, in addition to special numerical techniques during implementation such as the discrete crack approach, the smeared crack approach, and the extended finite element method (X-FEM) (Bouchard et al., 2003, Borst, 1997, Belytschko and Black, 1999).

Available research into modeling crack network morphology mainly uses imaging techniques to capture the evolution of the surface cracks network with moisture content in laboratory tray specimen. Network characteristics are captured using statistical distribution models of key parameters such as crack length per unit area, crack width, bifurcation angle, surface shrinkage, and cell area (Suits et al., 2009, Lakshmikantha et al., 2012), or using Minkowski numbers and Minkowski functions (Vogel et al., 2005b, Vogel et al., 2005a). Some experiments in characterizing the evolution of field crack networks and separating matrix for preferential flow using optical photography and latex resin casts have also been done (Abou Najm et al., 2010, Sanders et al., 2012).

Although all this research has contributed to our understanding of cracking and moisture flow in soils prone to dessication cracking, they remain mainly single process oriented, where the impact of the second process is incorporated either indirectly or very conceptually.

However, because of the potentially significant engineering, environmental, agricultural and hydrological impacts of dessication cracking, and the interdependence between processes of crack formation and moisture flow, and in order to better understand the mechanisms of formation and evolution of these types of cracks, and to quantify their impacts, there is a need to develop a model that is capable of simulating processes of solid mechanics and fracture as well as moisture flow in a soil medium in a coupled manner. However, neither the Richards Equation, used to describe the movement of moisture in variably saturated soils, nor the classic continuum mechanics formulation for solid mechanics are good candidates for this model. Both are partial differential equations with spatial derivative terms that are undefined at points of spatial discontinuities, and both will fail when cracks, which are points of singularities, form and evolve during a simulation.

I want to offer a potential solution by deriving an alternative formulation of the flow problem, similar to the reformulation of the theory of elasticity for solid mechanics presented by Silling (Silling, 2000, Silling et al., 2010). I propose a model that replaces the classic, local, continuum mechanics formulation, by a nonlocal integral functional, free of spatial derivatives and valid even in the presence of evolving discontinuities, where the parameters are measurable or are related to measurable quantities.

1.2 Research objectives

I have set two main objectives for the following research. The first objective is to derive a model for transient moisture flow in unsaturated soils applicable

to situations where the soil medium is prone to the development and evolution of cracks leading to spatial discontinuities. The model's formulation is non-local and analogous to the peridynamic model for solid mechanics (Silling, 2000, Silling et al., 2010). It is based on the hypothesis that moisture flow in a soil medium as observed at a given scale can be conceptualized as a phenomenon emerging from pairwise exchanges of moisture driven by the difference in hydraulic head between pairs of material points in a continuous domain that are within a set distance of each other.

This objective is met in two phases. In the first phase, I will develop and evaluate the model in one dimension for homogeneous soils. In the second phase, I will extend the model to two dimensions and to cases involving heterogeneous and/or anisotropic soils.

The second objective is to develop a model that will simultaneously model moisture flow processes and mechanical deformation and cracking processes in unsaturated soils. In the proposed model, the changes in the soil volume due to changes in the moisture content will be taken into account when calculating the mechanical deformations and checking for crack formation. This will automatically feed back into the flow calculations, altering the flow process. This will be achieved by coupling the peridynamic moisture flow model, my first objective, with Silling's peridynamic model for solid mechanics.

1.3 Dissertation organization

The dissertation is organized into five chapters, including this introductory chapter. The peridynamic model for transient flow in unsaturated soil is the subject of chapters two and three. In Chapter 2, I present the model for problems in one dimension for homogeneous soils. This is extended to problems in two dimensions for anisotropic and heterogeneous soils in Chapter 3. The coupled

flow-deformation peridynamic model is discussed in Chapter 4. In the last chapter, Chapter 5, I summarize the research outcomes and offer concluding remarks.

Chapter 2 starts by presenting the concept of a peridynamic material model in general and its mechanism of moisture flow in a porous medium. The chapter progresses to the derivation of the peridynamic equation of the rate of change of the volumetric moisture content, the equivalent of the Richard's equation. This is followed by defining the quantity equivalent to the moisture flux in the classic continuum mechanics theory and deriving its equation in the peridynamic conceptual framework as well as deriving the equation relating the peridynamic hydraulic conductivity to the measurable classic hydraulic conductivity. I then move on to the numerical discretization and implementation, and validation of the model in one dimension. The validation exercise consists of simulating infiltration and drainage scenarios using the peridynamic model and a classic finite element implementation of the classic equations and comparing their results.

In Chapter 3, the model is extended to problems of transient flow in unsaturated, heterogeneous and anisotropic soils in two dimensions. The general peridynamic equation of the rate of change of the moisture content in two dimensions is derived. This is followed by defining and deriving expressions for the peridynamic equivalents of moisture flux and flow power. The expressions are then used in relating the peridynamic hydraulic conductivity to the classic and measurable quantity. I then move on to extend this relationship to the case of soils with anisotropic hydraulic conductivities, and to generalize the model to unsaturated and heterogeneous soils. In order to validate the proposed model, the peridynamic equations are discretized and a parallel numerical implementation is coded and used to simulate various moisture flow scenarios whose results are compared with results of classic simulations of the same scenarios. These scenarios consist of moisture redistribution in homogeneous soils for the cases of isotropic, as well as anisotropic hydraulic conductivities, and of moisture drainage

in heterogeneous soils, also for the cases of isotropic and anisotropic hydraulic conductivities.

Chapter 4 begins by introducing the peridynamic model for solid mechanics in general (Silling, 2000, Silling et al., 2010), and details the bond-based model specifically (Silling, 2000). The peridynamic equation of motion is derived, followed by the derivation of the special case of a homogeneous linear microelastic material. Next, the peridynamic expressions for elastic deformation energy density, and their usage in deriving the relationship between the peridynamic elastic modulus and the material Young's modulus, are derived for problems in one, two, and three dimensions. I also show analytically that at the limit of vanishing horizon the peridynamic model for linear microelastic materials converges to the classic formulation. This is followed by defining and deriving an expression for the peridynamic stress measure that is equivalent to the classic stress, and expanding the model to capture damage and cracking using the concept of material critical stretch (Silling, 2000, Silling et al., 2010, Foster, 2009). I then move on to describing the coupling between the moisture flow model developed in chapters two and three with Silling's peridynamic model for solid mechanics, and discuss its numerical implementation and incorporation into an available bond-based peridynamic modeling tool. The coupled model performance is tested by performing a two dimensional simulation of a soil restrained ring test and comparing the results with published results of the same test carried out in the laboratory (Abou Najm et al., 2009, Abou Najm, 2009).

1.4 References

Abou Najm, M., Mohtar, R. H., Weiss, J., and Braudeau, E. (2009). Assessing internal stress evolution in unsaturated soils. *Water Resources Research*, 45(5):n/a–n/a.

Abou Najm, M. R. (2009). Soil-water interaction: Lessons across scales. *ETD Collection for Purdue University*, pages 1–257.

Abou Najm, M. R., Jabro, J. D., Iversen, W. M., Mohtar, R. H., and Evans, R. G. (2010). New method for the characterization of three-dimensional preferential flow paths in the field. *Water Resources Research*, 46(2):n/a–n/a.

Albrecht, B. and Benson, C. (2001). Effect of desiccation on compacted natural clays. *Journal of Geotechnical and Geoenvironmental Engineering*, 127(1):67–75.

Amarasiri, A. and Kodikara, J. (2011). Use of material interfaces in DEM to simulate soil fracture propagation in mode i cracking. *International Journal of Geomechanics*, 11(4):314–322.

Amarasiri, A. L. and Kodikara, J. K. (2013). Numerical modeling of desiccation cracking using the cohesive crack method. *International Journal of Geomechanics*, 13(3):213–221.

Ayad, R., Konrad, J. M., and Soulié, M. (1997). Desiccation of a sensitive clay: Application of the model CRACK. *Canadian Geotechnical Journal*, 34(6):943–951.

Belytschko, T. and Black, T. (1999). Elastic crack growth in finite elements with minimal remeshing. *International Journal for Numerical Methods in Engineering*, 45(5):601–620.

Beven, K. and Germann, P. (1981). Water flow in soil macropores II. a combined flow model. *Journal of Soil Science*, 32(1):15–29.

Borst, R. D. (1997). Some recent developments in computational modelling of concrete fracture. *International Journal of Fracture*, 86(1-2):5–36.

Bouchard, P., Bay, F., and Chastel, Y. (2003). Numerical modelling of crack propagation: Automatic remeshing and comparison of different criteria. *Computer Methods in Applied Mechanics and Engineering*, 192(35–36):3887–3908.

Braudeau, E. and Mohtar, R. H. (2009). Modeling the soil system: Bridging the gap between pedology and soil–water physics. *Global and Planetary Change*, 67(1–2):51–61.

Braudeau, E., Mohtar, R. H., El Ghezal, N., Crayol, M., Salahat, M., and Martin, P. (2009). A multi-scale "soil water structure" model based on the pedostructure concept. *Hydrology and Earth System Sciences Discussions*, 6(1):1111–1163.

Bronswijk, J. (1988a). Effect of swelling and shrinkage on the calculation of water balance and water transport in clay soils. *Agricultural Water Management*, 14(1–4):185–193.

Bronswijk, J. (1988b). Modeling of water balance, cracking and subsidence of clay soils. *Journal of Hydrology*, 97(3–4):199–212.

Chertkov, V. Y. (2002). Modelling cracking stages of saturated soils as they dry and shrink. *European Journal of Soil Science*, 53(1):105–118.

Davidson, S. E. and Page, J. B. (1956). Factors influencing swelling and shrinking in soils. *Soil Science Society of America Journal*, 20(3):320–324.

Dinka, T. M. (2012). Review paper: Challenges and limitations in studying the shrink-swell and crack dynamics of vertisol soils. *Open Journal of Soil Science*, 02(02):82–90.

Dixon, D., Chandler, N., Graham, J., and Gray, M. N. (2002). Two large-scale sealing tests conducted at atomic energy of canada's underground research laboratory: The buffer-container experiment and the isothermal test. *Canadian Geotechnical Journal*, 39(3):503–518.

Foster, J. T. (2009). Dynamic crack initiation toughness: Experiments and peridynamic modeling. *ETD Collection for Purdue University*, pages 1–165.

Genuchten, V., Th, M., and Wierenga, P. J. (1976). Mass transfer studies in sorbing porous media i. analytical solutions. *Soil Science Society of America Journal*, 40(4):473–480.

Genuchten, V., Th, M., and Wierenga, P. J. (1977a). Mass transfer studies in sorbing porous media: II. experimental evaluation with tritium (3H2O). *Soil Science Society of America Journal*, 41(2):272–278.

Genuchten, V., Th, M., Wierenga, P. J., and O'Connor, G. A. (1977b). Mass transfer studies in sorbing porous media: III. experimental evaluation with 2,4,5-t. *Soil Science Society of America Journal*, 41(2):278–285.

Gerke, H. H. and van Genuchten, M. T. (1993). A dual-porosity model for simulating the preferential movement of water and solutes in structured porous media. *Water Resources Research*, 29(2):305–319.

Germann, P. and Beven, K. (1981a). Water flow in soil macropores i. an experimental approach. *Journal of Soil Science*, 32(1):1–13.

Germann, P. and Beven, K. (1981b). Water flow in soil macropores iii. a statistical approach. *Journal of Soil Science*, 32(1):31–39.

Greco, R. (2002). Preferential flow in macroporous swelling soil with internal catchment: Model development and applications. *Journal of Hydrology*, 269(3–4):150–168.

Greve, A., Andersen, M. S., and Acworth, R. I. (2010). Investigations of soil cracking and preferential flow in a weighing lysimeter filled with cracking clay soil. *Journal of Hydrology*, 393(1):105–113.

Harris, G., Nicholls, P., Bailey, S., Howse, K., and Mason, D. (1994). Factors influencing the loss of pesticides in drainage from a cracking clay soil. *Journal of Hydrology*, 159(1–4):235–253.

Jarvis, N. J. (2007). A review of non-equilibrium water flow and solute transport in soil macropores: Principles, controlling factors and consequences for water quality. *European Journal of Soil Science*, 58(3):523–546.

Kosmas, C., Moustakas, N., Kallianou, C., and Yassoglou, N. (1991). Cracking patterns, bypass flow and nitrate leaching in greek irrigated soils. *Geoderma*, 49(1–2):139–152.

Lakshmikantha, M., Prat, P. C., and Ledesma, A. (2012). Experimental evidence of size effect in soil cracking. *Canadian Geotechnical Journal*, 49(3):264–284.

Lin, H. and Mcinnes, K. (1995). Water-flow in clay soil beneath a tension infiltrometer. *Soil Science*, 159(6):375–382. WOS:A1995RE91500002.

Peron, H., Delenne, J., Laloui, L., and El Youssoufi, M. (2009). Discrete element modelling of drying shrinkage and cracking of soils. *Computers and Geotechnics*, 36(1–2):61–69.

Sanders, E. C., Abou Najm, M. R., Mohtar, R. H., Kladivko, E., and Schulze, D. (2012). Field method for separating the contribution of surface-connected preferential flow pathways from flow through the soil matrix. *Water Resources Research*, 48(4):n/a–n/a.

Silling, S. (2000). Reformulation of elasticity theory for discontinuities and long-range forces. *Journal of the Mechanics and Physics of Solids*, 48(1):175–209.

Silling, S., Lehoucq, R., Aref, H., and van der Giessen, E. (2010). Peridynamic theory of solid mechanics. In *Advances in Applied Mechanics*, volume Volume 44, pages 73–168. Elsevier.

Singh, J., Mohtar, R., Braudeau, E., Heathmen, G., Jesiek, J., and Singh, D. (2012). Field evaluation of the pedostructure-based model (kamel®). *Computers and Electronics in Agriculture*, 86:4–14.

Smith, R., Raine, S., and Minkevich, J. (2005). Irrigation application efficiency and deep drainage potential under surface irrigated cotton. *Agricultural Water Management*, 71(2):117–130.

Suits, L. D., Sheahan, T. C., Lakshmikantha, M. R., Prat, P. C., and Ledesma, A. (2009). Image analysis for the quantification of a developing crack network on a drying soil. *Geotechnical Testing Journal*, 32(6):102216.

Vogel, H.-J., Hoffmann, H., Leopold, A., and Roth, K. (2005a). Studies of crack dynamics in clay soil: II. a physically based model for crack formation. *Geoderma*, 125(3–4):213–223.

Vogel, H.-J., Hoffmann, H., and Roth, K. (2005b). Studies of crack dynamics in clay soil: I. experimental methods, results, and morphological quantification. *Geoderma*, 125(3–4):203–211.

Wang, J.-J., Zhu, J.-G., Mroueh, H. Mroueh, Chiu, and C.F. Chiu (2007). Hydraulic fracturing of rock-fill dam. *The International Journal of Multiphysics*, 1(2):199–219.

Weaver, T., Hulugalle, N., and Ghadiri, H. (2005). Comparing deep drainage estimated with transient and steady state assumptions in irrigated vertisols. *Irrigation Science*, 23(4):183–191.

CHAPTER 2. PERIDYNAMIC MODEL FOR TRANSIENT MOISTURE FLOW THROUGH UNSATURATED SOILS IN 1D

2.1 Abstract

A nonlocal, derivative free, formulation of the porous media flow problem in unsaturated soils is derived. It parallels the peridynamic theory, a nonlocal reformulation of solid mechanics presented by Silling (Silling, 2000). In the proposed model, the evolution of the state of a material point is driven by pairwise interactions with other points across finite distances. Flow and changes in moisture are the result of these interactions. Instead of featuring local gradients, the proposed model expresses the flow as a functional integral of the hydraulic potential field. The absence of spatial derivatives, undefined at or on discontinuities, makes the model a good candidate for flow simulations in fractured soils and lends itself to coupling with peridynamic mechanical models for simulating crack formation triggered by shrinkage and swelling, and assessing their potential impact on a wide range of processes, such as infiltration, contaminant transport, slope stability and integrity of clay barriers. Simulation results of infiltration and drainage in 1D using the peridynamic flow model are presented and compared to results from HYDRUS1D (Silling and Askari, 2005), a computer software that solves the classic Richards Equation using the finite element model.

2.2 Introduction

The movement of moisture in variably saturated soils is described by the Richards Equation (Equation 2.1) (Richards, 1931). It is a nonlinear partial

differential equation, and is a local continuum mechanics expression of the principle of conservation of mass applied to the Darcy-Buckingham Law of moisture flow in soils (Equation 2.2) (Darcy, 1856, Buckingham, 1907). As long as the domain being modeled is continuous, and remains so for the duration of the simulation, Equation 2.1 remains valid.

$$\frac{\partial \theta}{\partial t} = \nabla . \boldsymbol{q} + S. \tag{2.1}$$

where

$$\boldsymbol{q} = -K(h_m)\nabla(h_m + z). \tag{2.2}$$

Where θ is the volumetric moisture content, h_m is the soil matric head, z is the elevation head, $K(h_m)$ is the hydraulic conductivity as a function of the matric head, $\boldsymbol{q}$ is the flux vector, S is a source term in case there are any external sources or drains of moisture, and ∇ is the gradient operator.

However, changes in the moisture content of naturally occurring soils are often accompanied by changes in volume (Davidson and Page, 1956, Dinka, 2012, Braudeau and Mohtar, 2006). Depending on the mechanical properties of the soil, these volumetric deformations may lead to the formation and evolution of dessication cracks (Chertkov, 2002, Greco, 2002, Jarvis, 2007, Abou Najm et al., 2009, Abou Najm et al., 2010). These cracks act as preferential pathways for the rapid movement of moisture into deeper layers which in turn affects where and when the soil will swell or shrink (Greve et al., 2010, Braudeau et al., 2009, Sanders et al., 2012). Mathematically, these cracks are a violation of the assumption of continuity and points that lie on the surfaces and tips of cracks, where gradients are undefined, are points of singularities of equations 2.1 and 2.2.

In this paper, I present an alternative flow model to the classic Richard's equation based on Silling's reformulation of the theory of elasticity for solid

mechanics (Silling, 2000, Silling et al., 2010). In the proposed model, I replace the classic, local, continuum mechanics formulation by a nonlocal integral functional, free of spatial derivatives and valid even in the presence of evolving discontinuities. In the following I will concentrate on the one-dimensional formulation and validation of the model.

2.3 Peridynamic flow model in 1D

The proposed model is based on the bond based peridynamic model for solid mechanics (Silling, 2000, Silling et al., 2010). In Silling's model, the force felt by some material point is due to actions at a distance from all material points in the domain within a certain radius via pairwise interactions given by a force density function. The force density function for a homogeneous, isotropic and linear elastic material is a function of the original relative distance separating the interacting points and their relative displacement, and it has the units of force per volume squared. Multiplying each interaction by the volumes of the parter points gives the force felt by each due to their interaction. Integrating all the interactions connected to a certain point gives the total force felt by that point.

The following is a description of the proposed peridynamic flow model. The rate of change of the moisture content at some material point is due to actions at a distance from all material points in the domain within a certain radius via pairwise interactions. This is in contrast to the classic local continuum mechanics formulation, where a point is only influenced by its immediate neighbors that are separated from it by an infinitesimal distance. These pairwise interactions are given by a flow density function which gives the rate of moisture flow per volume squared. Multiplying each interaction by the volume of one partner point gives the rate of change of the volumetric moisture content experienced by the other due to their interaction (reduction in one point and increase in the other). Integrating all

the interactions connected to a certain point gives me the total rate of change of the volumetric moisture content at that point.

In contrast to Silling's peridynamic model for solid mechanics for homogeneous, isotropic, and linear elastic materials where the force density function is only a function of relative distance and relative displacement, I require that the flow density function be a function of the position and matric head or moisture content at the connected points. This generalization will allow me to model heterogeneous, variably saturated and anisotropic soils, where the medium properties may depend on position for a heterogeneous or layered soil profile, on matric head or moisture content for unsaturated soils, and on the orientation of the flow for anisotropic soils.

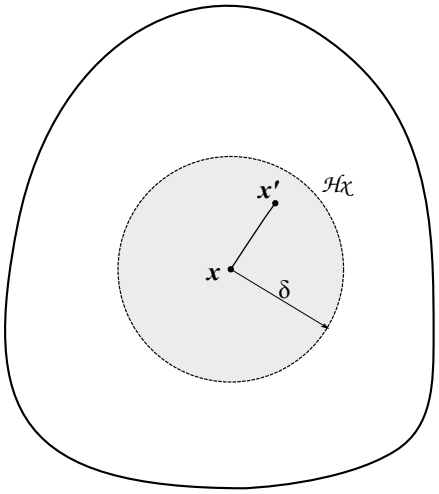

Fig. 2.1. Peridynamic medium representation. Point $\boldsymbol{x}$ is influenced by all points within its horizon. $\mathcal{H}_x$ is the horizon of $\boldsymbol{x}$, δ is the radius of the horizon.

To illustrate the basics of this peridynamic flow model, let me turn my attention to material point $\boldsymbol{x}$ inside a body of soil (Figure 2.1). Point $\boldsymbol{x}$ at time t has a moisture content of $\theta(\boldsymbol{x}, t)$, and is at some total hydraulic potential $H(\boldsymbol{x}, t) = h_m(\boldsymbol{x}, t)+z$. Let me now define $\mathcal{H}_x$ as the set of points located within some distance

δ of $\boldsymbol{x}$, I will call $\mathcal{H}_x$ the horizon of $\boldsymbol{x}$, and δ the horizon radius. The presence of a crack intersecting with the horizon notwithstanding, all the points in $\mathcal{H}_x$ are visible to $\boldsymbol{x}$, and they will each exert an influence on $\boldsymbol{x}$ given by the flow density function that I will represent by J. Now consider the point $\boldsymbol{x'}$ inside the horizon of $\boldsymbol{x}$ with $H(\boldsymbol{x'}, t) = h_m(\boldsymbol{x'}, t) + z'$.

The influence exerted by $\boldsymbol{x'}$ on $\boldsymbol{x}$, which is the rate of change of the volumetric moisture content at $\boldsymbol{x}$ per unit volume of $\boldsymbol{x'}$, is given by:

$$J(\boldsymbol{x}, \boldsymbol{x'}, h_m(\boldsymbol{x}, t), h_m(\boldsymbol{x'}, t)). \tag{2.3}$$

Multiplying Equation 2.3 by the volume of $\boldsymbol{x'}$, $\mathrm{d}V_{x'}$, gives me the rate of change of the volumetric moisture content at $\boldsymbol{x}$ due to $\boldsymbol{x'}$:

$$\frac{\partial \theta(\boldsymbol{x}|\boldsymbol{x'}, t)}{\partial t} = J(\boldsymbol{x}, \boldsymbol{x'}, h_m(\boldsymbol{x}, t), h_m(\boldsymbol{x'}, t))\mathrm{d}V_{x'}. \tag{2.4}$$

If I now account for all the interactions involving $\boldsymbol{x}$ by integrating all pairwise flow functions over the horizon of $\boldsymbol{x}$, $\mathcal{H}_x$, I arrive at the total rate of change of the volumetric moisture content at point $\boldsymbol{x}$ due to all its pairwise interactions, which is given by the following integral functional:

$$\frac{\partial \theta(\boldsymbol{x}, t)}{\partial t} = \int_{\mathcal{H}_x} J(\boldsymbol{x}, \boldsymbol{x'}, h_m(\boldsymbol{x}, t), h_m(\boldsymbol{x'}, t))\mathrm{d}V_{x'}. \tag{2.5}$$

In order to take into account the possible existence of a local moisture source or sink, such as a pumping well, a buried irrigation system, or a second embedded porosity, a source/sink term, $S(\boldsymbol{x}, t)$ should be added to Equation 2.5. The resultant expression gives the change in volumetric moisture content due to pairwise interactions and other sources:

$$\frac{\partial \theta(\boldsymbol{x}, t)}{\partial t} = \int_{\mathcal{H}_x} J(\boldsymbol{x}, \boldsymbol{x'}, h_m(\boldsymbol{x}, t), h_m(\boldsymbol{x'}, t))\mathrm{d}V_{x'} + S(\boldsymbol{x}, t). \tag{2.6}$$

If a crack happens to intersect with the horizon of point $\boldsymbol{x}$, its effect is accounted for by severing the influence on $\boldsymbol{x}$ of any interaction that intersects with it. This is captured by multiplying J by a term D which takes the value zero

if the interaction is severed, otherwise it is one. In the present paper I will not incorporate this term; however, I will return to it in the following chapters.

In order to proceed with my derivation it is helpful to describe and make certain assumptions about the properties of a peridynamic porous medium and the underlying mechanisms of moisture flow within it. It is important to note that these mechanisms are only a conceptual tool intended to guide me during the derivation of a mathematical model that, at least, successfully simulates the evolution of moisture content and flow as understood within the framework of classical continuous formulation of flow, while overcoming the difficulties faced by the classic formulation in simulating domains with evolving discontinuities.

To that end, it is useful to devise a physical proxy for the peridynamic porous medium. An intuitive, and as will be shown later, useful analogy is to think of the medium's material points as moisture reservoirs, and that between every pair of reservoirs, separated by a distance up to δ, there exists a one-dimensional pipe that is responsible for the exchange of moisture between the reservoirs it connects. These pipes represent the pairwise interactions given by J, and I will refer to them as peripipes. I would like to impose the following requirement:

1. Moisture is stored in the reservoirs only, zero moisture content in peripipes.
2. Moisture flows along the length of the peripipes and does not cross their longitudinal boundaries (pairwise interactions).
3. Peripipes are purely resistive, they have zero reactance and their response is proportional to the applied hydraulic potential at their end-nodes.
4. Peripipes have a uniform conductivity.
5. Peripipes conductivity is a function of the conductivity of the medium at their end-nodes.
6. Peripipes have a length equal to the euclidean distance between their end-nodes.

7. The response of peripipes may also depend on the distance separating the end-nodes.

Consider a prototype peripipe $\boldsymbol{xx'}$ connecting reservoirs $\boldsymbol{x}$ and $\boldsymbol{x'}$. Peripipe $\boldsymbol{xx'}$ has a conductance $\kappa(\boldsymbol{xx'}, t)$. Reservoirs $\boldsymbol{x}$ and $\boldsymbol{x'}$ have volumes $\mathrm{d}V_x$ and $\mathrm{d}V_{x'}$ respectively, and are at a hydraulic potential of $H(\boldsymbol{x}, t) = h_m(\boldsymbol{x}, t) + z$ and $H(\boldsymbol{x'}, t) = h_m(\boldsymbol{x'}, t) + z'$. The length of $\boldsymbol{xx'}$ is $||\boldsymbol{x'} - \boldsymbol{x}||$. Using points 1, 2 and 3 I could model the peripipe as a two port dissipative element with the following equation:

$$Q_{xx'} = C(\boldsymbol{xx'}, t)[H(\boldsymbol{x'}, t) - H(\boldsymbol{x}, t)]. \tag{2.7}$$

Where $Q_{xx'}$ is the amount of moisture that is leaving reservoir $\boldsymbol{x'}$ and entering reservoir $\boldsymbol{x}$ per unit time. $C(\boldsymbol{x}, \boldsymbol{x'}, t)$ is the lumped conductance of the peripipe $\boldsymbol{xx'}$ and is given by:

$$C(\boldsymbol{xx'}, t) = \frac{\kappa(\boldsymbol{x}, \boldsymbol{x'}, t)}{||\boldsymbol{x'} - \boldsymbol{x}||}. \tag{2.8}$$

Plugging Equation 2.8 in Equation 2.7 I get:

$$Q_{xx'} = \frac{\kappa(\boldsymbol{xx'}, t)}{||\boldsymbol{x'} - \boldsymbol{x}||}[H(\boldsymbol{x'}, t) - H(\boldsymbol{x}, t)]. \tag{2.9}$$

Remember that $Q_{xx'}$ is the rate of moisture being exchanged between $\boldsymbol{x}$ and $\boldsymbol{x'}$. Dividing $Q_{xx'}$ by $\mathrm{d}V_x$, the volume of reservoir $\boldsymbol{x}$, I get the rate of change in volumetric moisture content in reservoir $\boldsymbol{x}$ due to its interaction with $\boldsymbol{x'}$ per unit time. If I further divide by $\mathrm{d}V_{x'}$, the volume of reservoir $\boldsymbol{x'}$, I get the change in volumetric moisture content in reservoir $\boldsymbol{x}$ per unit volume of reservoir $\boldsymbol{x'}$ per unit time, which is what I am looking for as an expression of J. Redefining κ as the conductivity of the peripipe normalized with respect to volume squared, I get:

$$J(\boldsymbol{x}, \boldsymbol{x'}, h_m(\boldsymbol{x}, t), h_m(\boldsymbol{x'}, t)) = \frac{\kappa(\boldsymbol{xx'}, t)}{\|\boldsymbol{x'} - \boldsymbol{x}\|}(H(\boldsymbol{x'}, t) - H(\boldsymbol{x}, t)). \tag{2.10}$$

Due to the nonlinear dependence of soil parameters on moisture content and potential anisotropy and inhomogeneity, and the requirement stated in point 5 that

peripipe conductivity depends on the material conductance at its end-nodes, the peripipe conductivity κ should be a function of $\boldsymbol{x}$, $\boldsymbol{x'}$, $h_m(\boldsymbol{x}, t)$, and $h_m(\boldsymbol{x'}, t)$. The details of the function κ and its exact form will be derived later in the chapter.

2.4 Peridynamic flux equation in 1D

Whether I am describing the flow using the classic formulation or the proposed peridynamic formulation, moisture flux across some surface $\mathcal{S}$ is the amount of moisture flowing across the surface $\mathcal{S}$ in a normal direction per unit area of the surface per unit time. In the classic formulation of one-dimensional flow problems, it is given by:

$$\boldsymbol{q}_c(\boldsymbol{x}, t) = -K(\boldsymbol{x}, t)\nabla.H(\boldsymbol{x}, t). \tag{2.11}$$

This definition can be restated in a form that is more easily related to the concept of a peridynamic porous medium and the description of conceptual transport mechanisms underlying the behavior of such a material. This restated definition will now read as follows: moisture flux across some surface is the net amount of moisture exchanged between points located on one side of the surface with points located on the other side of the surface, per unit area of that surface, per unit time. In the proposed peridynamic model, moisture exchange is driven by pairwise interactions via peripipes connecting material points, and the flux is the sum of all moisture exchanged due to pairwise interactions between points on one side of the surface with points on the other side, per unit area per unit time.

Consider the 1D soil column with a horizon radius δ depicted in Figure 2.2. I would like to evaluate the moisture flux across the surface $\mathcal{S}$ normal to the column at $x = x_s$. Let me start by identifying the points that have pipes linking them to points located across $\mathcal{S}$ from them. All points located at a distance larger than δ from either side of the surface $\mathcal{S}$ have their entire horizon contained in the same side of $\mathcal{S}$ that they are in. Therefore, these points do not interact and exchange moisture with points located on the opposite side of $\mathcal{S}$ to theirs, consequently they

do not contribute to the moisture flux across $\mathcal{S}$. On the other hand, a point located within a distance δ of the surface $\mathcal{S}$ has part of its horizon located across $\mathcal{S}$; and, the moisture exchanged between that point and all points within its horizon that are located across $\mathcal{S}$ contribute to the moisture flux across $\mathcal{S}$. This is similar to Lehoucq and Silling proposed for the mechanical stress in the peridynamic model for solid mechanics (Lehoucq and Silling, 2008).

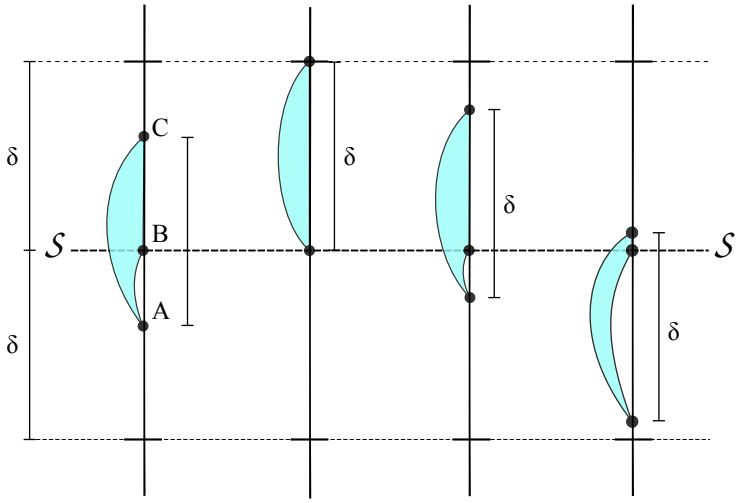

Fig. 2.2. Peridynamic moisture flux.

For example, point A located below $\mathcal{S}$ at $x = x_A$ with $||x_A - x_s|| < \delta$ has pairwise interactions with all points on the segment BC with coordinates $x_B = x_s$ and $x_C = x_A + \delta$. The contribution to the moisture flux across $\mathcal{S}$ of all the pipes crossing $\mathcal{S}$ involving point A – namely, the peripipes that are connecting point A to all points of segment BC – is given by:

$$\boldsymbol{q}(\boldsymbol{x_s}|\boldsymbol{x_A}, t) = -\int_{x_s}^{x_a+\delta} \frac{\kappa(\boldsymbol{x}_A, \boldsymbol{x'}, t)}{||\boldsymbol{x'} - \boldsymbol{x_A}||}[H(\boldsymbol{x'}, t) - H(\boldsymbol{x}_A, t)]\mathrm{d}x'. \tag{2.12}$$

The total flux across $\mathcal{S}$, which is the combined contribution of all interactions crossing $\mathcal{S}$, is the combined contribution of all pairwise interactions involving the points which are located within a maximum distance of δ from the surface $\mathcal{S}$.

Taking the points below $\mathcal{S}$, these are the points $\boldsymbol{x}$ with $x_s - \delta < x < x_s$. And the total flux is given by:

$$\boldsymbol{q}(\boldsymbol{x_s}, t) = \int_{x_s-\delta}^{x_s} q(\boldsymbol{x_s}|\boldsymbol{x''}, t)\mathrm{d}x''. \tag{2.13}$$

$$\boldsymbol{q}(\boldsymbol{x_s}, t) = -\int_{x_s-\delta}^{x_s}\int_{x_s}^{x''+\delta} \frac{\kappa(\boldsymbol{x''}, \boldsymbol{x'}, t)}{||\boldsymbol{x'} - \boldsymbol{x''}||}[H(\boldsymbol{x'}, t) - H(\boldsymbol{x''}, t)]\mathrm{d}x'\mathrm{d}x''. \tag{2.14}$$

I have only included the points below the surface as points of origin, because including points on both sides would lead to double counting the peripipes.

2.5 Peridynamic hydraulic conductivity function in 1D

In this section I would like to relate the peridynamic hydraulic conductivity to the classic measurable hydraulic conductivity of the soil. This entails finding an expression for κ as a function of the classic hydraulic conductivity that will make the results from the peridynamic model and those from the classic approach equal. In the case of thebond based peridynamic model for solid mechanics, one approach to relate the peridynamic constant to the classic elastic bulk modulus is to equate the classic and peridynamic expressions for the strain energy density for an infinite isotropic homogeneous body under isotropic extension (Silling, 2000, Silling et al., 2010, Kilic and Madenci, 2010).

I use a similar tactic but replacing strain energy density with moisture flux; the latter is analogous to mechanical stress, which was used by Liu and Hong to calculate the peridynamic elastic parameter (Liu and Hong, 2012). Suppose I have a saturated one-dimensional infinite homogeneous column of soil. Suppose also that the column is at steady state and under a linear hydraulic potential field $H(x) = ax + c$. I would like to have the moisture flux across a surface at $x = x_s$ given by the classic method to be equal to the same given by the peridynamic flow model.

According to the classic formulation, the flux across the surface x_s is given by Darcy's Law:

$$\begin{aligned}\boldsymbol{q}(\boldsymbol{x_s}) &= -K\nabla.H(x)|_{x_s} \\ &= -K\frac{\partial(ax+c)}{\partial x}|_{x_s} \\ &= -Ka. \end{aligned} \tag{2.15}$$

where K is the classic hydraulic conductivity and a is the applied hydraulic potential gradient.

According to the peridynamic formulation, the flux across the surface is given by:

$$\begin{aligned}\boldsymbol{q}(\boldsymbol{x_s}) &= -\int_{x_s-\delta}^{x_s}\int_{x_s}^{x''+\delta}\frac{\kappa(\boldsymbol{x},\boldsymbol{x'})}{||\boldsymbol{x'}-\boldsymbol{x_s}||}[H(\boldsymbol{x'})-H(\boldsymbol{x}_s)]\mathrm{d}x'\mathrm{d}x'' \\ &= -\int_{x_s-\delta}^{x_s}\int_{x_s}^{x''+\delta}\frac{\kappa(\boldsymbol{x},\boldsymbol{x'})}{||\boldsymbol{x'}-\boldsymbol{x_s}||}[(ax'+c)-(ax_s+c)]\mathrm{d}x'\mathrm{d}x'' \\ &= -\int_{x_s-\delta}^{x_s}\int_{x_s}^{x''+\delta}\frac{\kappa(\boldsymbol{x},\boldsymbol{x'})}{||\boldsymbol{x'}-\boldsymbol{x_s}||}[a(x'-x_s)]\mathrm{d}x'\mathrm{d}x''. \end{aligned} \tag{2.16}$$

Where $\kappa(\boldsymbol{x},\boldsymbol{x'})$ is the peridynamic conductivity function and δ is the radius of the horizon of the peridynamic material.

Before I proceed with the derivation, I have to decide on the form of $\kappa(\boldsymbol{x},\boldsymbol{x'})$, specifically, the dependence of $\kappa(\boldsymbol{x},\boldsymbol{x'})$ on the distance between the interacting point. Investigations of the specific effects that the shape of the influence function has on the behavior of a system are still in their infancy (Seleson and Parks, 2011). Nevertheless, this dependence translates into an influence function and, in addition to the horizon radius δ, is a description of the nonlocality of the peridynamic model. I will derive the peridynamic conductivity function for two influence shapes: uniform, and linear (Figure 2.3).

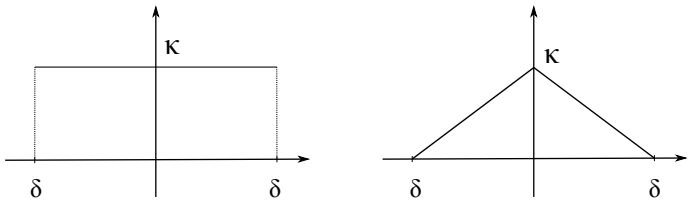

Fig. 2.3. Uniform and triangular influence functions.

2.5.1 Uniform influence function

In the case of a uniform influence function, there is no dependence of the peridynamic hydraulic conductivity on the distance between points. In this case I have:

$$\kappa(x, x') = \kappa. \tag{2.17}$$

Plugging Equation 2.17 into Equation 2.16 leads to:

$$\begin{aligned} \boldsymbol{q}(\boldsymbol{x_s}) &= -\int_{x_s-\delta}^{x_s}\int_{x_s}^{x''+\delta} \frac{\kappa}{||\boldsymbol{x'} - \boldsymbol{x_s}||}[a(x' - x_s)]\mathrm{d}x'\mathrm{d}x'' \\ &= -\frac{\kappa a \delta^2}{2}. \end{aligned} \tag{2.18}$$

Equating equations 2.18 and 2.15 leads to the following relationship between the classic hydraulic conductivity and the peridynamic hydraulic conductivity:

$$\begin{aligned} -Ka &= -\frac{\kappa a \delta^2}{2} \\ \kappa(\boldsymbol{x}, \boldsymbol{x'}) &= \frac{2K}{\delta^2}. \end{aligned} \tag{2.19}$$

2.5.2 Linear influence function

In the case of a linear influence function, the peridynamic hydraulic conductivity κ has a maximum at the center of the horizon and it decreases linearly

as the length of the peripipe increases. If I set the influence to be zero at the edge of the horizon I get:

$$\kappa(x, x') = \kappa\left(1 - \frac{\|\boldsymbol{x'} - \boldsymbol{x}\|}{\delta}\right). \tag{2.20}$$

Plugging Equation 2.20 into Equation 2.16 leads to:

$$\begin{aligned}\boldsymbol{q}(\boldsymbol{x_s}) &= -\int_{x_s-\delta}^{x_s}\int_{x_s}^{x''+\delta} \frac{\kappa}{||\boldsymbol{x'} - \boldsymbol{x_s}||}\left(1 - \frac{\|\boldsymbol{x'} - \boldsymbol{x}_s\|}{\delta}\right)[a(x' - x_s)]\mathrm{d}x'\mathrm{d}x'' \\ &= -\frac{\kappa a\delta^2}{6}.\end{aligned} \tag{2.21}$$

Equating equations 2.21 and 2.15 leads to the following relationship between the classic hydraulic conductivity and the peridynamic hydraulic conductivity:

$$\begin{aligned}-Ka &= -\frac{\kappa a\delta^2}{6} \\ \kappa &= \frac{6K}{\delta^2} \\ \kappa(\boldsymbol{x}, \boldsymbol{x'}) &= \frac{6K}{\delta^2}\left(1 - \frac{\|\boldsymbol{x'} - \boldsymbol{x}\|}{\delta}\right).\end{aligned} \tag{2.22}$$

2.5.3 Unsaturated soil

Equations 2.20 and 2.22 were derived starting from the assumptions that the medium is homogeneous and at saturation, hence that it has a constant hydraulic conductivity. However, soils are often heterogeneous, and for unsaturated regimes the hydraulic conductivity is dependent on moisture content or matric potential. In order to address this difficulty, I will adjust the definition of a pairwise interaction to become mediated by two parallel peripipes, with half of the interaction coming from each of the peripipes and each one having a peridynamic conductivity derived from one of the end nodes hydraulic conductivity.

$$\kappa(\boldsymbol{x}, \boldsymbol{x'}, t) = \frac{\kappa(\boldsymbol{x}, t) + \kappa(\boldsymbol{x'}, t)}{2}. \tag{2.23}$$

I will further assume that the relationship between the peridynamic conductivity function and the classic hydraulic conductivity of the medium depends

on the horizon radius, the number of dimensions of the problem, and the form of the influence function (whether it is uniform, linear, Gaussian, or any other conceivable form). I also assume that it does not depend on the variation of the hydraulic conductivity within the horizon. The adequacy of this assumption will be verified numerically by comparing the results of flow simulations using the peridynamic flow model to those using the classic approach.

Assuming this assumption holds, I get the following equations for the rate of volumetric moisture change and moisture flux for a peridynamic porous material with a uniform influence function in 1D:

$$\frac{\partial\theta(\boldsymbol{x},t)}{\partial t} = \int_{x-\delta}^{x+\delta} \frac{[K(\boldsymbol{x},t)+K(\boldsymbol{x'},t)]}{\delta^2||\boldsymbol{x'}-\boldsymbol{x}||}[H(\boldsymbol{x'},t)-H(\boldsymbol{x},t)]\mathrm{d}x'. \tag{2.24}$$

$$\boldsymbol{q}(\boldsymbol{x},t) = -\int_{x-\delta}^{x}\int_{x}^{x''+\delta} \frac{[K(\boldsymbol{x},t)+K(\boldsymbol{x'},t)]}{\delta^2||\boldsymbol{x'}-\boldsymbol{x}||}[H(\boldsymbol{x'},t)-H(\boldsymbol{x},t)]\mathrm{d}x'\mathrm{d}x''. \tag{2.25}$$

For a peridynamic material with a linear influence function equations 2.24 and 2.25 become the following:

$$\frac{\partial\theta(\boldsymbol{x},t)}{\partial t} = \int_{x-\delta}^{x+\delta} \left(1-\frac{\|\boldsymbol{x'}-\boldsymbol{x}\|}{\delta}\right)\frac{3[K(\boldsymbol{x},t)+K(\boldsymbol{x'},t)]}{\delta^2||\boldsymbol{x'}-\boldsymbol{x}||}[H(\boldsymbol{x'},t)-H(\boldsymbol{x},t)]\mathrm{d}x'. \tag{2.26}$$

$$\boldsymbol{q}(\boldsymbol{x},t) = -\int_{x-\delta}^{x}\int_{x}^{x''+\delta} \left(1-\frac{\|\boldsymbol{x'}-\boldsymbol{x}\|}{\delta}\right)\frac{3[K(\boldsymbol{x},t)+K(\boldsymbol{x'},t)]}{\delta^2||\boldsymbol{x'}-\boldsymbol{x}||}[H(\boldsymbol{x'},t)-H(\boldsymbol{x},t)]\mathrm{d}x'\mathrm{d}x''. \tag{2.27}$$

2.6 Numerical implementation in 1D and comparison with a classic model

Numerical implementation of the peridynamic model was carried out by discretizing the medium into nodes using a regular grid. Figure 2.4 shows a section

of a discretized soil column with a grid spacing of Δx and a horizon radius $\delta = m\Delta x$ with $m = 3$, and where m is the horizon radius in multiples of grid lengths. Each node in the grid represents a volume of Δx, and has a moisture content $\theta(x_n, t)$, an associated hydraulic potential $H(x_n, t)$ and a hydraulic conductivity $K(x_n, t)$.

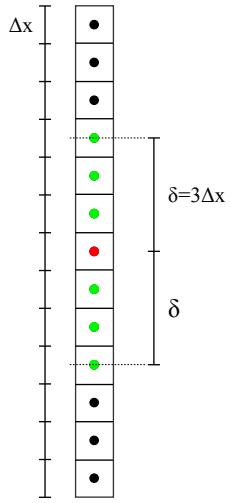

Fig. 2.4. Discrete representation of a peridynamic horizon of radius $3\Delta x$. Point in red is the center of the horizon. Points in green belong to the horizon.

It should be noted that there is no restriction on the type of grid used when discretizing the domain. The decision to use a regular grid was taken due to its simplicity and because only regular shapes will be modeled for this research. In fact, irregular grids are just as adequate, if not more helpful, when modeling complex geometries (Simunek et al., 2005).

The discrete form of the peridynamic equation for the evolution of moisture content for the cases of uniform and linear influence functions in 1D are given by Equation 2.28 and 2.29 respectively:

$$\frac{\partial\theta(\boldsymbol{x}_n,t)}{\partial t}=\sum_{\substack{p=n-m\\p\neq n}}^{n+m}\frac{[K(\boldsymbol{x_n},t)+K(\boldsymbol{x_p},t)]}{\delta^2||\boldsymbol{x_p}-\boldsymbol{x_n}||}[H(\boldsymbol{x_p},t)-H(\boldsymbol{x_n},t)]\Delta x_p. \tag{2.28}$$

Where the summation index p spans all the points belonging to the horizon of point x_n.

$$\boldsymbol{q}(\boldsymbol{x_n},t)=-\sum_{k=n-m}^{n-1}\sum_{p=n}^{k+m}\frac{[K(\boldsymbol{x_k},t)+K(\boldsymbol{x_p},t)]}{\delta^2||\boldsymbol{x_p}-\boldsymbol{x_k}||}[H(\boldsymbol{x_p},t)-H(\boldsymbol{x_k},t)]\Delta x_p\Delta x_k. \tag{2.29}$$

Where the summation index k spans all the points on one side of the surface $\mathcal{S}$ as far as one horizon radius away from $\mathcal{S}$. And, for each point x_k, the index p spans all the points in the horizon of x_k to the opposite side of the surface $\mathcal{S}$.

Similarly, the discrete form of the peridynamic moisture flux equation for the cases of uniform and linear influence functions are given by Equations 2.30 and 2.31 respectively:

$$\frac{\partial\theta(\boldsymbol{x}_n,t)}{\partial t}=\sum_{\substack{p=n-\frac{m}{2}\\p\neq n}}^{n+\frac{m}{2}}\left(1-\frac{\|\boldsymbol{x_p}-\boldsymbol{x_k}\|}{\delta}\right)\frac{3[K(\boldsymbol{x_n},t)+K(\boldsymbol{x_p},t)]}{\delta^2||\boldsymbol{x_p}-\boldsymbol{x_n}||}[H(\boldsymbol{x_p},t)-H(\boldsymbol{x_n},t)]\Delta x_p. \tag{2.30}$$

$$\boldsymbol{q}(\boldsymbol{x_n},t)= -\sum_{k=n-\frac{m}{2}}^{n-1}\sum_{p=n}^{k+\frac{m}{2}}\left(1-\frac{\|\boldsymbol{x_p}-\boldsymbol{x_k}\|}{\delta}\right)\frac{3[K(\boldsymbol{x_k},t)+K(\boldsymbol{x_p},t)]}{\delta^2||\boldsymbol{x_p}-\boldsymbol{x_k}||}[H(\boldsymbol{x_p},t)-H(\boldsymbol{x_k},t)]\Delta x_p\Delta x_k. \tag{2.31}$$

Several functions exist for modeling the relationship between the soil moisture content and matric potential and for calculating the unsaturated hydraulic conductivity as a function of the moisture content and the saturated hydraulic

conductivity. For the current implementation I opted for the Van Genuchten model (Van Genuchten, 1980) for matric potential and hydraulic conductivity given by the following equations:

$$\theta(h_m) = \theta_r + \frac{\theta_s - \theta_r}{[1 + (\alpha|h_m|)^n]^{1-1/n}}. \tag{2.32}$$

$$K(\theta) = K_s \left(\frac{\theta - \theta_r}{\theta_s - \theta_r}\right)^{\frac{1}{2}} \left\{1 - \left[1 - \left(\frac{\theta - \theta_r}{\theta_s - \theta_r}\right)^{\frac{n}{n-1}}\right]^{\frac{n-1}{n}}\right\}^2. \tag{2.33}$$

Where θ_s and θ_r are the volumetric water content at saturation and residual respectively. K_s is the soil hydraulic conductivity at saturation, α is related to the inverse of the air entry pressure, and n is a parameter related to the soil pore size distribution. Rearranging Equation 2.32 I get the matric potential as a function of the moisture content:

$$h_m(\theta) = -\frac{1}{\alpha}\left[\left(\frac{\theta_s - \theta_r}{\theta - \theta_r}\right)^{\frac{n}{n-1}} - 1\right]^{\frac{1}{n}}. \tag{2.34}$$

To make use of current multi-core processors in speeding up the computation time, the model was implemented in a parallel C++ code was using OpenMP. The algorithm of which is presented Figure 2.5:

In order to validate the proposed model, and analyze the effects that the horizon radius (δ), the density of points per horizon radius (m), and the type of influence function (uniform or triangular) have on the performance of the model, several scenarios are simulated. Due to the lack of an analytical solution of the flow problem, the same scenarios are also simulated using HYDRUS-1D (Silling and Askari, 2005), a one-dimensional finite element model that solves the classic Richards equation. The results from HYDRUS-1D are used as a benchmark for evaluating to accuracy of the peridynamic flow model.

The validation scenarios are divided into two major groups. The first group is scenarios of drainage of a vertical soil column from saturation. The second group is

```
1  Setup geometry;
2  Generate peripipe list;
3  Generate matric head vs moisture content look-up table;
4  Generate hydraulic conductivity vs moisture content look-up table;
5  Initialize moisture content to initial conditions;
6  for t = 1 to Number of time steps do
7      for p = 1 to Number of peripipes do in parallel
8          Look up matric potentials of nodes connected by peripipe p using their
           moisture content;
9          Calculate difference in total hydraulic head across peripipe p;
10         Look up peridynamic hydraulic conductivities of nodes connected by
           peripipe p using their moisture content;
11         Calculate peridynamic hydraulic conductivity of peripipe p;
12         Calculate change in moisture content of each node due to peripipe p;
13         Accumulate change in moisture content for each node;
14     end
15     for n = 1 to Number of nodes do in parallel
16         Update moisture content of node n;
17         Reset change in moisture content to zero;
18         if node n belongs to a boundary then
19             Update moisture content of node n according to boundary
               condition;
20         end
21     end
22     Write results of timestep t to file;
23 end
```

Fig. 2.5. Implementation algorithm of peridynamic moisture flow model

scenarios of infiltration into a vertical soil column initially 10% of the saturation moisture content. For each group, identical scenarios are simulated using four horizon radii. In addition, for each horizon radius, several grid spacing values were used. These values were chosen to get four point density values. Table 4.1 lists the different horizon radii and m values used, along with the corresponding grid spacing. Table 3.1 lists the soil parameters for the Van Genuchten model for matric potential and hydraulic conductivity for the soil used.

Table 2.1
Grid size for the various horizon radii (δ) and point densities used (m).

$\delta \backslash m$	1	3	4	5
2	0.500	1.500	2.0	2.50
4	0.250	0.750	1.0	1.25
5	0.200	0.600	0.8	1.00
8	0.125	0.375	0.5	0.625

Table 2.2
Van Genuchten soil parameters.

θ_s	θ_r	K_s	α	n
0.430	0.078	24.96	0.036	1.56

For each validation scenario I repeated the simulation for different values of the peridynamic horizon radius δ and the discretization grid spacing Δx. I used three horizon radii: 1 cm, 3cm, 4cm, and 5cm. For each horizon radius value I repeated the simulations for 4 different grid spacings. The grid spacings were calculated by specifying the density of nodes per horizon, such that $\Delta x = \frac{\delta}{m}$, with $m = 2, 4, 6, 8$. In addition to the δ-m combinations, I repeated the simulation using a uniform influence function and a triangular influence function.

2.6.1 Group 1: Drainage scenarios

This is the drainage scenarios group. The vertical soil column is 300 cm long. Initially the entire soil column is at saturation. The top boundary at $x = 300cm$ is a no flow boundary condition. The bottom boundary is maintained at saturation, simulating the level of the water table at $x = 0cm$.

In HYDRUS-1D the column is simulated using the Van Genuchten soil model, and a top boundary condition of zero flux. The bottom boundary is maintained at

saturation and, initially, all the soil profile is set to saturation moisture content. Grid length is set to $0.5cm$ in order to remain within the maximum number of nodes of the program. Conversion criteria were set to 1E-5 for absolute change in moisture content and to $0.01cm$ for absolute change in matric potential.

For the peridynamic model, all horizon radii listed in table 4.1 were used. The soil is initially set at saturation moisture content. Because of the nonlocal nature of the formulation, the bottom boundary condition is simulated by adding an additional number of nodes from $x = 0cm$ to $x = -\delta$. The lower boundary nodes are maintained at saturation moisture content for the duration of the simulation. The time step used for the drainage scenarios is 1E-6 days.

Figure 2.6 is a plot of the moisture profile of the drainage scenario recorded time at 1 day, 3 day and 10 days. The solid lines are the results using the classic formulation modeled using HYDRUS-1D. Overlayed in squares and triangles are the plots using the peridinamic formulation for the uniform and triangular influence functions respectively for a horizon radius $\delta = 1cm$ and a point density value $m = 4$. Following a visual inspection of the plots I observe a very good agreement between the results of the peridynamic model and the classic model.

In order to obtain a more quantitative evaluation of the level of agreement between both methods, I will analyze more closely the results at 1 day. Specifically, I will examine the effects the values of the horizon radius (δ), the point density (m) and the shape of the influence function ($uniform$ or $linear$) have on the relative difference between the results of the peridynamic model and HYDRUS-1D for two variables: the value of the surface moisture content and the total amount of moisture that exited the profile.

Figures 2.7 and 2.9 are plots of the relative difference of the surface moisture content versus the point density value (m) for various horizon radii ($\delta = 1, 3, 4, 5cm$) using a uniform influence function and a linear influence function respectively. I observe that with increasing values of m, the relative difference curve for each horizon radius (δ) converges to a limit value with smaller relative

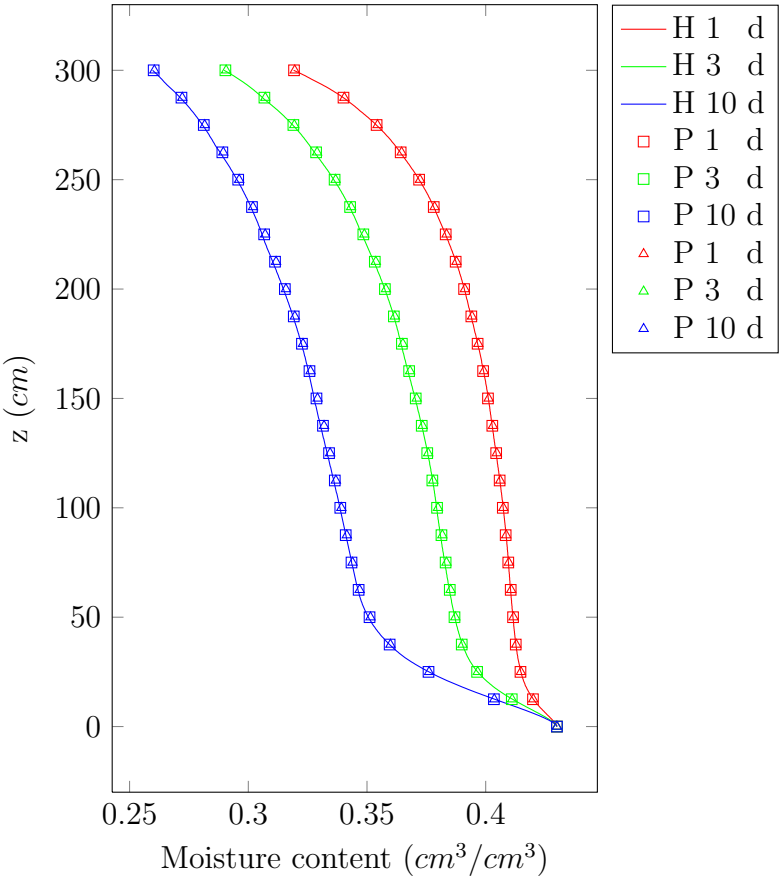

Fig. 2.6. Drainage scenario: Moisture profile at 1, 3, and 10 days. HYDRUS-1D simulation results plotted as solid lines. Peridynamic simulation results for $\delta = 1cm$, $m = 4$. Uniform influence function results plotted as squares, triangular as triangles; only every 50 points are plotted for visibility.

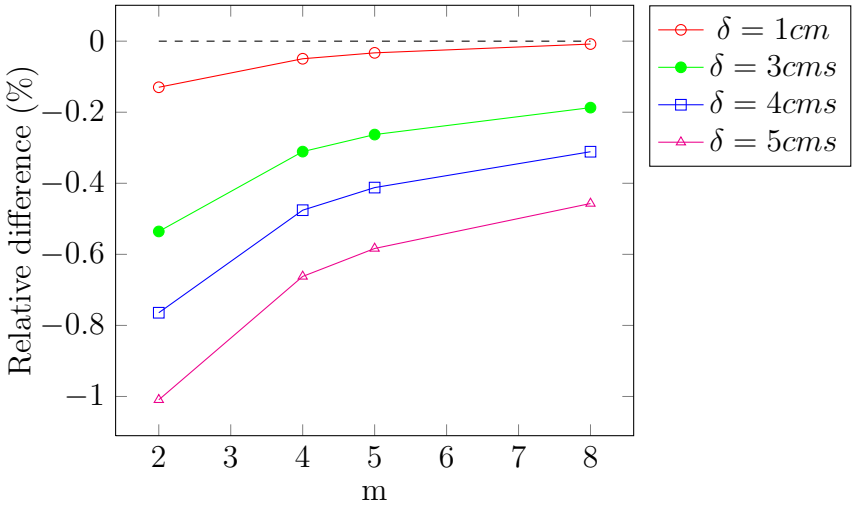

Fig. 2.7. Drainage scenario: Effect of m on the relative difference (%) for soil surface moisture content at 1 day between HYDRUS-1D and the peridynamic simulation using a uniform influence function. For each horizon radius the relative difference decreases with increasing point density. Also, relative difference curves of smaller horizon radii are closer to 0%.

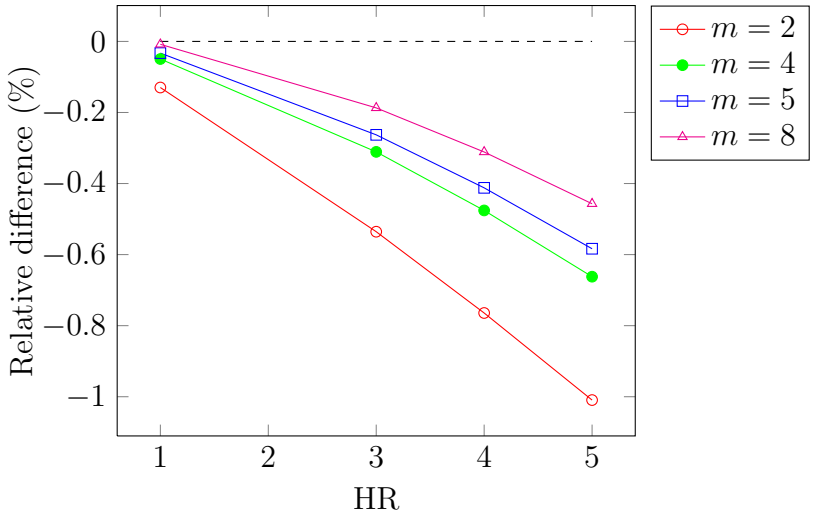

Fig. 2.8. Drainage scenario: Effect of δ on the relative difference (%) for soil surface moisture content at 1 day between HYDRUS-1D and the peridynamic simulation using a uniform influence function. For each point density, m, the relative difference decreases with decreasing δ. Also, relative difference curves of higher m values are closer to 0%.

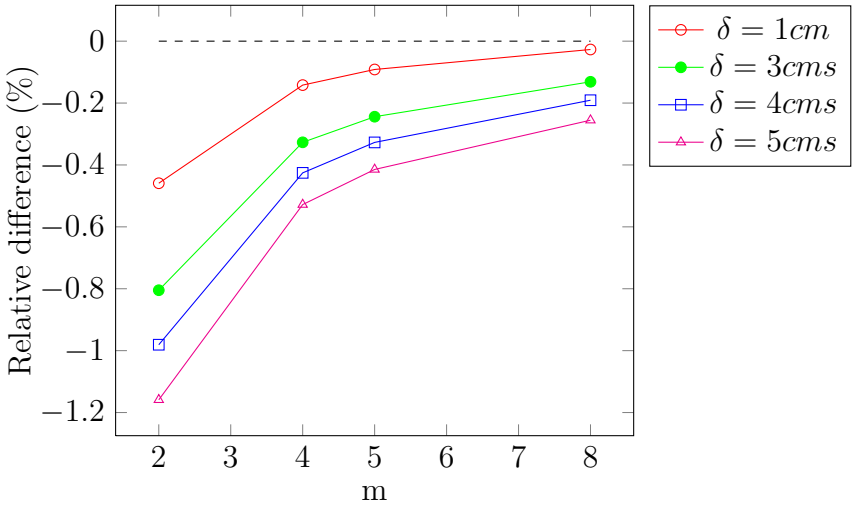

Fig. 2.9. Drainage scenario: Effect of m on the relative difference (%) for soil surface moisture content at 1 day between HYDRUS-1D and the peridynamic simulation using a triangular influence function. For each horizon radius the relative difference decreases with increasing point density. Also, relative difference curves of smaller horizon radii are closer to 0%.

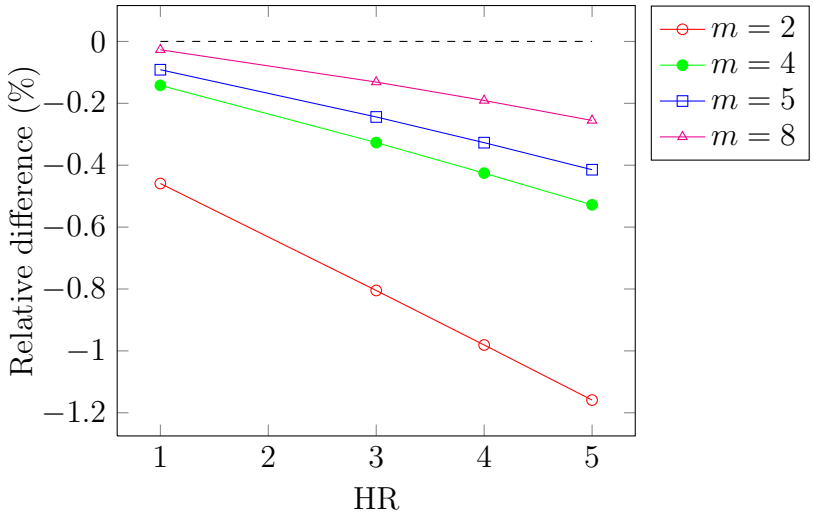

Fig. 2.10. Drainage scenario: Effect of δ on the relative difference (%) for soil surface moisture content at 1 day between HYDRUS-1D and the peridynamic simulation using a triangular influence function. For each point density, m, the relative difference decreases with decreasing δ. Also, relative difference curves of higher m values are closer to 0%.

difference. This behavior is expected; because, as the number of points within a horizon increases, the distribution of moisture content is sampled more accurately and its influence on the change of moisture content at the center of the horizon is better represented. The same trend is observed in Figures 2.12 and 2.14, where the relative difference of the total moisture that drained out of the profile is plotted against m for the same horizon radii, using uniform and triangular influence functions respectively.

The results also indicate that as the horizon radius (δ) decreases the performance of the model increases. Larger horizon radii (δ) lead to an overestimation of the surface moisture content, and and under estimation of the total amount of drained moisture; and that with decreasing horizon radii, the relative difference moves towards a smaller value. This is evident in Figures 2.7 and 2.9, where the curve of smaller horizons are above those of larger ones, and in Figures 2.12 and 2.14 where curves of smaller horizons are below those of larger horizons. I attribute this to the fact that as the horizon radius decreases, the influence of points closer to the center of the horizon increases and the model becomes more localized and closer to the classic local formulation.

Figures 2.8 and 2.10 are plots of relative difference of the surface moisture content as a function of the horizon radius (δ) for various values of m, using a uniform influence function and a linear influence function respectively. Similar plots are shown in Figures 2.13 and 2.15 for the relative difference in total amount of moisture drained. This confirm my previous statement regarding the effects of δ and m and the performance of the model. In addition, they illustrate how the value of m modulates the effect that the horizon radius has on the performance of the model. I observe that as m increases, in addition to an improvement in the relative difference, there is a reduction in the slope of the curve, and consequently a reduction in the deterioration of the performance of the model with increasing δ.

The graphs in Figure 2.11 are plots comparing curves of the relative difference for the surface moisture content as a function of m of simulations using a uniform

influence function with those using a triangular influence function. From top to bottom, I have plotted the curves for $\delta = 1, 3, 5cm$. I notice that as the horizon radius increases, the simulations where a triangular influence function was used perform better compared to the ones where a uniform influence function was used. I attribute this effect to the fact that with a triangular influence function, the model is giving more weight to the points that are closer to the horizon center than those that are farther. On the other hand, with a uniform influence function, an equal weight is assigned to all points within the horizon. Effectively, for the same horizon radius, compared to a model with a uniform influence function, a model with a triangular influence function is more local, and will therefore, lead to results closer to a classic local model. This feature is not observed for the total amount of moisture drained (Figure 2.16). Both uniform and linear influence functions converge towards the same limit without intersecting.

2.6.2 Group 2: Infiltration scenarios

In this group of scenarios, I am simulating infiltration from runoff into a $300cm$ vertical soil column initial at 10% saturation. The infiltration is soil controlled and ponding height is constant and equal to zero. The top boundary condition is set to a constant head $h_m = 0cm$. The bottom boundary condition is deep drainage to simulate water table far below the bottom of the column. Because at the recorded time steps the infiltration front remains above $x = 0cm$, I could use a constant moisture content of 10% saturation at the bottom as a boundary condition.

As in the previous group, I am using Van Genuchten Soil model in HYDRUS-1D. The top boundary condition is a constant moisture content equal to saturation, the bottom boundary condition is constant moisture content maintained at 10% saturation. Initially all nodes except the node at $x = 300cm$ are set to a moisture content of 10% saturation. The grid length is $0.5cm$, and conversion criteria are the same as those of the previous group.

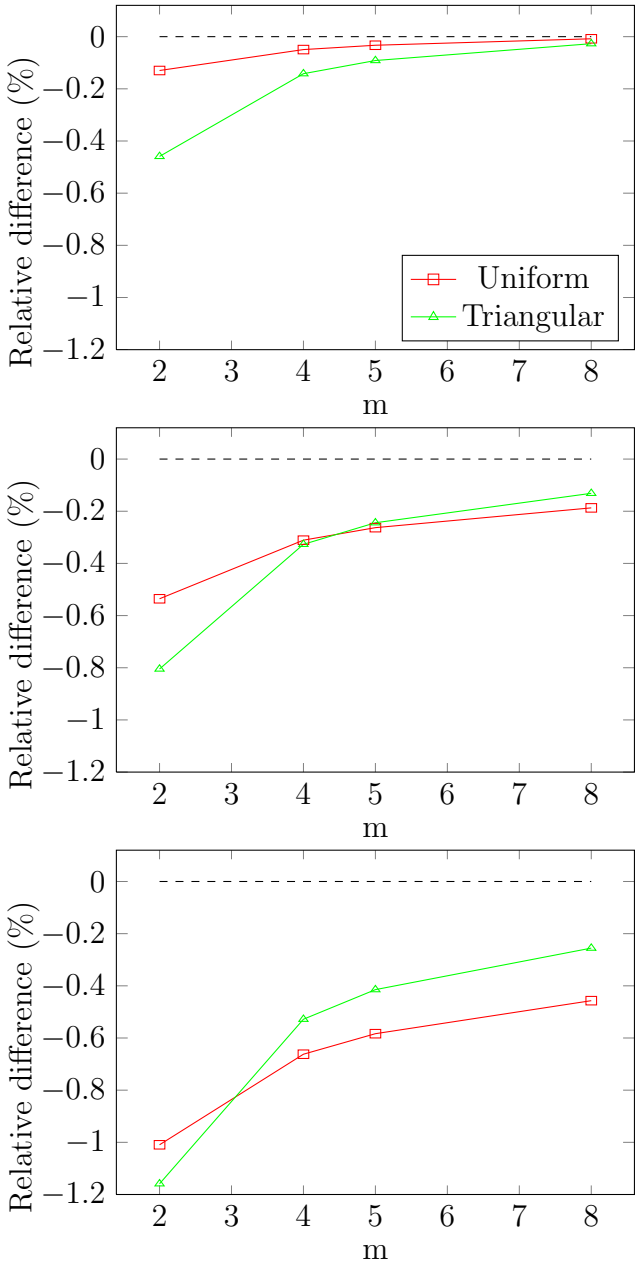

Fig. 2.11. Drainage scenario: Comparison between the effects of uniform and triangular influence function on the relative difference of surface moisture content at 1 day. From top to bottom $\delta = 1, 3, 5 cms$ respectively. I notice that as the horizon radius increases the performance of the triangular influence function with respect to the uniform influence function improves.

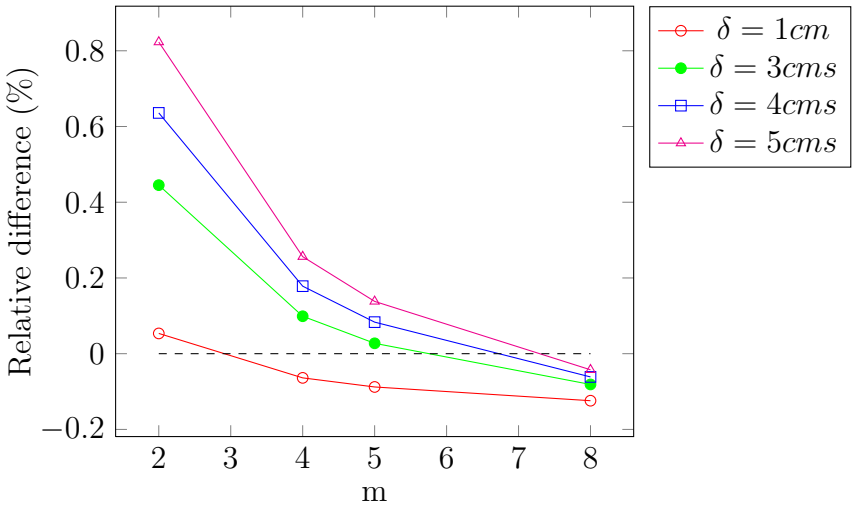

Fig. 2.12. Drainage scenario: Effect of m on the relative difference (%) for total amount of drained moisture at 1 day between HYDRUS-1D and the peridynamic simulation using a uniform influence function. For each horizon radius the relative difference decreases with increasing point density. Also, relative difference curves of smaller horizon radii are closer to 0%.

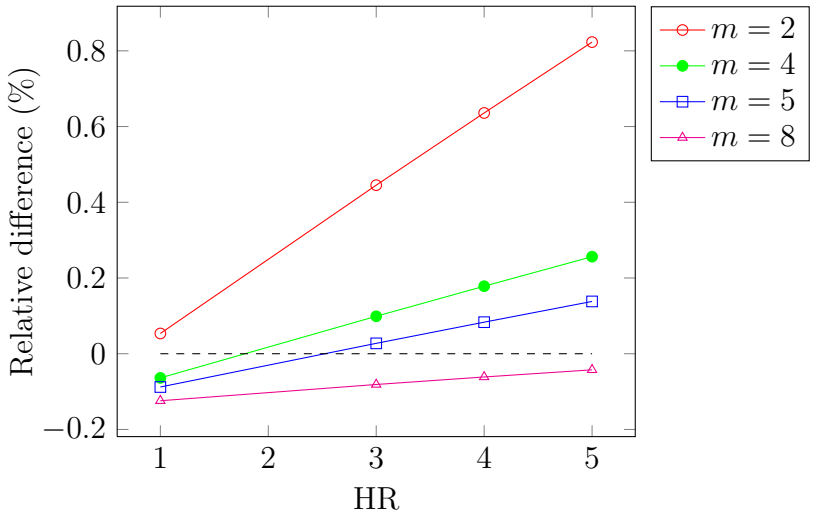

Fig. 2.13. Drainage scenario: Effect of δ on the relative difference (%) for total amount of drained moisture at 1 day between HYDRUS-1D and the peridynamic simulation using a uniform influence function. For each point density, m, the relative difference decreases with decreasing δ. Also, relative difference curves of higher m values are closer to 0%.

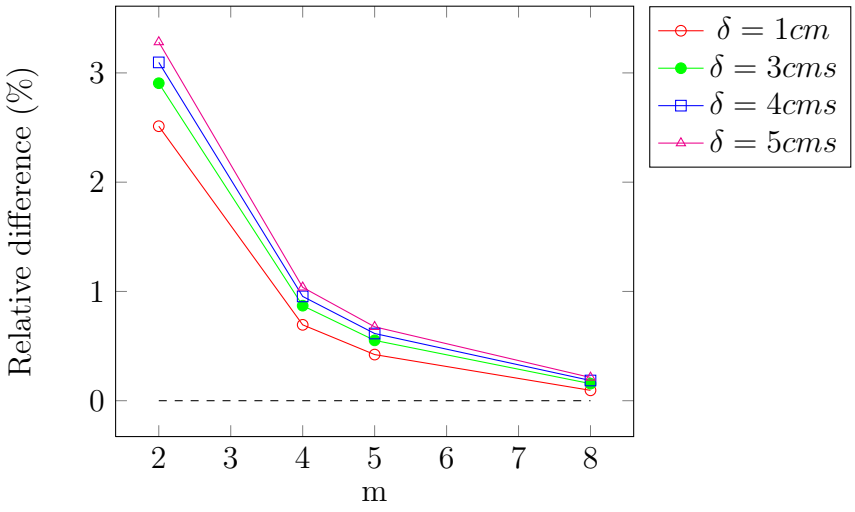

Fig. 2.14. Drainage scenario: Effect of m on the relative difference (%) for total amount of drained moisture at 1 day between HYDRUS-1D and the peridynamic simulation using a triangular influence function. For each horizon radius the relative difference decreases with increasing point density. Also, relative difference curves of smaller horizon radii are closer to 0%.

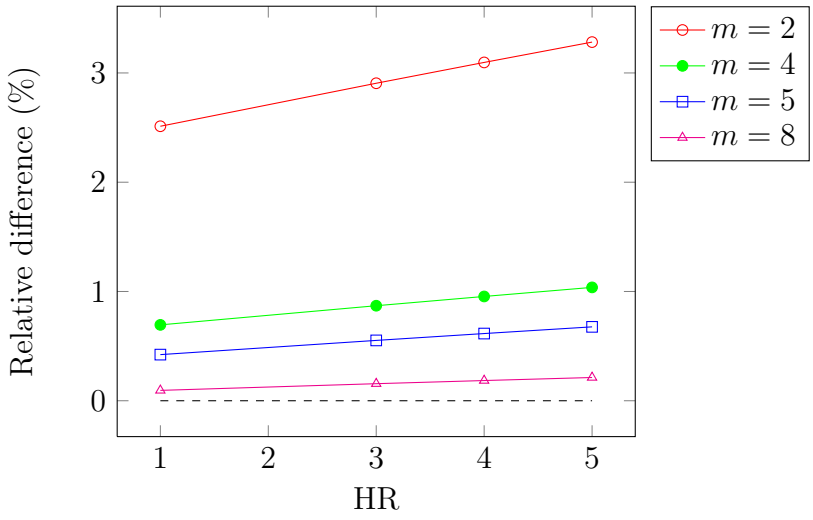

Fig. 2.15. Drainage scenario: Effect of δ on the relative difference (%) for total amount of drained moisture at 1 day between HYDRUS-1D and the peridynamic simulation using a triangular influence function. For each point density, m, the relative difference decreases with decreasing δ. Also, relative difference curves of higher m values are closer to 0%.

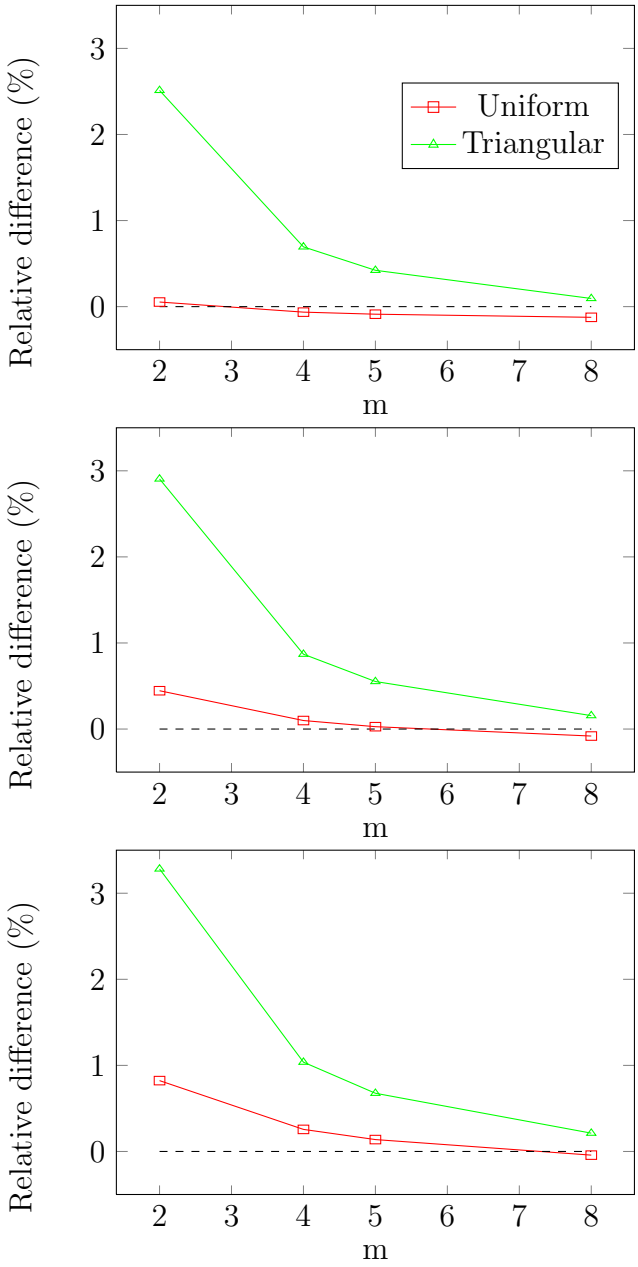

Fig. 2.16. Drainage scenario: Comparison between the effects of uniform and triangular influence function on the relative difference of total amount of drained moisture at 1 day. From top to bottom $\delta = 1, 3, 5cms$ respectively. I notice that as the horizon radius increases the performance of the triangular influence function with respect to the uniform influence function improves.

For the peridynamic model, all horizon radii are used. Initially all nodes except the one located at x = 300 cm are set to 10% saturation. The top and bottom boundary conditions are applied by adding boundary nodes from $x = 0cm$ to $x = -\delta$ for the lower boundary and are maintained at 10% saturation, and from $x = 300cm$, to $x = 300 + \delta cm$ for the top boundary condition and are maintained at saturation moisture content. The time step used is 0.5E-6 days.

Figure 2.17 is a plot of the moisture profile of the infiltration scenario recorded time at 0.5 day, 1 day and 2 days. The solid lines are the results using the classic formulation modeled using HYDRUS-1D. Overlayed in squares and triangles are the plots using the peridynamic formulation for the uniform and triangular influence functions respectively for a horizon radius $\delta = 1cm$ and a point density value $m = 4$. Following a visual inspection of the plots, I observe a very good agreement between the results of the peridynamic model and the classic model.

In order to obtain a more quantitative evaluation of the level of agreement between both methods, I will analyze more closely the results at 1 day. However, unlike the drainage simulations, using the relative difference in surface moisture content between the peridynamic model and HYDRUS-1D at some point in time as a benchmark is not adequate. In fact, comparing moisture content at any location in the column is not adequate for accuracy assessment. This is because during the simulated infiltration event, the advancing infiltration front is a narrow segment of the soil profile as evident in figure 2.17. Soil above the infiltration front is saturated, soil below it is near residual moisture content, and using points that happen to fall above or below the front at some point in time is not information bearing. Moisture content at the start of the front increases from near residual to saturation as the front advances over the short length of the front. Even slight variations in locating the front from one model to another, or from one grid length to another, will lead to large variations in the moisture content at some location within the front at some point in time. These variations lead to large relative differences in moisture content that are not necessarily a reflection of

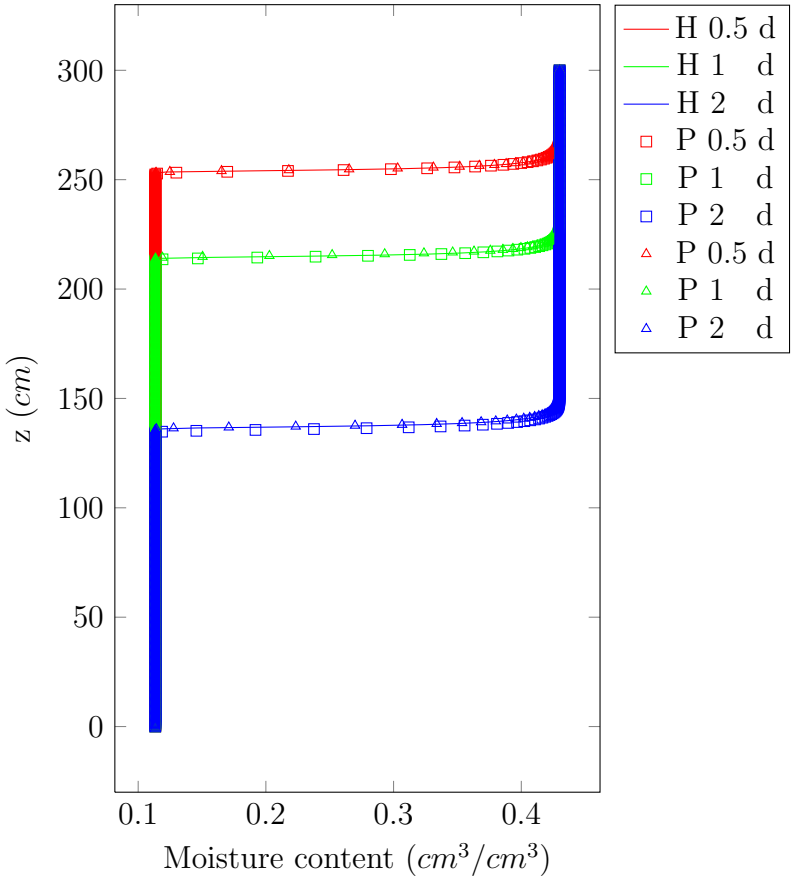

Fig. 2.17. Infiltration scenario: Moisture profile at 0.5, 1, and 2 days. HYDRUS-1D simulation results plotted as solid lines. Peridynamic simulation results for $\delta = 1cm$, $m = 5$. Uniform influence function results plotted as squares, triangular as triangles; only every 2 points are plotted for visibility.

the performance of the model and renders comparing points within the front uninformative as well.

On the other hand, using the location of the infiltration front at some point in time, or the amount of water infiltrated into the soil column from the beginning of the infiltration event up to any point in time is a better benchmark. Because the thickness of the infiltration front is small compared to the total soil thickness from the front to the surface, I will assume that the soil moisture profile may be approximated by a saturated column above a sharp infiltration front like the Green-Ampt model (Haws et al., 2005), and the total amount of infiltrated water and the depth to the infiltration front become essentially equivalent.

Figure 2.18 is a plot of the relative difference of the infiltration depth between HYDRUS-1D and the peridynamic simulations for the various horizon radii used ($\delta = 1, 3, 4, 5cm$), plotted versus the point density value m using a uniform influence function. As expected, for each horizon radius, the relative difference decreases with increasing m, as each point is capturing better the state of the soil within its horizon. In addition, the curves seem to be converging with those of smaller horizons having lower relative difference values.

This is confirmed by inspecting figure 2.19, which is a plot of the same relative difference but as a function of the horizon radius, with each curve grouping simulations with the same point density value m. In Figure 2.19, I observe for the same value of m the relative difference gets smaller with smaller horizon radius. This is because as the horizon gets smaller, the "nonlocality" of the model is getting smaller and approaching the classic local model formulation.

Figures 2.20 and 2.21 are identical to figures 2.18 and 2.19, but for triangular influence functions. Inspecting figure 2.20 I notice that for $m = 2$ the model yields an infiltration front that is above the classic solution, and that the relative difference decreases with increasing δ, which is contrary to what I expected. However, as m increases the model converges and smaller δ exhibit smaller relative difference.

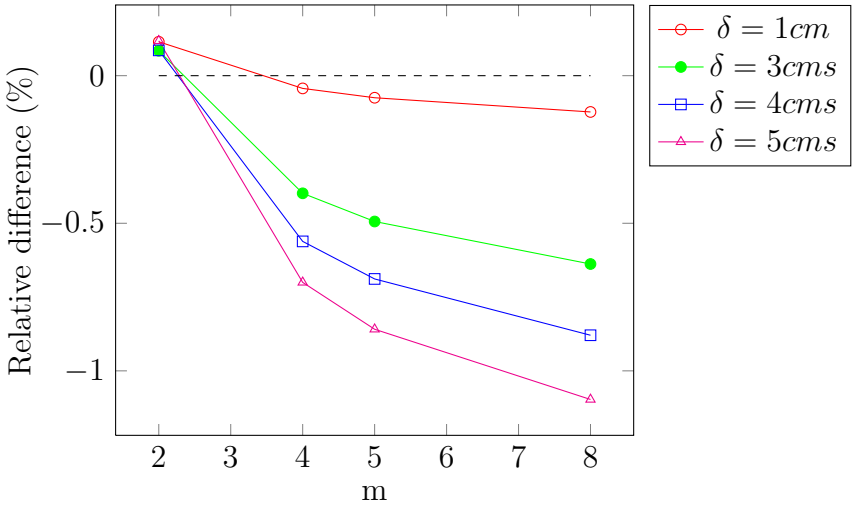

Fig. 2.18. Infiltration scenario: Effect of m on the relative difference (%) for soil surface moisture content at 1 day between HYDRUS-1D and the peridynamic simulation using a uniform influence function. For each horizon radius the relative difference decreases with increasing point density. Also, relative difference curves of smaller horizon radii are closer to 0%.

The graphs plotted in figure 2.22 compare the relative difference of the infiltration depth at 1 day using a uniform influence function and a triangular influence function. From top to bottom, I have plotted the curves for $\delta = 1, 3, 5cm$ versus m. I notice that the curves of the uniform influence function are increasing towards a limit and those of the triangular influence function are decreasing. I also notice that for each horizon radius, as m increases, curves of the uniform influence function and of the triangular influence function converge towards the same relative difference value, and that this value, although small — ranging from -2% for $\delta = 5cms$ to 0% for $\delta = 1cm$ — is different for each δ and increases with increasing δ.

This was not observed in the case of the drainage scenarios, where the curves for the uniform and triangular influence functions were both increasing towards smaller relative difference values. In these scenarios, although the relative difference values at the limit were larger in absolute value for larger δ, the difference was not as large. These observations may be attributed to the difference between the drainage moisture profile and the infiltration moisture profile. For drainage, the gradients of moisture, matric head, and hydraulic conductivity are smooth and change slowly; whereas in the case of infiltration, suction head increases several orders of magnitude over the short length of the infiltration front, and the hydraulic conductivity decreases several orders of magnitude over the same distance.

In the presence of these sharp changes, as the horizon radius increases, the center of a horizon located within, or intersecting with, the infiltration front, is getting influenced by an increasing number of points with very high suction pressure and has access to an increasing number of points with a higher hydraulic permeability and moisture content. This results in more moisture being transferred from points above the front to points below the front with increasing δ leading to a deeper infiltration front.

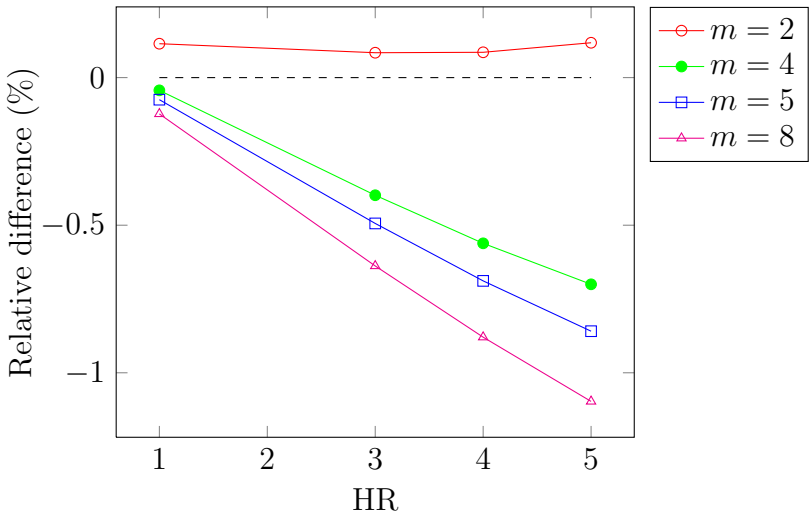

Fig. 2.19. Infiltration scenario: Effect of δ on the relative difference (%) for soil surface moisture content at 1 day between HYDRUS-1D and the peridynamic simulation using a uniform influence function. For each point density, m, the relative difference decreases with decreasing δ. Also, relative difference curves of higher m values are closer to 0%.

As for the reversed direction of the relative difference curves for the model using the triangular influence function, this may be due the reduced influence of the points farther away from a horizon center.

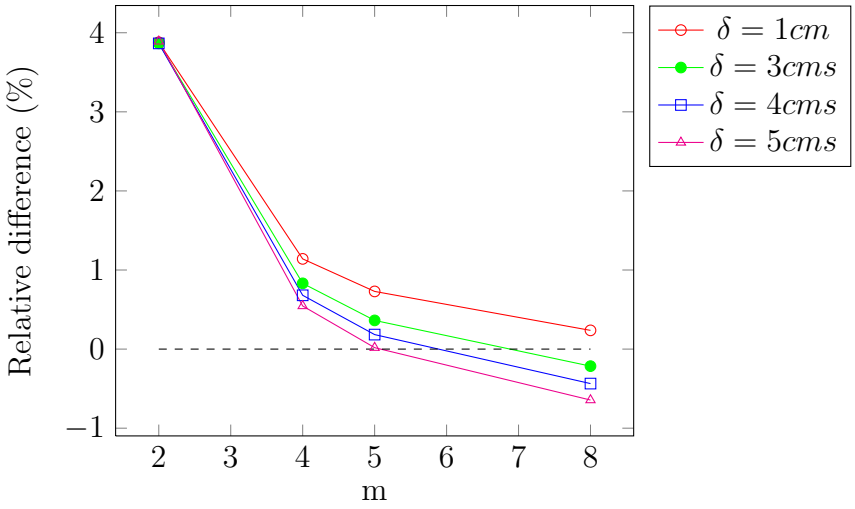

Fig. 2.20. Infiltration scenario: Effect of m on the relative difference (%) for soil surface moisture content at 1 day between HYDRUS-1D and the peridynamic simulation using a triangular influence function. For each horizon radius the relative difference decreases with increasing point density.

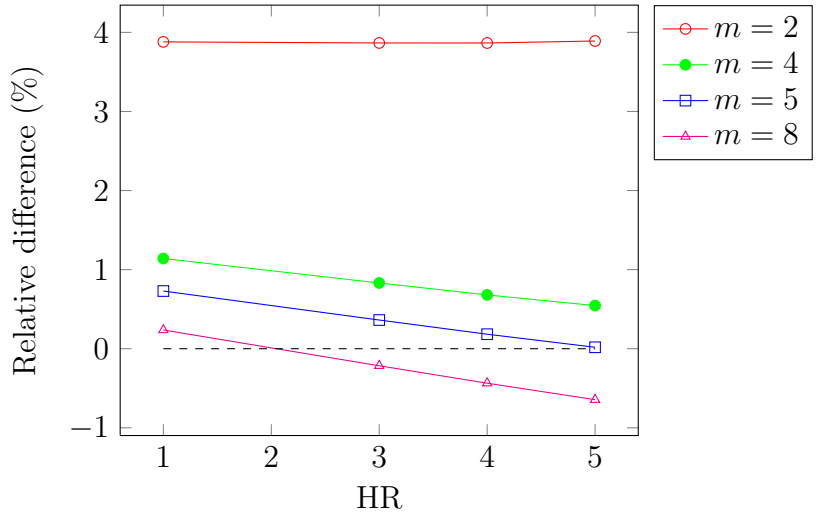

Fig. 2.21. Infiltration scenario: Effect of δ on the relative difference (%) for soil surface moisture content at 1 day between HYDRUS-1D and the peridynamic simulation using a triangular influence function.

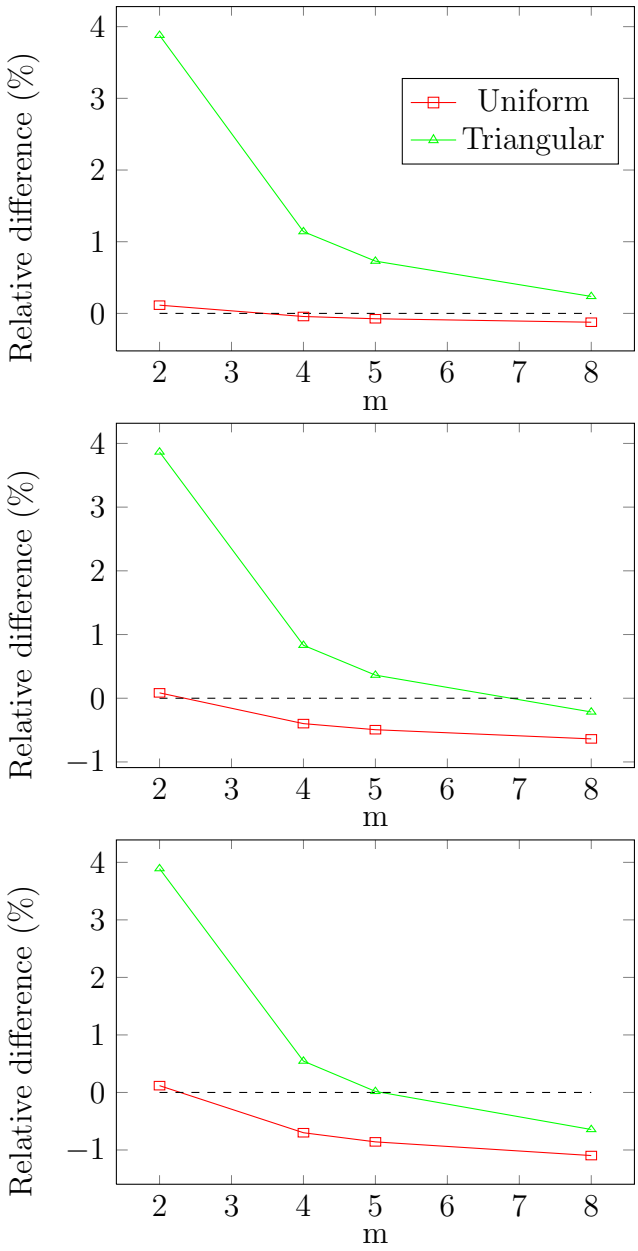

Fig. 2.22. Infiltration scenario: Comparison between the effects of uniform and triangular influence function on the relative difference of surface moisture content at 1 day. From top to bottom $\delta = 1, 3, 5cms$ respectively. I notice that as the density of point (m) increses, the relative difference curves for the triangular and the uniform influence function converge. And as the radius of the horizon decreases the curves converge with increasing m towards a smaller relative difference.

2.7 Conclusion

In this paper I derived a nonlocal derivative free alternative of the Richards Equation. The absence of spatial derivative allows for the simulation of domains with internal evolving singularities, a feature of soils with a high shrink/swell potential.

Using the derived model, I simulated drainage and infiltration in 1D, for several horizon radii ($\delta = 1, 3, 4, 5cms$), and point densities ($m = 2, 4, 5, 8$). I repeated the same simulation using the classic local formulation using HYDRUS-1D (Simunek et al., 2005).

For both cases — drainage and infiltration — I noticed that increasing the number of points per horizon leads to an increased agreement between the peridynamic model and the classic model. I also noticed that with a reduction in the horizon radius, I also observe an increased agreement between the models. I also observe that overall the triangular influence function leads to a higher level of agreement between both models.

Having said that, the results of the peridynamic model are in good agreement with those of the classic model as the values of the absolute value of the relative difference between the models for a horizon radius $\delta = 1cms$ and a point density value $m = 8$ remained lower than 0.2%, and it increased to only 1.0% for $\delta = 4cms$ with $m = 4$.

2.8 References

Abou Najm, M., Mohtar, R. H., Weiss, J., and Braudeau, E. (2009). Assessing internal stress evolution in unsaturated soils. *Water Resources Research*, 45(5):n/a–n/a.

Abou Najm, M. R., Jabro, J. D., Iversen, W. M., Mohtar, R. H., and Evans, R. G. (2010). New method for the characterization of three-dimensional preferential flow paths in the field. *Water Resources Research*, 46(2):n/a–n/a.

Braudeau, E. and Mohtar, R. H. (2006). Modeling the swelling curve for packed soil aggregates using the pedostructure concept. *Soil Science Society of America Journal*, 70(2):494.

Braudeau, E., Mohtar, R. H., El Ghezal, N., Crayol, M., Salahat, M., and Martin, P. (2009). A multi-scale "soil water structure" model based on the pedostructure concept. *Hydrology and Earth System Sciences Discussions*, 6(1):1111–1163.

Buckingham, E. (1907). Studies on the movement of soil moisture: Ii the capillary potential of soil moisture.

Chertkov, V. Y. (2002). Modelling cracking stages of saturated soils as they dry and shrink. *European Journal of Soil Science*, 53(1):105–118.

Darcy, H. (1856). *Les fontaines publiques de la ville de dijon. Exposition et application des principes à suivre et des formules à employer dans les questions de distribution d'eau: Ouvrage terminé par un appendice relatif aux fournitures d'eau de plusieurs villes au filtrage des eaux et à la fabrication des tuyaux de fonte, de plomb, de tole et de bitume*. Dalmont.

Davidson, S. E. and Page, J. B. (1956). Factors influencing swelling and shrinking in soils. *Soil Science Society of America Journal*, 20(3):320–324.

Dinka, T. M. (2012). Review paper: Challenges and limitations in studying the shrink-swell and crack dynamics of vertisol soils. *Open Journal of Soil Science*, 02(02):82–90.

Greco, R. (2002). Preferential flow in macroporous swelling soil with internal catchment: Model development and applications. *Journal of Hydrology*, 269(3–4):150–168.

Greve, A., Andersen, M. S., and Acworth, R. I. (2010). Investigations of soil cracking and preferential flow in a weighing lysimeter filled with cracking clay soil. *Journal of Hydrology*, 393(1):105–113.

Haws, N. W., Rao, P. S. C., Simunek, J., and Poyer, I. C. (2005). Single-porosity and dual-porosity modeling of water flow and solute transport in subsurface-drained fields using effective field-scale parameters. *Journal of Hydrology*, 313(3–4):257–273.

Jarvis, N. J. (2007). A review of non-equilibrium water flow and solute transport in soil macropores: Principles, controlling factors and consequences for water quality. *European Journal of Soil Science*, 58(3):523–546.

Kilic, B. and Madenci, E. (2010). Peridynamic theory for thermomechanical analysis. *Advanced Packaging, IEEE Transactions on*, 33(1):97 –105.

Lehoucq, R. and Silling, S. (2008). Force flux and the peridynamic stress tensor. *Journal of the Mechanics and Physics of Solids*, 56(4):1566–1577.

Liu, W. and Hong, J.-W. (2012). Discretized peridynamics for brittle and ductile solids. *International Journal for Numerical Methods in Engineering*, 89(8):1028–1046.

Richards, L. A. (1931). Capillary conduction of liquids through porous mediums. *Physics*, 1(5):318–333.

Sanders, E. C., Abou Najm, M. R., Mohtar, R. H., Kladivko, E., and Schulze, D. (2012). Field method for separating the contribution of surface-connected preferential flow pathways from flow through the soil matrix. *Water Resources Research*, 48(4):n/a–n/a.

Seleson, P. and Parks, M. (2011). On the role of the influence function in the peridynamic theory. *International Journal for Multiscale Computational Engineering*, 9(6):689–706.

Silling, S. (2000). Reformulation of elasticity theory for discontinuities and long-range forces. *Journal of the Mechanics and Physics of Solids*, 48(1):175–209.

Silling, S. and Askari, E. (2005). A meshfree method based on the peridynamic model of solid mechanics. *Computers & Structures*, 83(17–18):1526–1535.

Silling, S., Lehoucq, R., Aref, H., and van der Giessen, E. (2010). Peridynamic theory of solid mechanics. In *Advances in Applied Mechanics*, volume Volume 44, pages 73–168. Elsevier.

Simunek, J., Sejna, M., and Van Genuchten, M. (2005). The HYDRUS-1D software package for simulating the one-dimensional movement of water, heat, and multiple solutes in variably-saturated media. *University of California, Riverside, Research reports*, 240.

Van Genuchten, M. T. (1980). A closed-form equation for predicting the hydraulic conductivity of unsaturated soils. *Soil Science Society of America Journal*, 44(5):892–898.

CHAPTER 3. PERIDYNAMIC MODEL FOR TRANSIENT MOISTURE FLOW THROUGH UNSATURATED SOILS IN 2D

3.1 Abstract

A two-dimensional peridynamic model for transient flow in unsaturated, heterogeneous, and anisotropic soils is presented. The model formulation is an extension of the peridynamic flow model in one dimension. It is a nonlocal alternative to the classical continuum mechanics formulation that addresses the failure of the classic, local formulation to represent moisture flow in domains with evolving cracks. It is based on the peridynamic model for solid mechanics, where differential equations are replaced by derivative free functional integrals. Peridynamic expressions of the rate of change in moisture content, moisture flux, and flow power are derived. Relationships between the peridynamic hydraulic conductivity and the classic hydraulic conductivity for uniform, and linear influence functions are also derived. Validation scenarios of moisture redistribution and drainage are simulated using the peridynamic model and a classic flow model. Their results are presented and compared.

3.2 Introduction

Within the classic framework of continuum mechanics, the flux of moisture in two dimensions is expressed as a function of the gradient of the hydraulic head. In the case of unsaturated soils the flux is given by the modified Darcy-Buckingham law (Equation 3.1) (Darcy, 1856, Buckingham, 1907).

$$\boldsymbol{q} = -\boldsymbol{K}(h_m)\nabla\left(h_m + h_g\right). \tag{3.1}$$

$$\nabla = \frac{\partial}{\partial x}\hat{\boldsymbol{i}} + \frac{\partial}{\partial z}\hat{\boldsymbol{k}}. \tag{3.2}$$

$$\boldsymbol{K}(h_m) = \begin{vmatrix} K_{xx}(h_m) & K_{xz}(h_m) \\ K_{zx}(h_m) & K_{zz}(h_m) \end{vmatrix}. \tag{3.3}$$

Where $\boldsymbol{q}$ is the moisture flux vector, ∇ is the gradient operator (Equation 3.2), $\hat{\boldsymbol{i}}$ and $\hat{\boldsymbol{k}}$ are the standard basis for plane xy, h_m is the soil matric head, z is the elevation head, and $\boldsymbol{K}$ is a second-order symmetric tensor describing the hydraulic conductivity of a two-dimensional medium as a function of the matric head (Equation 3.3). The normal components of the flux vector q_x and q_z in the x and y directions respectively are given by Equations 3.4 and 3.5.

$$\boldsymbol{q}_x = -K_{xx}(h_m)\frac{\partial\left(h_m + h_g\right)}{\partial x}\hat{\boldsymbol{i}} - K_{xz}(h_m)\frac{\partial\left(h_m + h_g\right)}{\partial z}\hat{\boldsymbol{i}}. \tag{3.4}$$

$$\boldsymbol{q}_z = -K_{zx}(h_m)\frac{\partial\left(h_m + h_g\right)}{\partial x}\hat{\boldsymbol{k}} - K_{zz}(h_m)\frac{\partial\left(h_m + h_g\right)}{\partial z}\hat{\boldsymbol{k}}. \tag{3.5}$$

Assuming, without any loss of generality, that the principal axes of conductivity coincide with the plane axes, the tensor $\boldsymbol{K}$ becomes a diagonal matrix and the flux becomes:

$$\begin{aligned} \boldsymbol{q} &= \boldsymbol{q}_x + \boldsymbol{q}_z \\ &= -K_{xx}(h_m)\frac{\partial(h_m + h_g)}{\partial x}\hat{\boldsymbol{i}} - K_{zz}(h_m)\frac{\partial(h_m + h_g)}{\partial z}\hat{\boldsymbol{k}}. \end{aligned} \tag{3.6}$$

Applying the continuity equation to Equation 3.6, I get a nonlinear partial differential equation for the rate of change of moisture content expressed as the divergence of the moisture flux vector field. This expression is known as the Richard's Equation (Equation 3.7) (Richards, 1931).

$$\begin{aligned} \frac{\partial\theta}{\partial t} &= \nabla.\boldsymbol{q} + S \\ &= -\frac{\partial}{\partial x}\left[K_{xx}(h_m)\frac{\partial(h_m + h_g)}{\partial x}\right] - \frac{\partial}{\partial z}\left[K_{zz}(h_m)\frac{\partial(h_m + h_g)}{\partial z}\right] + S. \end{aligned} \tag{3.7}$$

Where the term S is equal to the rate of moisture added or removed by any external sources or drains of moisture.

As long as the problem is well-behaved and the assumption of continuity holds for all time, Equation 3.7 remains valid. However, naturally occurring soils, especially those that are finely textured, may exhibit shrinking and swelling behavior that depends on moisture content (Davidson and Page, 1956, Dinka, 2012, Braudeau and Mohtar, 2006). Depending on the mechanical properties of the soil, this behavior may trigger the formation of dessication cracks that open during drying phases and close during wetting phases (Chertkov, 2002, Greco, 2002, Jarvis, 2007, Abou Najm et al., 2009, Abou Najm et al., 2010). These cracks affect the dynamics of moisture and solute movement into and within the soil by providing a preferential flow path of moisture into deeper layers (Greve et al., 2010, Braudeau et al., 2009, Sanders et al., 2012), which in turn, influences the shrinking and swelling of the soil and the process of crack formation.

Because of this interdependence between processes of crack formation and moisture flow, and in order to better understand the mechanisms of formation and evolution of these types of cracks, and analyze their potential impact on moisture flow, I need to develop a model that is capable of simulating both processes of solid mechanics and fracture and moisture flow in a soil medium in a coupled manner. However, the emergence and evolutions of these cracks render the Richard's Equation unsuitable to describe moisture flow since they violate the assumption of continuity and lead to undefined gradients at their tips and on their surfaces.

The one-dimensional peridynamic flow model derived previously addresses this issue by replacing the classic, local, continuum mechanics formulation with a nonlocal functional integral, free of spatial derivatives, which remains valid even in the presence of evolving discontinuities. In this study, I will extend the peridynamic formulation to two dimensions and demonstrate its ability to simulate transient flow in heterogeneous and anisotropic soils.

3.3 Peridynamic flow model in 2D

The peridynamic model for moisture flow in one dimension was derived in the previous chapter. The model is a reformulation of flow problem in a nonlocal framework, and the particular mechanics of matter and energy flow adopted lead to a mathematical expression free of any spatial derivatives, and replaced the standard differential equation with a functional integral. The model is based on Silling's reformulation of elasticity which is aimed at simulating mechanical deformations of bodies where singularities such as cracks may form and evolve during the simulation (Silling, 2000, Silling et al., 2010). In the peridynamic model for solid mechanics, the cracks become part of the solution instead of a mathematical difficulty that requires special numerical treatment and prior knowledge of the crack location.

In the classical continuum mechanics framework, the rate of change of some quantity at some material point in a body is proportional to the divergence of the vector field carrying this quantity at the same point. In the case of solid mechanics and deformations, the quantity of interest is the momentum, and the vector field is the displacement field. In the case of moisture flow in porous media in general, and soil in specific, the quantity of interest is the moisture content and the vector field carrying this quantity is the moisture flux.

In a peridynamic framework, the rate of change of some quantity at some material point in a body results from the influence on the point of interest exerted by other points in the body. These points can be the entire body or, for practical purposes, a subset of points that are within a certain distance of the point of interest (Silling, 2000, Silling et al., 2010). This contrasts with the classic continuum mechanic formulation, where interactions are between points separated by an infinitesimal distance. It is in that sense that a peridynamic model can be described as nonlocal, and the maximum distance between interacting points is a measure of its nonlocality.

Two variants exist for the peridynamic model for mechanics of solids: the bond-based model (Silling, 2000), and the state-based model (Silling et al., 2007). The differences concern the modality of the influence that the points exercise on each other. In the bond-based model, the influence on some point is due to pair-wise interactions between that point and all other points influencing it via a force density function with units of force per volume squared, the volume of the first point times the volume of the second. In the state-based model, the influence is due to the collective state of the influencing points instead of the sum of their individual states. The state-based model allows for simulating a larger number of behaviors and material properties, such as the deformation of materials with a Poisson ratio different from 0.25, which is the only Poisson ratio value that the bond-based model is capable of modeling due to the pair-wise interactions.

The peridynamic flow model is based on the bond-based model for solid mechanics (Silling, 2000, Silling et al., 2010). Similar to the one-dimensional model derived previously, in two dimensions, or three dimensions for that matter, the change in moisture content at any point is due to the pair-wise exchange of moisture between it and all other points within a certain distance. These pair-wise exchanges conceptualize moisture flow via one dimensional pipes that I call peripipes. The flow through each peripipe is described by a flow density function that gives the rate of moisture flow from one node to the other per unit volume squared, the volume of the first point times the volume of the second, driven by the hydraulic head at its node. The hydraulic parameters of each peripipe are related to the hydraulic parameters of the medium at the nodes, and are given by a transformation from the classic parameter space to the peridynamic parameter space. This transformation is derived by requiring that simulations of a problem using either model yield similar results.

Consider the the body of soil $\boldsymbol{\Omega}$ in Figure 3.1. Each point $\boldsymbol{x}$ in $\boldsymbol{\Omega}$ has a volume $\mathrm{d}V_x$, and has a moisture content of $\theta(\boldsymbol{x}, t)$ and is at some total hydraulic potential $H(\boldsymbol{x}, t) = h_m(\boldsymbol{x}, t) + h_g(\boldsymbol{x}, t)$. Suppose that the maximum distance separating two

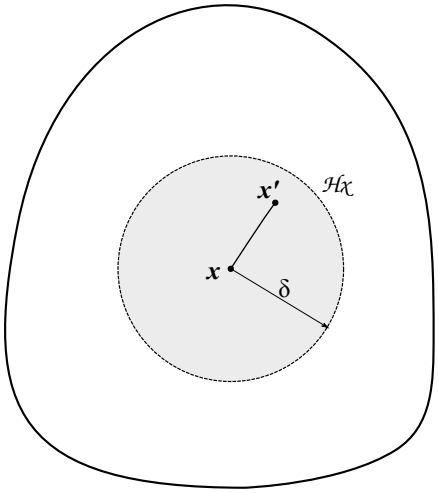

Fig. 3.1. Peridynamic medium representation. Point $\boldsymbol{x}$ is influenced by all points within its horizon. $\mathcal{H}_x$ is the horizon of $\boldsymbol{x}$, δ is the radius of the horizon.

interacting points is δ. Let me define for every point $\boldsymbol{x}$ in $\boldsymbol{\Omega}$ the set $\mathcal{H}_x$ as the set of points in $\boldsymbol{\Omega}$ that are within a distance δ from $\boldsymbol{x}$ (Equation 3.8); these are the points that would exercise an influence on $\boldsymbol{x}$. I call the set $\mathcal{H}_x$ the horizon of point $\boldsymbol{x}$, and δ the radius of the horizon.

$$\mathcal{H}_x = \{\boldsymbol{x'} \in \boldsymbol{\Omega} \mid 0 \leq \|\boldsymbol{x'} - \boldsymbol{x}\| \leq \delta\}\,. \tag{3.8}$$

Now consider the point $\boldsymbol{x'}$ inside the horizon of $\boldsymbol{x}$ with $H(\boldsymbol{x'}, t) = h_m(\boldsymbol{x'}, t) + h_g(\boldsymbol{x'}, t)$. The influence exerted by $\boldsymbol{x'}$ on $\boldsymbol{x}$, which is the rate of change of the volumetric moisture content at $\boldsymbol{x}$ per unit volume of $\boldsymbol{x'}$, is given by the flow density function J:

$$J(\boldsymbol{x}, \boldsymbol{x'}, h_m(\boldsymbol{x}, t), h_m(\boldsymbol{x'}, t)). \tag{3.9}$$

Multiplying Equation 3.9 by the volume of $\boldsymbol{x'}$, $\mathrm{d}V_{x'}$, gives me the rate of change of the volumetric moisture content at $\boldsymbol{x}$ due to $\boldsymbol{x'}$:

$$\frac{\partial \theta(\boldsymbol{x}|\boldsymbol{x'}, t)}{\partial t} = J(\boldsymbol{x}, \boldsymbol{x'}, h_m(\boldsymbol{x}, t), h_m(\boldsymbol{x'}, t))\mathrm{d}V_{x'}. \tag{3.10}$$

Invoking the principle of conservation of mass, I imply that the rate of change of the volumetric moisture content at point $\boldsymbol{x}$ at every time t is equal to the sum of all the rates of change of moisture content due to all the points within the horizon of $\boldsymbol{x}$:

$$\frac{\partial\theta(\boldsymbol{x},t)}{\partial t} = \int_{\mathcal{H}_x} \frac{\partial\theta(\boldsymbol{x}|\boldsymbol{x'},t)}{\partial t}\mathrm{d}V_{x'}. \tag{3.11}$$

Replacing the integrand of the right hand side of Equation 3.11 by the right hand side of Equation 3.10, and replacing $\mathrm{d}V_{x'}$ by its two-dimensional equivalent $\mathrm{d}A_{x'}$, I can write, for convenience, the integral in polar coordinates with point $\boldsymbol{x}$ at the origin of the system:

$$\frac{\partial\theta(\boldsymbol{x},t)}{\partial t} = \int_0^{2\pi}\int_0^r J(\boldsymbol{x},\boldsymbol{x'},h_m(\boldsymbol{x},t),h_m(\boldsymbol{x'},t))\, r\mathrm{d}r\mathrm{d}\phi + S(\boldsymbol{x},t). \tag{3.12}$$

Where $S(\boldsymbol{x},t)$ is a source/sink term added to account for a potential local source or sink, e.g.: pumping well, irrigation system, root uptake, or a second embedded porosity.

If a crack happens to intersect with the horizon of point $\boldsymbol{x}$, its effect is accounted for by severing the influence on $\boldsymbol{x}$ of any interaction that intersects with it. This is captured by multiplying J by a term D which takes the value zero if the interaction is severed; otherwise it is one. Equation 3.12 becomes:

$$\frac{\partial\theta(\boldsymbol{x},t)}{\partial t} = \int_0^{2\pi}\int_0^r D(\boldsymbol{x}\boldsymbol{x'},t)J(\boldsymbol{x},\boldsymbol{x'},h_m(\boldsymbol{x},t),h_m(\boldsymbol{x'},t))\, r\mathrm{d}r\mathrm{d}\phi + S(\boldsymbol{x},t), \tag{3.13}$$

$$D(\boldsymbol{x}\boldsymbol{x'},t) = \begin{cases} 1, & \text{if interaction } xx' \text{ is present,} \\ 0, & \text{if interaction } xx' \text{ is severed.} \end{cases} \tag{3.14}$$

Let me shift my attention back to the definition of peripipes and work towards deriving the expression of their associated flow density function J. I have already stated that peripipes are two-dimensional entities; I will now suppose the following additional peripipe properties:

1. Moisture flows along the length of the peripipes and does not cross their longitudinal boundaries (pairwise interactions).

2. Peripipes are purely resistive, they have zero reactance and their response is proportional to the applied hydraulic potential at their end-nodes.
3. Peripipes have a uniform conductivity.
4. Peripipes have a length equal to the euclidean distance between their end-nodes.

Consider the prototype peripipe $\boldsymbol{xx'}$ connecting points $\boldsymbol{x}$ and $\boldsymbol{x'}$ (Figure 3.1). Points $\boldsymbol{x}$ and $\boldsymbol{x'}$ have volumes $\mathrm{d}V_x$ and $\mathrm{d}V_{x'}$ respectively, and are at a hydraulic potential of $H(\boldsymbol{x},t) = h_m(\boldsymbol{x},t) + h_g(\boldsymbol{x},t)$ and $H(\boldsymbol{x'},t) = h_m(\boldsymbol{x'},t) + h_g(\boldsymbol{x'},t)$. The material of peripipe $\boldsymbol{xx'}$ has a conductivity $\kappa(\boldsymbol{xx'},t)$. Properties one and two imply that the flow of moisture from $\boldsymbol{x'}$ towards $\boldsymbol{x}$ is given by:

$$Q_{xx'} = C(\boldsymbol{xx'},t)[H(\boldsymbol{x'},t) - H(\boldsymbol{x},t)]. \tag{3.15}$$

Where $Q_{x'x}$ is the amount of moisture exchanged per unit time, and $C(\boldsymbol{xx'},t)$ is the lumped conductance of peripipe $\boldsymbol{xx'}$ which, from properties three and four, is given by:

$$C(\boldsymbol{xx'},t) = \frac{\kappa(\boldsymbol{xx'},t)}{||\boldsymbol{x'} - \boldsymbol{x}||}. \tag{3.16}$$

Where $||\boldsymbol{x'} - \boldsymbol{x}||$ is the length of $\boldsymbol{xx'}$. Plugging Equation 3.16 in Equation 3.15, I get:

$$Q_{xx'} = \frac{\kappa(\boldsymbol{xx'},t)}{||\boldsymbol{x'} - \boldsymbol{x}||}[H(\boldsymbol{x'},t) - H(\boldsymbol{x},t)]. \tag{3.17}$$

Remember that $Q_{xx'}$ is the rate of moisture being exchanged between $\boldsymbol{x}$ and $\boldsymbol{x'}$. Dividing $Q_{xx'}$ by $\mathrm{d}V_x$, the volume of $\boldsymbol{x}$, I get the rate of change in volumetric moisture content at $\boldsymbol{x}$ due to its interaction with $\boldsymbol{x'}$ per unit time. If I further divide by $\mathrm{d}V_{x'}$, the volume of $\boldsymbol{x'}$, I get the change in volumetric moisture content at $\boldsymbol{x}$ per unit volume of $\boldsymbol{x'}$ per unit time, which is the definition of the flow density function J. Redefining κ as the conductivity of the peripipe normalized with respect to volume squared, I get:

$$J(\boldsymbol{x},\boldsymbol{x'},h_m(\boldsymbol{x},t),h_m(\boldsymbol{x'},t)) = \frac{\kappa(\boldsymbol{xx'},t)}{\|\boldsymbol{x'} - \boldsymbol{x}\|}(H(\boldsymbol{x'},t) - H(\boldsymbol{x},t)). \tag{3.18}$$

Combining Equations 3.18 and 3.13, I get the following expression for the rate of change in moisture content at point $\boldsymbol{x}$ at time t:

$$\frac{\partial\theta(\boldsymbol{x},t)}{\partial t} = \int_0^{2\pi}\int_0^{r} D(\boldsymbol{x}\boldsymbol{x'},t)\frac{\kappa(\boldsymbol{x}\boldsymbol{x'},t)}{\|\boldsymbol{x'}-\boldsymbol{x}\|}(H(\boldsymbol{x'},t)-H(\boldsymbol{x},t))\,r\mathrm{d}r\mathrm{d}\phi + S(\boldsymbol{x},t). \quad (3.19)$$

3.4 Peridynamic flux and flow power in 2D

3.4.1 Peridynamic flux equation in 2D

The definition of moisture flux across some surface $\mathcal{S}$ is the amount of moisture flowing across the surface $\mathcal{S}$ in a normal direction per unit area of the surface per unit time. In the classic formulation of two-dimensional flow problems, it is given by Equation 3.1.

In order to derive the equation of moisture flux for a peridynamic flow model, let me restate the definition as follows: moisture flux across some surface is the net amount of moisture exchanged between points located on one side of the surface with points located on the other side of the surface, per unit area of that surface, per unit time. In the proposed peridynamic model, moisture exchange is driven by pairwise interactions via peripipes connecting material points, and the flux is the sum of all moisture exchanged due to pairwise interactions between points on one side of the surface with points on the other side, per unit area per unit time.

In Figure 3.2, I have a two-dimensional soil column in a polar coordinate system with pole $O(0,0)$. Suppose this medium has a horizon radius δ, I would like to evaluate the moisture flux normal to the surface $\mathcal{S}$ with $\phi = 0$. The flux I am after is the sum of the components normal to $\mathcal{S}$ of the moisture flows in all peripipes transporting moisture from points on one side of $\mathcal{S}$, shown in green in Figure 3.2a, to points on one side of $\mathcal{S}$, shown in red in Figure 3.2a, and passing through point O.

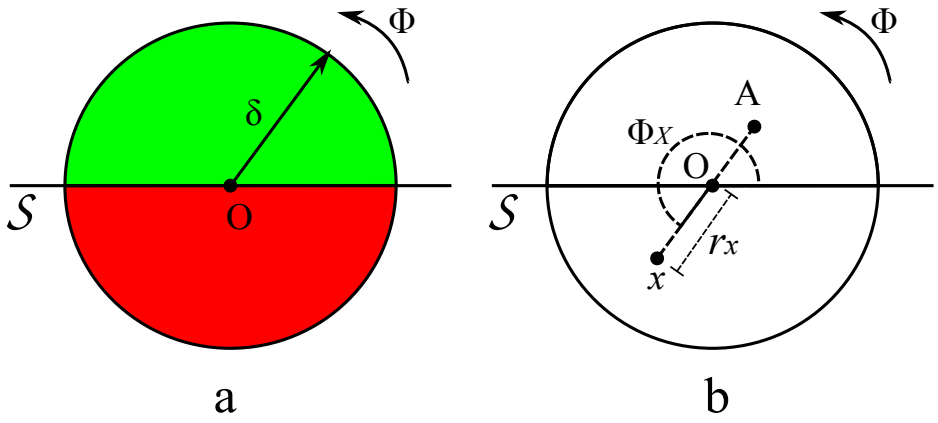

Fig. 3.2. Peridynamic moisture flux calculation diagram.

To simplify the following argument, I adopted the convention that the distance r and the angle ϕ are always positive. Consider point $\boldsymbol{x}(r_x, \phi_x)$ with $r_x \leq \delta$ (Figure 3.2b). Its horizon, $\mathcal{H}_x$, is the entire disk of radius δ centered at $\boldsymbol{x}$. However, only the points forming the segment $[OA]$ with $\phi_{x'} = \phi_x - \pi$ and $0 \leq r_{x'} \leq (\delta - r_x)$ are connected to point $\boldsymbol{x}$ with peripipes that pass through O. Points with $\phi \neq \phi_x - \pi$ are not colinear with (xO) and will not pass through O, and points on the line (xO) with $r > (\delta - r_x)$ are simply outside $\mathcal{H}_x$ and are not connected to point $\boldsymbol{x}$.

Taking the points $\boldsymbol{x}$ and $\boldsymbol{x'} \in [OA]$, the moisture flowing across O due to peripipe $\boldsymbol{xx'}$ is given by:

$$\boldsymbol{q}(O|\boldsymbol{xx'}) = -\frac{\kappa(\boldsymbol{xx'})}{(r_x + r_{x'})}\Delta H(\boldsymbol{xx'})\,\mathrm{d}V_{x'}. \tag{3.20}$$

Where $\Delta H(\boldsymbol{xx'}) = H(\boldsymbol{x'}, t) - H(\boldsymbol{x}, t)$, and t was dropped from $\kappa(., t)$ and $H(., t)$ for conciseness.

Multiplying Equation 3.20 by $sin(\phi_{x'} - \pi)$ I get the component normal to surface $\mathcal{S}$:

$$\boldsymbol{q}_{\perp\mathcal{S}}(O|\boldsymbol{xx'}) = -\frac{\kappa(\boldsymbol{xx'})}{(r_x + r_{x'})}\Delta H(\boldsymbol{xx'})sin(\phi_{x'} - \pi)\,\mathrm{d}V_{x'}. \tag{3.21}$$

To get the total contribution of point $\boldsymbol{x}$ to the flux across $\mathcal{S}$ I account for all the contribution of $\boldsymbol{x}$ due to all points of $[OA]$ by integrating over $0 \leq \ r'_x \leq (\delta - r_x)$ with $\phi_{x'} = \pi - \phi_x$. It is given by:

$$\boldsymbol{q}_{\perp\mathcal{S}}(O|\boldsymbol{x}) = -\int_0^{\delta - r_x} \frac{\kappa(\boldsymbol{x}\boldsymbol{x'})}{(r_x + r_{x'})} \Delta H(\boldsymbol{x}\boldsymbol{x'}) sin(\phi_{x'} - \pi)\, \mathrm{d}V_{x'}. \tag{3.22}$$

Replacing $\mathrm{d}V_{x'}$ by $(r_x + r_{x'})\mathrm{d}r_{x'}\mathrm{d}\phi_{x'}$, and changing the integration variable from $r_{x'}$ to $r = (r_x + r_{x'})$, Equation 3.21 becomes:

$$\begin{aligned}\boldsymbol{q}_{\perp\mathcal{S}}(O|\boldsymbol{x}) &= -\int_{r_x}^{\delta} \frac{\kappa(\boldsymbol{x}\boldsymbol{x'})}{r} \Delta H(\boldsymbol{x}\boldsymbol{x'}) sin(\phi_{x'} - \pi)\, r\mathrm{d}r\mathrm{d}\phi_{x'}, \\ &= -\int_{r_x}^{\delta} \kappa(\boldsymbol{x}\boldsymbol{x'}) \Delta H(\boldsymbol{x}\boldsymbol{x'}) sin(\phi_{x'} - \pi)\, \mathrm{d}r\mathrm{d}\phi_{x'}. \end{aligned} \tag{3.23}$$

To get the contribution to the flux across $\mathcal{S}$ of the entire arc $(r_x, \pi \leq \phi_x \leq 2\pi)$ I integrate as follows:

$$\boldsymbol{q}_{\perp\mathcal{S}}(O|\boldsymbol{x}) = -\int_{\pi}^{2\pi}\int_{r_x}^{\delta} \kappa(\boldsymbol{x}\boldsymbol{x'}) \Delta H(\boldsymbol{x}\boldsymbol{x'}) sin(\phi_{x'} - \pi)\, \mathrm{d}r\mathrm{d}\phi_{x'}. \tag{3.24}$$

Integrating over $\delta \leq r_x \leq 0$, I get the contribution of the entire half horizon on one side of the surface $\mathcal{S}$ which is the total flux at O normal to $\mathcal{S}$. It is given by:

$$\boldsymbol{q}_{\perp\mathcal{S}}(O) = -\int_{\delta}^{0}\int_{\pi}^{2\pi}\int_{r_x}^{\delta} \kappa(\boldsymbol{x}\boldsymbol{x'}) \Delta H(\boldsymbol{x}\boldsymbol{x'}) sin(\phi_{x'} - \pi)\, \mathrm{d}r\mathrm{d}\phi_{x'}\mathrm{d}r_x. \tag{3.25}$$

For the flux at O normal to a surface S with angle ϕ, Equation 3.25 becomes:

$$\boldsymbol{q}_{\perp\mathcal{S}(\phi)}(O) = -\int_{\delta}^{0}\int_{\pi}^{2\pi}\int_{r_x}^{\delta} \kappa(\boldsymbol{x}\boldsymbol{x'}) \Delta H(\boldsymbol{x}\boldsymbol{x'}) sin(\phi_{x'} + \phi - \pi)\, \mathrm{d}r\mathrm{d}\phi_{x'}\mathrm{d}r_x. \tag{3.26}$$

This is similar to what Lehoucq and Silling proposed for the mechanical stress in the peridynamic model for solid mechanics (Lehoucq and Silling, 2008).

3.4.2 Peridynamic flow power equation in 2D

I will now derive the peridynamic expression for power dissipated by the flow of moisture within a porous medium at some point in space and time. Due to its simpler form, I will use this expression as an alternative to the peridynamic

flux equation in the subsequent section to derive the function of the peridynamic hydraulic conductivity.

Consider a point $\boldsymbol{x}$ in a body of soil modeled using the peridynamic flow model with a horizon radius δ. The power dissipated by moisture flow at point $\boldsymbol{x}$ is the power dissipated by the flow mobilized due to $\boldsymbol{x}$. This power is the power dissipated within each peripipe connected to $\boldsymbol{x}$.

I know that the power dissipated by flow of energy though a two port element is equal to the flow rate of the quantity carrying the energy times the potential difference driving the flow. For a peripipe $\boldsymbol{x}\boldsymbol{x'}$, the quantity carrying the energy is moisture, and the flow rate of moisture is given as flow per unit volume squared by the flow density function J (Equation 3.18). The potential difference driving the flow is the hydraulic potential difference across $\boldsymbol{x}\boldsymbol{x'}$. Multiplying J by the hydraulic potential difference across a peripipe will yield the power dissipated within the peripipe per unit volume squared, similar to how J is the flow per unit volume squared. It is given by:

$$P(\boldsymbol{x}\boldsymbol{x'}, t) = \frac{\kappa(\boldsymbol{x}\boldsymbol{x'}, t)}{\|\boldsymbol{x'} - \boldsymbol{x}\|}(H(\boldsymbol{x'}, t) - H(\boldsymbol{x}, t))^2. \tag{3.27}$$

Multiplying P by the volume of $\boldsymbol{x'}$ and integrating over the entire horizon of $\boldsymbol{x}$ gives me the power dissipated per unit volume of $\boldsymbol{x}$ due to all flows it mobilized across all peripipes connected to it. It is given by:

$$P(\boldsymbol{x}, t) = \frac{1}{2}\int_{\mathcal{H}_x} \frac{\kappa(\boldsymbol{x}\boldsymbol{x'}, t)}{\|\boldsymbol{x'} - \boldsymbol{x}\|}(H(\boldsymbol{x'}, t) - H(\boldsymbol{x}, t))^2 \,\mathrm{d}V_{x'}. \tag{3.28}$$

Where the factor $1/2$ was added because each peripipe is connected to two points, making the share of power dissipated of each one of these points of a half.

Integrating in a polar coordinates reference with pole $\boldsymbol{x}$ and with $\mathrm{d}V_{x'} = r\mathrm{d}r\mathrm{d}\Phi$, I get:

$$\begin{aligned} P(\boldsymbol{x}, t) &= \frac{1}{2}\int_0^{\delta}\int_0^{2\pi} \frac{\kappa(\boldsymbol{x}\boldsymbol{x'}, t)}{r}(H(\boldsymbol{x'}, t) - H(\boldsymbol{x}, t))^2 \, r\mathrm{d}r\mathrm{d}\phi, \\ &= \frac{1}{2}\int_0^{\delta}\int_0^{2\pi} \kappa(\boldsymbol{x}\boldsymbol{x'}, t)(H(\boldsymbol{x'}, t) - H(\boldsymbol{x}, t))^2 \,\mathrm{d}r\mathrm{d}\phi. \end{aligned} \tag{3.29}$$

3.5 Peridynamic hydraulic conductivity function in 2D

In this section I would like to work towards deriving the expression of the unmeasurable peridynamic hydraulic conductivity κ in terms of the measurable classic hydraulic conductivity K. I will achieve this by choosing a quantity that depends on the hydraulic conductivity and require that the value of this quantity be the same whether I use a peridynamic or a classic model. In the literature of peridynamic modeling of solid mechanics, two quantities have been used to establish the relationship between the peridynamic elastic constant and the classic elastic bulk modulus. The first is the deformation energy density stored in the body (Silling, 2000, Silling et al., 2010, Kilic and Madenci, 2010). The second is the mechanical stress induced by the deformation of a body (Liu and Hong, 2012).

In deriving the relationship between κ and K for the one-dimensional peridynamic flow model, I equated the moisture flux, which is the equivalent of the mechanical stress in Liu and Hong's paper. In addition to equating the expressions of flux in the peridynamic and classic model, I will also equate the expressions for flow power, which is similar to the deformation energy density in Silling et al. Moreover, the extension of the peridynamic flow model to multiple dimensions allows for the possibility of modeling soils where the hydraulic conductivity is anisotropic. I will also derive a relationship between κ and K with an additional dependence on the orientation of the peripipe relative the principal hydraulic conductivity axes.

Before I proceed, I must enhance the model by adding an extra feature to the description of nonlocality. So far, the only parameter influencing the degree of locality of the model is δ, the radius of the horizon. The smaller δ is, the more local the model is, and vise versa. In addition, all the points within a horizon have an equal influence on its center; the distance to the center being only an argument of the conductance of a peripipe and having no influence on the attenuation of the potential felt at the center. Similar to the peridynamic flow model in one

dimension, I would like to lift this limitation by making explicit the dependence between the influence of one point on another and the distance separating them.

3.5.1 Influence functions

Several influence function types have been used in peridynamic formulations to describe the dependence of the pairwise interaction on the separation distance. The simplest influence function is constant, or uniform; it shows no additional dependence on the separation distance (Silling, 2000, Silling et al., 2010, Simunek et al., 2005, Bobaru and Duangpanya, 2010, Bobaru and Hu, 2012). Others have used a normal distribution, arguing that in statistical mechanics, quantities — such as particle speeds, momenta, and energies — follow a Maxwell-Boltzmann distribution which at the continuum scale leads to a normal distribution (Kilic and Madenci, 2010). In evaluating the role the shape of the influence function plays on the behavior of a peridynamic model, Seleson and Parks used a family of spherical influence functions with a softening length of the form $f_p(r) = (r + \epsilon)^{-p}$ (Seleson and Parks, 2011).

I will use two types of influence functions in my derivations. The first is a uniform influence function; the second is a linear influence function similar to one of the functions used by Bobaru and Duangpanya. I introduce the influence function into the model by appending it to the peridynamic hydraulic conductivity function, so that $\kappa(\boldsymbol{x}\boldsymbol{x}')$ becomes: $\kappa(\boldsymbol{x}\boldsymbol{x}', \|\boldsymbol{x}\boldsymbol{x}'\|)$.

For the case of a uniform influence function (Figure 3.3a), there is no dependence of the peridynamic hydraulic conductivity on the distance between points. In this case I revert to the previous κ:

$$\kappa(\boldsymbol{x}\boldsymbol{x}', \|\boldsymbol{x}\boldsymbol{x}'\|) = \kappa(\boldsymbol{x}\boldsymbol{x}'). \tag{3.30}$$

For the case of a linear influence function (Figure 3.3b), the peridynamic hydraulic conductivity κ has a maximum at the center of the horizon and it

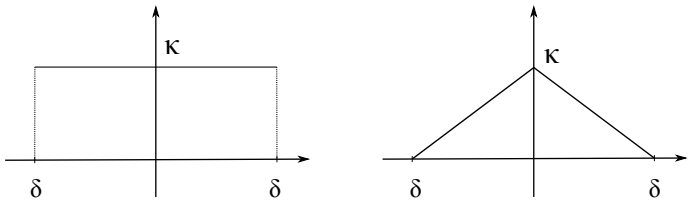

Fig. 3.3. Uniform and triangular influence functions.

decreases linearly as the length of the peripipe increases. If I set the influence to be zero at the edge of the horizon I get:

$$\kappa(\boldsymbol{x}\boldsymbol{x'}, \|\boldsymbol{x}\boldsymbol{x'}\|) = \kappa(\boldsymbol{x}\boldsymbol{x'}) \left(1 - \frac{\|\boldsymbol{x}\boldsymbol{x'}\|}{\delta}\right). \tag{3.31}$$

3.5.2 Isotropic conductivity function

In this section, I will derive the peridynamic hydraulic conductivity function for the simple case of isotropic soils. To that end, let me suppose I have a saturated two-dimensional infinite homogeneous column of soil . Suppose also that the flow is in steady state and the column is subjected to a linear hydraulic potential field with slope a (Equation 3.32). I will first derive the relationship between κ and K using the moisture flux equations and then derive it using the equations for flow power.

$$H(\boldsymbol{x}) = a\boldsymbol{x}.\hat{j} + c. \tag{3.32}$$

3.5.2.1. Derivation using moisture flux

In the first method, I equate the moisture flux at a point $\boldsymbol{x}$ in the direction of the maximum gradient of the applied hydraulic head, $(\hat{j})$, as given by the peridynamic formulation, with the same quantity given by the classic formulation.

According to the classic formulation, the flux at $\boldsymbol{x}$ in the direction of $\hat{j}$ is given by Darcy's Law:

$$\begin{aligned}\boldsymbol{q}(\boldsymbol{x}) &= -K(\boldsymbol{x})\nabla.H(\boldsymbol{x}),\\ &= -aK(\boldsymbol{x}).\end{aligned} \tag{3.33}$$

Where K is the classic hydraulic conductivity and $\nabla.H(\boldsymbol{x})$ was replaced by its value a.

According to the peridynamic formulation, the flux across the surface is given by Equation 3.26 repeated below.

$$\boldsymbol{q}_{\perp\mathcal{S}(\phi=0)}(O) = -\int_{\delta}^{0}\int_{\pi}^{2\pi}\int_{r_x}^{\delta}\kappa(\boldsymbol{x}\boldsymbol{x'})\Delta H(\boldsymbol{x}\boldsymbol{x'})sin(\phi_{x'}-\pi)\,\mathrm{d}r\mathrm{d}\phi_{x'}\mathrm{d}r_x.$$

Using Equation 3.32 and setting $r = \|\boldsymbol{x}\boldsymbol{x'}\|$, I can also replace the difference in hydraulic potential by the following:

$$\Delta H(\boldsymbol{x}\boldsymbol{x'}) = arsin(\phi_{x'}-\pi). \tag{3.34}$$

Combining Equations 3.34 and 3.26 I get:

$$\boldsymbol{q}_{\perp\mathcal{S}(\phi=0)}(O) = -\int_{\delta}^{0}\int_{\pi}^{2\pi}\int_{r_x}^{\delta}\kappa(\boldsymbol{x}\boldsymbol{x'})arsin^2(\phi_{x'}-\pi)\,\mathrm{d}r\mathrm{d}\phi_{x'}\mathrm{d}r_x. \tag{3.35}$$

In order to proceed, I have to decide on the type of the influence function: uniform, or linear. For a uniform influence function, no additional modifications to Equation 3.35 are needed.

Evaluating the right hand side of Equation 3.35 yields:

$$\boldsymbol{q}_{\perp\mathcal{S}(\phi=0)}(O) = -\frac{a\,\pi\delta^3}{6}\kappa. \tag{3.36}$$

Equating Equations 3.36 and 3.33 and solving for κ leads to:

$$\kappa = \frac{6}{\pi\delta^3}K. \tag{3.37}$$

And the equation for the peridynamic hydraulic conductivity for a homogeneous and isotropic soil in terms of the classic hydraulic conductivity using a uniform influence function is given by:

$$\kappa(\boldsymbol{x}\boldsymbol{x'}) = \frac{6}{\pi\delta^3}K. \tag{3.38}$$

For a linear influence function, I replace $\kappa(\boldsymbol{x}\boldsymbol{x'})$ by Equation 3.31, and Equation 3.35 becomes:

$$\boldsymbol{q}_{\perp\mathcal{S}(\phi=0)}(O) = -\int_{\delta}^{0}\int_{\pi}^{2\pi}\int_{r_x}^{\delta}\kappa\left(1-\frac{r}{\delta}\right)arsin^2(\phi_{x'}-\pi)\,\mathrm{d}r\mathrm{d}\phi_{x'}\mathrm{d}r_x. \tag{3.39}$$

Evaluating the right hand side of Equation 3.39 yields:

$$\boldsymbol{q}_{\perp\mathcal{S}(\phi=0)}(O) = -\frac{a\,\pi\delta^3}{24}\kappa. \tag{3.40}$$

Equating Equations 3.36 and 3.33 and solving for κ leads to:

$$\kappa = \frac{24}{\pi\delta^3}K. \tag{3.41}$$

And the equation for the peridynamic hydraulic conductivity for a homogeneous, and isotropic soil in terms of the classic hydraulic conductivity, using a linear influence function is given by:

$$\kappa(\boldsymbol{x}\boldsymbol{x'}, \|\boldsymbol{x}\boldsymbol{x'}\|) = \frac{24K}{\pi\delta^3}\left(1-\frac{\|xx'\|}{\delta}\right). \tag{3.42}$$

3.5.2.2. Derivation using flow power

In the classical local continuum framework, the power dissipated by moisture flow through an infinitesimal element at point $\boldsymbol{x}$ is given by:

$$\begin{aligned}\boldsymbol{p}(\boldsymbol{x}) &= K(\boldsymbol{x})\nabla.H(\boldsymbol{x})\Delta H(\boldsymbol{x}),\\ &= a^2K(\boldsymbol{x}).\end{aligned} \tag{3.43}$$

Where K is the classic hydraulic conductivity, and a replace $\nabla.H(\boldsymbol{x})$. And, because I am computing the power over an infinitesimal element I also have $\Delta H(\boldsymbol{x}) = a$.

The expression for power in the peridynamic framework which was given by Equation 3.29 is repeated below:

$$P(\boldsymbol{x},t) = \frac{1}{2}\int_0^{\delta}\int_0^{2\pi}\kappa(\boldsymbol{x}\boldsymbol{x'},t)(H(\boldsymbol{x'},t)-H(\boldsymbol{x},t))^2\,\mathrm{d}r\mathrm{d}\phi.$$

Replacing the difference in hydraulic potential by Equation 3.34 as I did in the previous section, I get:

$$P(\boldsymbol{x},t) = \frac{1}{2}\int_0^{\delta}\int_0^{2\pi} \kappa(\boldsymbol{x}\boldsymbol{x'},t)a^2r^2sin(\phi-\pi)^2\,\mathrm{d}r\mathrm{d}\phi. \tag{3.44}$$

For the case of a uniform influence function, evaluating the integral in Equation 3.45 I get:

$$P(\boldsymbol{x},t) = \frac{a^2\pi\delta^3}{6}\kappa. \tag{3.45}$$

Equating Equations 3.45 and 3.43 of the power in the peridynamic and classic frameworks respectively, and solving for κ leads to the following relationship:

$$\kappa = \frac{6}{\pi\delta^3}K. \tag{3.46}$$

Which is the same result given by the flux method in Equation 3.37.

For the case of a linear influence function, I replace $\kappa(\boldsymbol{x}\boldsymbol{x'})$ by Equation 3.31, and Equation 3.29 becomes:

$$P(\boldsymbol{x},t) = \frac{1}{2}\int_0^{\delta}\int_0^{2\pi} \kappa\left(1-\frac{r}{\delta}\right)a^2r^2sin(\phi-\pi)^2\,\mathrm{d}r\mathrm{d}\phi. \tag{3.47}$$

Evaluating the integral in Equation 3.47 I get:

$$P(\boldsymbol{x},t) = \frac{a^2\pi\delta^3}{24}\kappa. \tag{3.48}$$

Equating Equations 3.48 and 3.43 of the power in the peridynamic and classic frameworks respectively, and solving for κ leads to the following relationship for a linear influence function:

$$\kappa = \frac{24}{\pi\delta^3}K. \tag{3.49}$$

This is also identical to the result given by the flux method given in Equation 3.41

3.5.3 Anisotropic conductivity function

I will now derive the equation for the peridynamic hydraulic conductivity for the case of an anisotropic soil, where the hydraulic conductivity depends on the orientation of the peripipe. I will derive the equations for the two cases of a uniform influence function and a linear influence function. However, since I have shown that I arrive at the same equation whether I use the expressions for moisture flux or for flow power, for the following derivation I will only use the flow power method.

The peridynamic hydraulic conductivity κ now explicitly depends on the orientation angle of the peripipe, $\kappa(\boldsymbol{xx'}, \phi(\boldsymbol{xx'}))$, for the case of a uniform influence function, or on the orientation angle and the length of the peripipe, $\kappa(\boldsymbol{xx'}, \|\boldsymbol{xx'}\|, \phi(\boldsymbol{xx'}))$, for the case of a linear influence function.

Let the soil in a vertical columnbe anisotropic with $K_y = K$ and $K_x = nK$. In the classical framework, the power dissipated at $\boldsymbol{x}$ due to an applied uniform hydraulic gradient a in the direction of $\hat{j}$ is given by:

$$\begin{aligned} p(\boldsymbol{x}) &= a^2 K_y, \\ &= a^2 K. \end{aligned} \tag{3.50}$$

And the power dissipated at $\boldsymbol{x}$ due to an applied uniform hydraulic gradient a in the direction of $\hat{i}$ is given by:

$$\begin{aligned} p(\boldsymbol{x}) &= a^2 K_x, \\ &= a^2 nK. \end{aligned} \tag{3.51}$$

I need to derive an equation for κ that would yield a flow power equal to the classic formulation for both scenarios. In the classic framework, the directional hydraulic conductivity, $K(\phi)$, for an anisotropic medium is given by:

$$K(\phi) = \left(\frac{cos^2(\phi)}{nK} + \frac{sin^2(\phi)}{K} \right)^{-1}. \tag{3.52}$$

If I use the same relationship to express κ as a function of ϕ, I get different results when deriving the relationship between κ and the classic K by applying a uniform hydraulic potential gradient in the direction of $\hat{j}$ versus applying the gradient in the direction of $\hat{i}$. However, I will show by verification, that the following relationship gives equal results.

$$\kappa(\phi) = \left(\frac{\kappa_y cos^2(\phi)}{\kappa_x^2} + \frac{sin^2(\phi)}{\kappa_y} \right)^{-1}. \tag{3.53}$$

For the case of a uniform influence function, if the uniform hydraulic gradient a applied in the direction of $\hat{j}$, replacing κ in Equation 3.44 by Equation 3.53 after dropping the argument $\boldsymbol{xx'}$ for readability, I get:

$$P(\boldsymbol{x}, t) = \frac{1}{2} \int_0^{\delta} \int_0^{2\pi} \left(\frac{\kappa_y cos^2(\phi)}{\kappa_x^2} + \frac{sin^2(\phi)}{\kappa_y} \right)^{-1} a^2 r^2 sin(\phi - \pi)^2 \, \mathrm{d}r\mathrm{d}\phi. \tag{3.54}$$

If the hydraulic gradient a is applied in the direction of $\hat{i}$, I replace $sin(\phi - \pi)^2$ by $cos(\phi - \pi)^2$ in Equation 3.54, I get:

$$P(\boldsymbol{x}, t) = \frac{1}{2} \int_0^{\delta} \int_0^{2\pi} \left(\frac{\kappa_y cos^2(\phi)}{\kappa_x^2} + \frac{sin^2(\phi)}{\kappa_y} \right)^{-1} a^2 r^2 cos(\phi - \pi)^2 \, \mathrm{d}r\mathrm{d}\phi. \tag{3.55}$$

Evaluating the integrals in Equations 3.54 and 3.55 after I replace κ_y by κ and κ_x by $n\kappa$, leads to:

$$P_{\hat{j}}(\boldsymbol{x}, t) = \frac{n\pi a^2 \delta^3}{3(n+1)} \kappa. \tag{3.56}$$

$$P_{\hat{i}}(\boldsymbol{x}, t) = \frac{n^2 \pi a^2 \delta^3}{3(n+1)} \kappa. \tag{3.57}$$

Equating Equations 3.56 and 3.50, and solving for κ leads to:

$$\kappa = \frac{3(n+1)}{n\pi\delta^3} K. \tag{3.58}$$

Equating Equations 3.57 and 3.51, and solving for κ leads to the same result:

$$\kappa = \frac{3(n+1)}{n\pi\delta^3} K. \tag{3.59}$$

And the equation for the peridynamic hydraulic conductivity for an anisotropic soil in terms of the classic hydraulic conductivity components $K_y = K$ and $K_x = nK$, using a uniform influence function is given by:

$$\kappa(\boldsymbol{xx'}, \phi(\boldsymbol{xx'})) = K\frac{3(n+1)}{n\pi\delta^3}\left(\frac{cos^2(\phi)}{n^2} + sin^2(\phi)\right)^{-1}. \tag{3.60}$$

If I use a linear influence function, I multiply the integrand in Equations 3.54 and 3.55 by the term $(1 - r/\delta)$. After replacing κ_y by κ and κ_x by $n\kappa$ and integrating I get the following equations for the flow power due to an applied hydraulic the gradient in the direction of $\hat{j}$ and $\hat{i}$ respectively:

$$P_{\hat{j}}(\boldsymbol{x}, t) = \frac{n\pi a^2\delta^3}{12(n+1)}\kappa. \tag{3.61}$$

$$P_{\hat{i}}(\boldsymbol{x}, t) = \frac{n^2\pi a^2\delta^3}{12(n+1)}\kappa. \tag{3.62}$$

Equating Equations 3.61 and 3.62 with Equations 3.50 and 3.51 respectively leads to the same relationship given by:

$$\kappa = \frac{12(n+1)}{n\pi\delta^3}K. \tag{3.63}$$

And the equation for the peridynamic hydraulic conductivity for a homogeneous and anisotropic soil in terms of the classic hydraulic conductivity components $K_y = K$ and $K_x = nK$, using a linear influence function is given by:

$$\kappa(\boldsymbol{xx'}, \|\boldsymbol{xx'}\|, \phi(\boldsymbol{xx'})) = K\frac{12(n+1)}{n\pi\delta^3}\left(1 - \frac{\|\boldsymbol{xx'}\|}{\delta}\right)\left(\frac{cos^2(\phi)}{n^2} + sin^2(\phi)\right)^{-1}. \tag{3.64}$$

3.5.4 Generalizing to unsaturated, inhomogeneous soils

Equations 3.38, 3.42, 3.60, and 3.60 were derived under the assumption that the medium is homogeneous and at saturation, hence that it has a constant hydraulic conductivity. However, naturally occurring soils are almost always

heterogeneous, and their hydraulic conductivity varies in space. In addition, even soils with fairly homogeneous parameters will exhibit spatial variability in their conductivity when in unsaturated regimes due to the dependence of the conductivity on the moisture content or matric potential.

In order to adapt the derivation to the general case of inhomogeneous soils in the unsaturated regime, I will modify the mechanics of pairwise interactions and make additional assumptions similar to what I did in the derivation of the peridynamic flow model in one dimension. I will first replace each peripipe by two parallel peripipes, each responsible for half the interaction of the original one, and each has the peridynamic hydraulic conductivity of one of the nodes. I will also assume that the relationship between the peridynamic and the classic hydraulic conductivity is independent of the distribution of the moisture content within the horizon. With these modifications, the peridynamic hydraulic conductivity is now given by:

$$\kappa(\boldsymbol{x}\boldsymbol{x'},.,.,t) = \frac{\kappa(\boldsymbol{x},.,.,t)}{2} + \frac{\kappa(\boldsymbol{x'},.,.,t)}{2}. \tag{3.65}$$

Where the second and third arguments of κ, left blank, could be the length of the peripipe, $\|\boldsymbol{x}\boldsymbol{x'}\|$, and/or the orientation angle of the pipe, $\phi(\boldsymbol{x}\boldsymbol{x'})$, if the influence function is linear, and/or the soil is anisotropic.

I will verify the acceptability of these assumptions later in the chapter, by comparing results of flow simulations from the peridynamic model to results from a classic model. Assuming they are acceptable, the general form of the peridynamic equations for rate of change in moisture content, moisture flux, and flow power at a point $\boldsymbol{x}(x,y)$ are given by:

$$\frac{\partial\theta(x,y,t)}{\partial t} = \int_0^{2\pi}\int_0^{\delta} \kappa(\boldsymbol{x}\boldsymbol{x'}, \|xx'\|, \phi_{x'}, t)\frac{H(x',y',t) - H(x,y,t)}{r_{x'}} \underbrace{r_{x'}\mathrm{d}r_{x'}\mathrm{d}\phi_{x'}}_{\mathrm{d}V_{x'}}. \tag{3.66}$$

$$q_{\perp\phi}(x,y,t) = -\int_{\delta}^{0}\int_{\pi}^{2\pi}\int_{r_{x'}}^{\delta}\kappa(\boldsymbol{x'x''},\|x'x''\|,\phi_{x'},t)sin(\phi_{x'}-\phi-\pi)$$
$$\frac{H(x'',y'',t)-H(x',y',t)}{r_{x''}}\underbrace{r_{x''}\mathrm{d}r_{x''}\mathrm{d}\phi_{x'}}_{\mathrm{d}V_{x'}}\mathrm{d}r_{x'}. \tag{3.67}$$

$$P(x,y,t) = \frac{1}{2}\int_{0}^{2\pi}\int_{0}^{\delta}\kappa(\boldsymbol{xx'},\|xx'\|,\phi_{x'},t)\frac{(H(x',y',t)-H(x,y,t))^2}{r_{x'}}\underbrace{r_{x'}\mathrm{d}r_{x'}\mathrm{d}\phi_{x'}}_{\mathrm{d}V_{x'}}. \tag{3.68}$$

With the following:

$$x' = x + r_{x'}cos(\phi_{x'}), \qquad y' = y + r_{x'}sin(\phi_{x'}), \tag{3.69}$$

$$x'' = x' + r_{x''}cos(\phi_{x'}-\pi), \qquad y'' = y' + r_{x''}sin(\phi_{x'}-\pi). \tag{3.70}$$

$$\kappa(\boldsymbol{xx'},\|xx'\|,\phi,t) = \frac{K(x,y,t)+K(x',y',t)}{2}\frac{3(n+1)}{n\pi\delta^3}\left(\frac{cos^2(\phi)}{n^2}+sin^2(\phi)\right)^{-1}\times$$
$$\begin{cases} 1, & \text{Uniform influence function} \\ 4\left(1-\dfrac{r_{x'}}{\delta}\right), & \text{Linear influence function} \end{cases} \tag{3.71}$$

Where δ is the radius of the peridynamic horizon, and the classic hydraulic conductivity of the soil is $K_y(x,y,t) = K(x,y,t)$ and $K_x(x,y,t) = nK(x,y,t)$.

3.6 Numerical implementation in 2D and comparison with a classic model

Numerical implementation of the peridynamic model was carried out by discretizing the medium into nodes using a regular grid. Figure 3.4 shows a section of a discretized two-dimensional domain with a grid spacing of Δx and a horizon radius $\delta = m\Delta x$ with $m = 4$, and where m is the horizon radius in multiples of grid lengths. Each node in the grid represents a volume of Δx^2, and has a

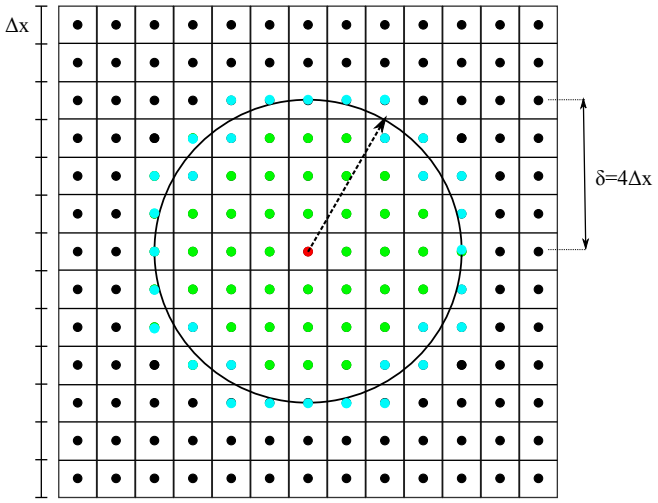

Fig. 3.4. Discrete representation of a peridynamic horizon of radius $4\Delta x$. Point in red is the center of the horizon. Points in green are fully included in the horizon. Points in cyan are partially covered in the horizon.

moisture content θ_{ij}, an associated hydraulic potential H_{ij} and a classic hydraulic conductivity K_{ij}.

The choice of a regular grid is motivated by its convenience, and to simplify parallelization. The derivation of the peridynamic model places no restriction on the type of spatial discretization used. In fact, when modeling complex geometries, irregular grids may even be more useful (Simunek et al., 2005).

I only implemented the equation of the rate of change in moisture content in my peridynamic flow model code. In the following, I outline the discretizating and parallelization of this equation.

I will start by rewriting Equation 3.66 in a more concise manner:

$$\frac{\partial \theta_x}{\partial t} = \int_{\mathcal{H}_x} (K_x + K_{x'}) (H_{x'} - H_x) A_{xx'} \, \mathrm{d}x'. \tag{3.72}$$

Where $A_{xx'}$ is given by:

$$A_{xx'} = \frac{3\,(n+1)\,V_{x'}}{2n\pi\delta^2 r_{xx'}} \left(\frac{cos^2(\phi_{xx'})}{n^2} + sin^2(\phi_{xx'}) \right)^{-1} \times \begin{cases} 1, & \text{Uniform influence function} \\ 4\left(1 - \dfrac{r_{xx'}}{\delta}\right) & \text{Linear influence function} \end{cases} \tag{3.73}$$

Expanding the integrand in Equation 3.72, I get:

$$\frac{\partial \theta_x}{\partial t} = \int_{\mathcal{H}_x} K_x H_{x'} A_{xx'}\,\mathrm{d}x' - \int_{\mathcal{H}_x} K_x H_x A_{xx'}\,\mathrm{d}x' + \int_{\mathcal{H}_x} K_{x'} H_{x'} A_{xx'}\,\mathrm{d}x' - \int_{\mathcal{H}_x} K_{x'} H_x A_{xx'}\,\mathrm{d}x'. \tag{3.74}$$

Which is the following sum of two-dimensional convolutions with a circular kernel A with radius δ:

$$\frac{\partial \theta_x}{\partial t} = K_x(H * A) - K_x H_x(1 * A) + (KH) * A - H_x(K * A). \tag{3.75}$$

Because I am using a regular grid, and noting that $A_{xx'}$ depends only on $r_{xx'}$ and $\phi_{xx'}$ and, therefore, could be represented by a matrix $A(2m+1,\, 2m+1)$, Equation 3.75 is written in the following discrete form:

$$\frac{\partial \theta_{ij}}{\partial t} = K_{ij} \sum_{k=-m}^{m} \sum_{p=-m}^{m} H_{ab} A_{kp} \quad - K_{ij} H_{ij} \sum_{k=-m}^{m} \sum_{p=-m}^{m} A_{kp} + \sum_{k=-m}^{m} \sum_{p=-m}^{m} K_{ab} H_{ab} A_{kp} \quad - H_{ij} \sum_{k=-m}^{m} \sum_{p=-m}^{m} K_{ab} A_{kp}. \tag{3.76}$$

With $a = i + k$ and $b = j + p$.

Taking advantage of modern multi-core processors, at every time step of the simulation, each convolution in Equation 3.76 is submitted and evaluated on one processor core. In addition, following the evaluation of the convolutions, the domain is split between all available cores where moisture content, matric potential, and hydraulic conductivity at each point are updated before the next time step.

The simulation is explicitly integrated in time using the Euler method with a small time step. The model was implemented using C++ and OpenMP library; its algorithm is presented in Figure 3.5.

```
1  Generate matric head vs moisture content look-up table per soil type;
2  Generate hydraulic conductivity vs moisture content look-up table per soil
   type;
3  Calculate 2D matrix size to store node specific data;
4  Generate 2D moisture content matrix and initialize to initial conditions;
5  Generate 2D matric head matrix and initialize to initial conditions;
6  Generate 2D total hydraulic head matrix H, and initialize using matric head
   and position;
7  Generate 2D hydraulic conductivity matrix K, and initialize to initial
   conditions;
8  Generate 2D convolution kernel A and initialize (Equation 3.73);
9  Assemble convolution input matrices: H, K. * H, and K (Equation 3.75);
10 for t = 1 to Number of time steps do
11 |   Core1: perform convolution H * A;
12 |   Core2: perform convolution 1 * A;
13 |   Core3: perform convolution KH * A;
14 |   Core4: perform convolution K * A;
15 |   for n = 1 to Number of nodes do in parallel
16 |   |   Update moisture content of each node (Equation 3.75;
17 |   |   if node n belongs to a boundary then
18 |   |   |   Update moisture content of node n according to boundary
   |   |   |   condition;
19 |   |   end
20 |   |   Update H and K;
21 |   |   Recalculate convolution input matrices;
22 |   end
23 |   Write results of timestep t to file;
24 end
```

Fig. 3.5. Implementation algorithm of peridynamic moisture flow model in 2D

In order to validate the proposed model, check the adequacy of the anisotropic hydraulic conductivity formulation, and evaluate the impact of the type of influence function (uniform or linear) on the performance of the model, several scenarios are simulated. Due to the lack of an analytical solution of the flow problem, the

same scenarios are also simulated using HYDRUS 2D/3D (Simunek et al., 2006), a 2D/3D finite element model that solves the classic Richard's equation. The results from HYDRUS 2D/3D serve as a benchmark for evaluating the performance of my peridynamic flow model.

The validation scenarios are divided into two groups. The first group is scenarios of moisture redistribution within a horizontal soil layer having an area with a higher moisture content than the rest of the layer. The second group is scenarios of drainage from a vertical soil column with a moisture content initially at saturation. The soil in the first group has homogeneous properties, whereas the soil in the second group is composed of two soil types.

In each group, the simulations were performed assuming isotropy, and then repeated assuming anisotropy of the hydraulic conductivity. In addition, every simulation was performed twice, using a uniform influence function in one, and a linear influence function in the other. All the peridynamic simulations were performed using a horizon radius $\delta = 1cm$ and a point density value $m = 4$ yielding a grid size $\Delta x = 0.25cm$. The choice δ and m was made by taking into consideration the results of the convergence analysis performed in developing the peridynamic flow model in one dimension, and the computational resources required for running the simulations.

For the soil characteristic curves that describe the relationships between the soil's moisture content, the soil matric head, and the unsaturated hydraulic conductivity, I used the Van Genuchten model (Van Genuchten, 1980). The model is given by the following equations:

$$\theta(h_m) = \theta_r + \frac{\theta_s - \theta_r}{[1 + (\alpha|h_m|)^n]^{1-1/n}}. \tag{3.77}$$

$$K(\theta) = K_s \left(\frac{\theta - \theta_r}{\theta_s - \theta_r}\right)^{\frac{1}{2}} \left\{1 - \left[1 - \left(\frac{\theta - \theta_r}{\theta_s - \theta_r}\right)^{\frac{n}{n-1}}\right]^{\frac{n-1}{n}}\right\}^2. \tag{3.78}$$

Where θ_s and θ_r are the volumetric water content at saturation and residual respectively. K_s is the soil hydraulic conductivity at saturation, α is related to

the inverse of the air entry pressure, and n is a parameter related to the soil pore size distribution. Rearranging Equation 3.77, I get the expression of the matric potential as a function of the moisture content:

$$h_m(\theta) = -\frac{1}{\alpha}\left[\left(\frac{\theta_s - \theta_r}{\theta - \theta_r}\right)^{\frac{n}{n-1}} - 1\right]^{\frac{1}{n}}. \tag{3.79}$$

The properties of the various soils used in the simulations such as residual moisture content, moisture content at saturation, and the saturated hydraulic conductivities, along with the Van Genuchten model parameters for these soils, are listed in Table 3.1.

Table 3.1
Van Genuchten soil parameters.

$SoilID$	θ_s	θ_r	Ks_1	Ks_2	α	n
S1	0.430	0.078	24.96	24.96	0.036	1.56
S2	0.430	0.078	24.96	24.96	0.036	1.56
S3	0.430	0.078	24.96	24.96	0.036	1.56
S4	0.430	0.078	24.96	24.96	0.036	1.56

3.6.1 Moisture redistribution scenarios

These examples simulate the redistribution of moisture within a two-dimensional horizontal layer of soil. The soil layer is 100 cm long by 100 cm wide. The soil layer is divided into two zones. Zone One is a 30 cm long by 30 cm wide in the middle of the soil layer with the lower left corner located at coordinates $(35, 35)$ and the upper right corner located at coordinates $(65, 65)$. Zone Two is the soil layer excluding Zone One. Soil properties in both zones are identical. Initially, the soil in Zone One is at saturation moisture content 0.43%, and the soil in Zone Two is at 0.25%. The boundary conditions at the edges of the soil layer are no flow boundary conditions. I simulated two variants of this example. In the first variant,

I used soil S1 that has an isotropic hydraulic conductivity; in the second, I used soil S2 that has an anisotropic hydraulic conductivity, with the major conductivity directions parallel to the model axis.

In HYDRUS 2D/3D, the layer is simulated using the Van Genuchten soil model, with all boundary conditions set to zero flux. Initially, nodes in Zone One are set to saturation moisture content, and all the other nodes are set to a moisture content of 0.25%. Grid length is set to $0.5cm$ in order to remain within the maximum number of nodes of the program. Conversion criteria were set to 1E-5 for absolute change in moisture content and to $0.01cm$ for absolute change in matric potential.

For the peridynamic model, zero flux boundary conditions were simulated by using periodic boundary conditions. Because of the symmetry of the problem, periodic and no flow boundary conditions are equivalent. The moisture content for soil volumes in Zone One were initially set to saturation moisture content, and the remaining were set to a moisture content of 0.25%. The time step used for these scenarios is 1E-6 days.

3.6.1.1. Isotropic conductivity

Figure 3.6 is an image of the moisture content distribution of the isotropic redistribution scenario at 0.2 days simulated using HYDRUS 2D/3D. Figures 3.7 is the image of the moisture content distribution at 0.2 days from the peridynamic model simulations with a uniform influence function; Figure 3.8 represents moisture content distribution at the same point in time using the peridynamic model with a linear influence function. All three images have the same color map extents. Following a visual inspection of the images, I observe a very good agreement between the results of the classic model and the peridynamic model for both types of influence functions.

In order to obtain a more quantitative evaluation of the level of agreement between both models and investigate the impact of the type of the influence

function on the performance of the model, I will look at the relative difference of the moisture content between the results of the peridynamic model and the classic model (Equation 3.80). Figures 3.9 3.10 are the images of the relative difference at 0.2 days for the uniform and linear influence functions respectively.

$$rd(\boldsymbol{x}) = 100\frac{\theta_{peri}(\boldsymbol{x}) - \theta_{classic}(\boldsymbol{x})}{\theta_{classic}(\boldsymbol{x})}. \tag{3.80}$$

It is clear from these figures that for both influence function types, the relative difference between the peridynamic and the classic models is very small, and varies between around -0.1%, up to about 0.4% for the uniform influence function, and up to 0.3% for the linear influence function. I notice that at the center of Zone One, the peridynamic model slightly underestimates the moisture content. As I move away from the center, the relative difference changes very slowly until I get closer to the edges of Zone One, where it increases sharply and becomes positive, then sharply decreases back to a small negative value before it tapers off at zero.

The fact that these sharp changes in relative difference happen over a small distance makes them less problematic and reduces their bearing on the performance of the model. Nevertheless, they are better understood when I notice that they coincide at the front separating the saturated soil from the soil at a lower moisture content. In this region, the moisture gradient is very large, and even small variations in its location and shape from one model to another may lead to large variations in moisture content at points within the front.

These variations between the classic and the peridynamic models can be attributed to the nature of these models, specifically the local versus non-local aspects of the formulations. To illustrate, let me go through the process of moisture redistribution scenario. At the beginning of the simulation, the soil has a sharp drop in moisture at the interface between Zone One and Zone Two. As time goes by, moisture flows from Zones One into Zone Two, which leads to an increase of the moisture content in Zone Two and a decrease in Zone One near the interface. Consequently, the interface zone widens and the moisture gradient becomes smaller. In the classic local formulation, this exchange happens over an

infinitesimal distance; whereas, in the nonlocal peridynamic framework, moisture exchange happens over the entire radius of the horizon. This means that moisture is exchanged from one side of the front to the other, between points located further away from the front. This leads to more moisture moving from one side of the interface to the other side, which explains the observed relative differences.

Although this behavior is observed in both peridynamic simulations, some differences exist between the results obtained using a uniform influence function and those obtained using a linear influence function. The simulation using the uniform type underestimated the moisture content inside Zone One, and overestimated it near the front in Zone Two when compared to the results from the linear influence function. This can be better observed in Figure 3.11. I attribute these differences to the shape of the function.

These differences between the uniform and linear influence functions are attributed to the shape of the function. Despite the fact that I used the same horizon radius in both simulations, the uniform influence function treats all the points within a horizon equally, whereas a linear influence function favors more points that are near the center at the expense of points further away. This preference for points closer to the center makes the behavior of a peridynamic model with a linear influence function less nonlocal and closer to the classic local model.

3.6.1.2. Anisotropic conductivity

Figure 3.12 is an image of the moisture content distribution of the isotropic redistribution scenario at 0.2 days simulated using HYDRUS 2D/3D. Figures 3.13 is the image of the moisture content distribution at 0.2 days from the peridynamic model simulations with a uniform influence function; Figure 3.14 represents moisture content distribution at the same point in time using the peridynamic model with a linear influence function. All three images have the same color map

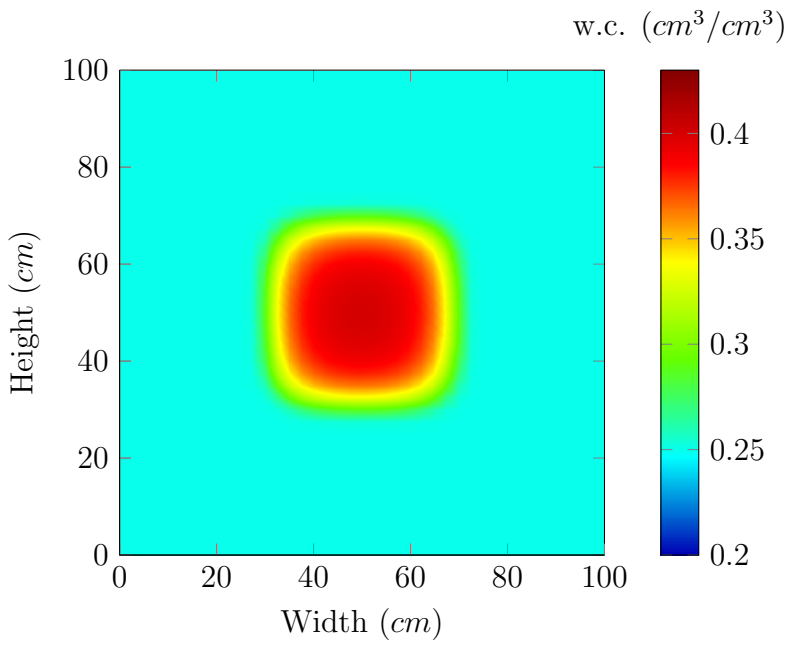

Fig. 3.6. Redistribution scenario, isotropic soil: Hydrus simulation results for moisture content at 0.2 days.

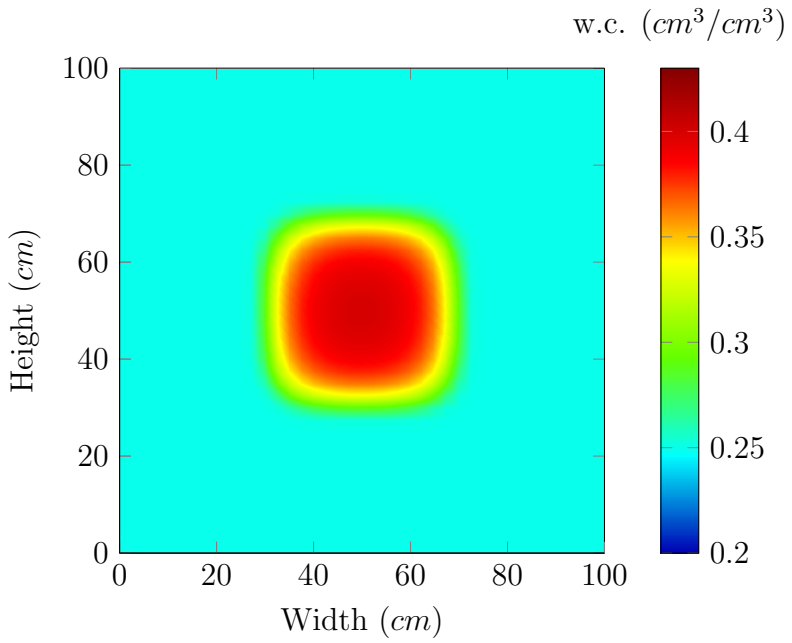

Fig. 3.7. Redistribution scenario, isotropic soil: Peridynamic simulation results for moisture content at 0.2 days. Uniform influence function, $\delta = 1cm$, and a point density value $m = 4$.

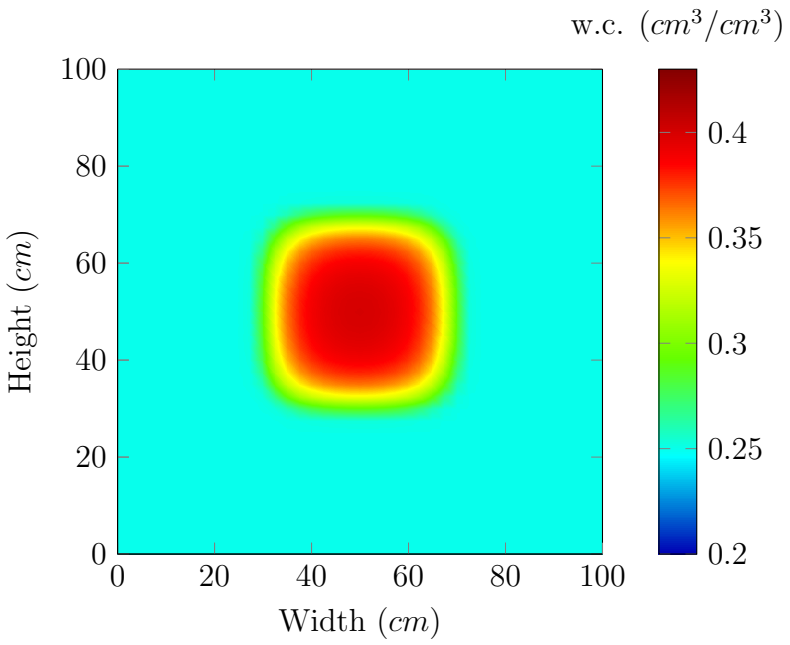

Fig. 3.8. Redistribution scenario, isotropic soil: Peridynamic simulation results for moisture content at 0.2 days. Linear influence function, $\delta = 1cm$, and a point density value $m = 4$.

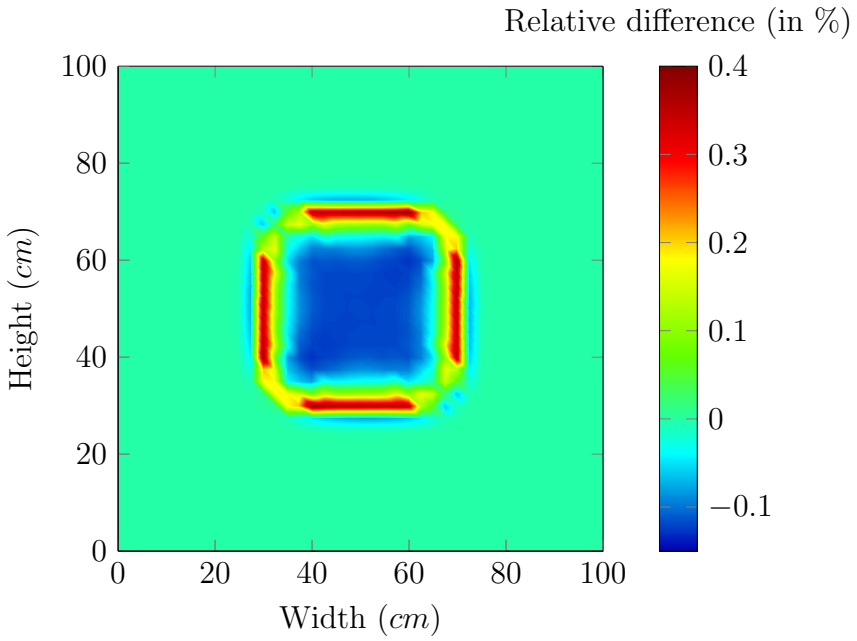

Fig. 3.9. Redistribution scenario, isotropic soil: Relative difference (in %) of moisture content between the peridynamic model results and the classic model HYDRUS at 0.2 days. Uniform influence function, $\delta = 1cm$, and a point density value $m = 4$.

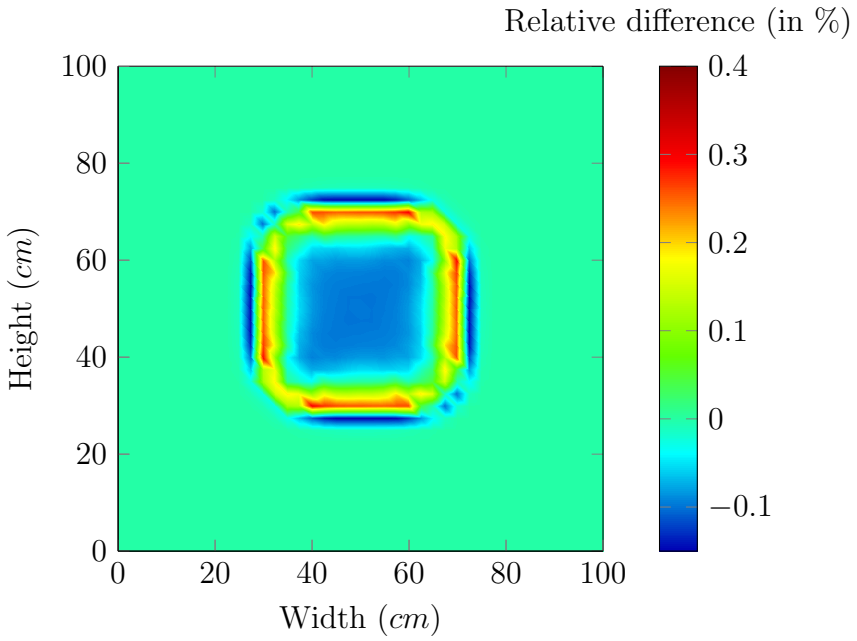

Fig. 3.10. Redistribution scenario, isotropic soil: Relative difference (in %) of moisture content between the peridynamic model results and the classic model HYDRUS at 0.2 days. Linear influence function, $\delta = 1cm$, and a point density value $m = 4$.

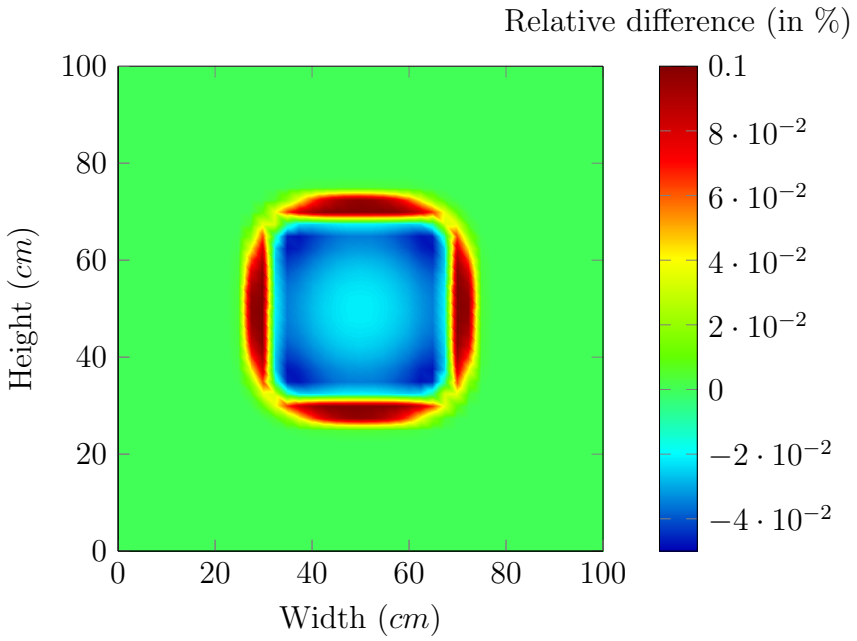

Fig. 3.11. Redistribution scenario, isotropic soil: Relative difference (in %) of moisture content between uniform and triangular influence functions for the peridynamic model at 0.2 days. Horizon radius $\delta = 1cm$, and a point density value $m = 4$.

extents. Just as in the earlier section, following a visual inspection of the images I observe a very good agreement between the results of the classic model and the peridynamic model for both types of influence functions.

Figures 3.16 and 3.16 are the images of the relative difference of the moisture content of the peridyamic model with respect to the classic model at 0.2 days for the uniform and linear influence functions respectively. I notice that the values of the relative difference are acceptable and range between -0.2% and 0.7%. Similarly to the results from the simulations of isotropic soils, I notice that at the center of Zone One, the model slightly underestimates the moisture content. As I move away from the center, the relative error changes very slowly until I get closer to the edges of Zone One, where the relative difference increases sharply before it reverses in direction and tapers off at zero.

However, when compared to the simulations of the isotropic soil, these results exhibit some very clear differences in the relative difference. The first is the difference in magnitude of the relative difference between the major flow axes, where it is higher in the direction of faster flow. The second is that the results of the simulation using a linear influence function show even higher relative difference along this direction, and a reduction in the relative difference in the direction of slower flow, compared to the results using the uniform influence function.

I attribute the model's deviation in behavior from the isotropic soil simulations to a combination of factors. The first factor is related to the Euler scheme I used to integrate the simulation forward in time. This naive numerical method requires a very small time step to give accurate results, which I used. However, no matter how small the error is, it remains proportional to the hydraulic conductivity, and it effectively translates into a proportional increase in the conductivity.

The second factor in the model's deviation is related to the medium's anisotropy. As a result of this anisotropy, the error in the direction of the fast flow will be larger than the error in the direction of the slow flow. This asymmetry in the error leads to an effective increase in the conductivity that is also asymmetric

and highest along the fast flow direction. Consequently, more moisture flows from Zone One towards the left and right fronts, leaving the center with a lower than expected moisture content, which in turn slows the flow in the other direction and prevents higher relative differences at the top and bottom front.

This behavior is even more pronounced when I use a linear influence function, which is peculiar since the more local behavior of the linear influence function suggests that the results should be closer to the classic model. However, Figure 3.9 shows a stronger asymmetry, with a higher increase in relative difference at the left and right fronts, and a higher decrease in relative difference at the top and bottom fronts. One potential explanation is that because of the more local behavior and the fact that a linear function favors more points closer to the center — note the factor four in Equation 3.71 — the linear influence function better captures the effects of the numerical errors; whereas, the uniform influence function smears this effect over the entire horizon by acting as a low pass filter.

Despite the minor differences between the results using the classic model and those obtained using the peridynamic model, the relative difference between these two formulations is negligible allowing me to move to the scenarios of moisture drainage in heterogeneous soils.

3.6.2 Drainage of heterogeneous soil examples

The following examples simulate the drainage of moisture from a two-dimensional vertical layer of soil. The soil layer is $100cm$ long by $100cm$ wide, and is divided into three vertical zones. Zone Two is $30cm$ long by $30cm$ wide in the middle of the soil layer with the lower left corner located at coordinates $(35, 0)$ and the upper right corner located at coordinates $(65, 100)$. Zone One and Zone Three are respectively at the left and right of Zone Two. Zone One and Zone Three have identical soils, whereas the soil in Zone Two has a faster hydraulic conductivity. Initially, the soil is at saturation moisture content (0.43%). The

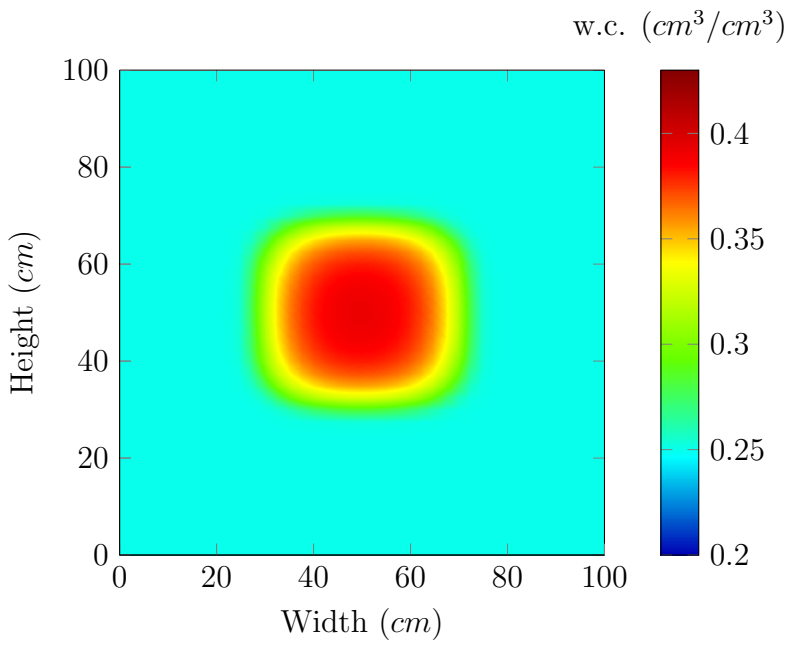

Fig. 3.12. Redistribution scenario, anisotropic soil: Hydrus simulation results for moisture content at 0.2 days.

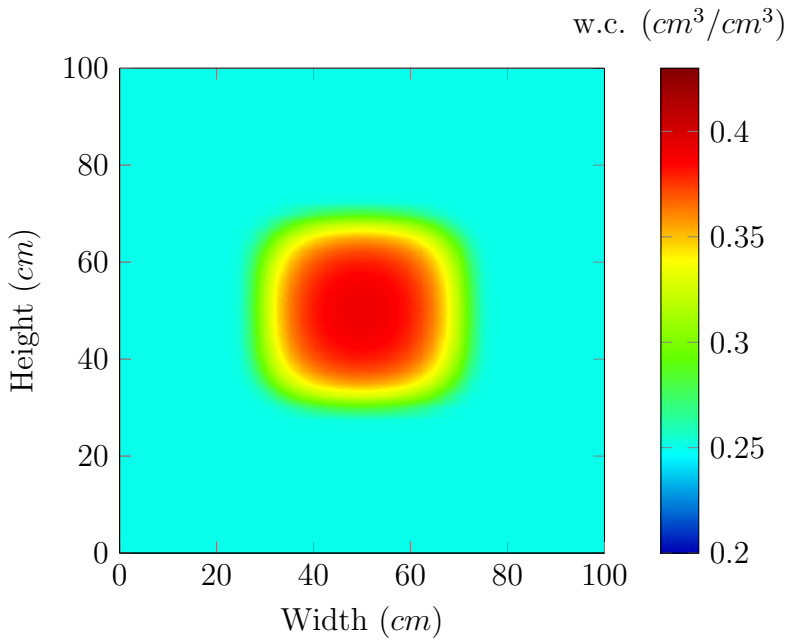

Fig. 3.13. Redistribution scenario, anisotropic soil: Peridynamic simulation results for moisture content at 0.2 days. Uniform influence function, $\delta = 1cm$, and a point density value $m = 4$.

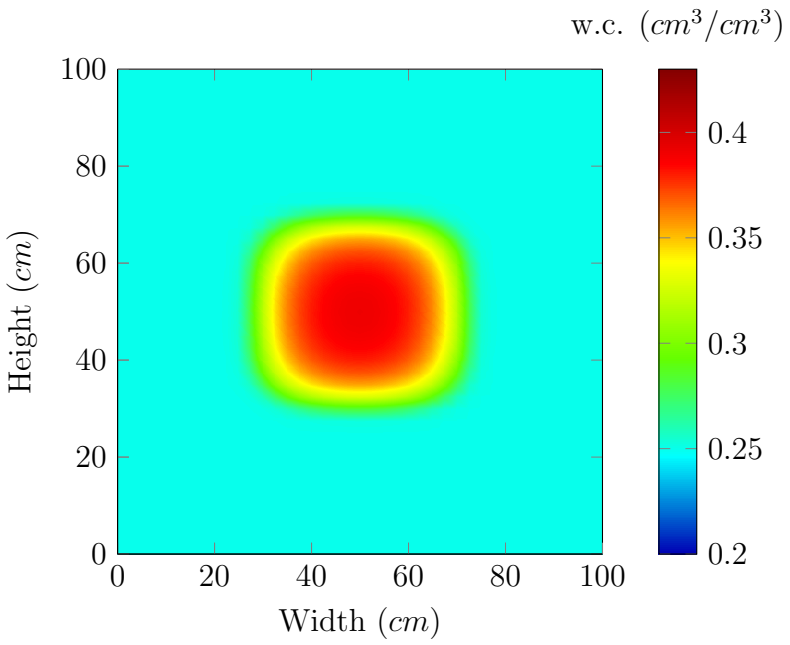

Fig. 3.14. Redistribution scenario, anisotropic soil: Peridynamic simulation results for moisture content at 0.2 days. Linear influence function, $\delta = 1cm$, and a point density value $m = 4$.

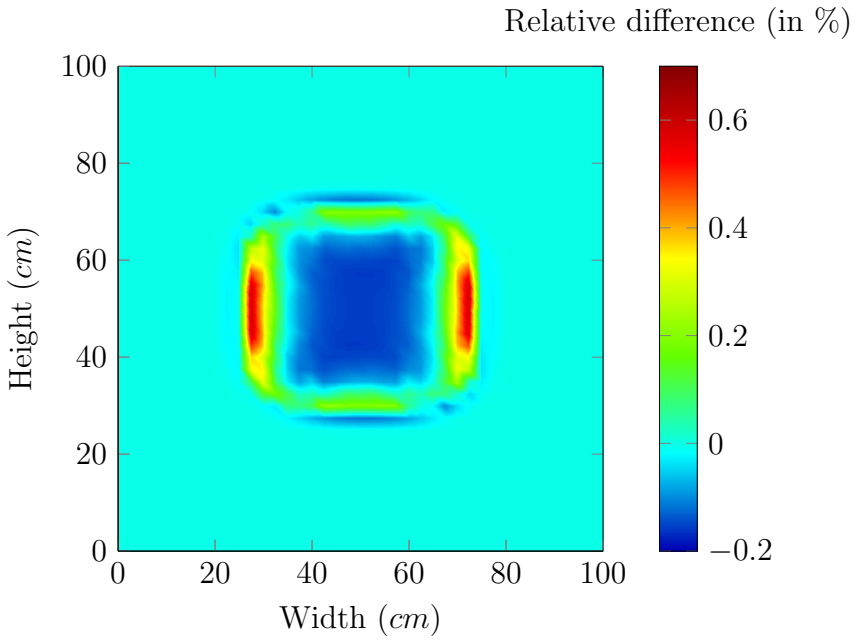

Fig. 3.15. Redistribution scenario, anisotropic soil: Relative difference (in %) of moisture content between the peridynamic model results and the classic model HYDRUS at 0.2 days. Uniform influence function, $\delta = 1cm$, and a point density value $m = 4$.

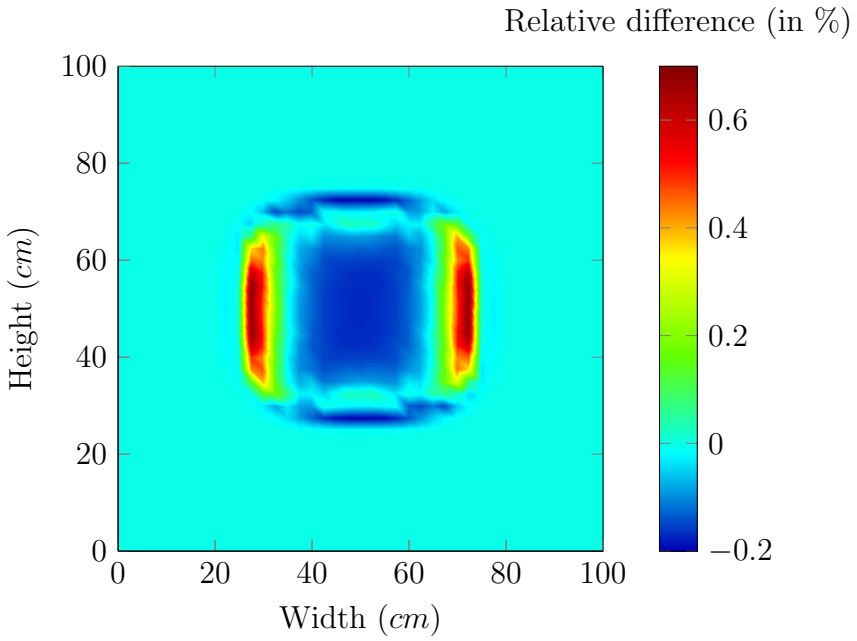

Fig. 3.16. Redistribution scenario, anisotropic soil: Relative difference (in %) of moisture content between the peridynamic model results and the classic model HYDRUS at 0.2 days. Linear influence function, $\delta = 1cm$, and a point density value $m = 4$.

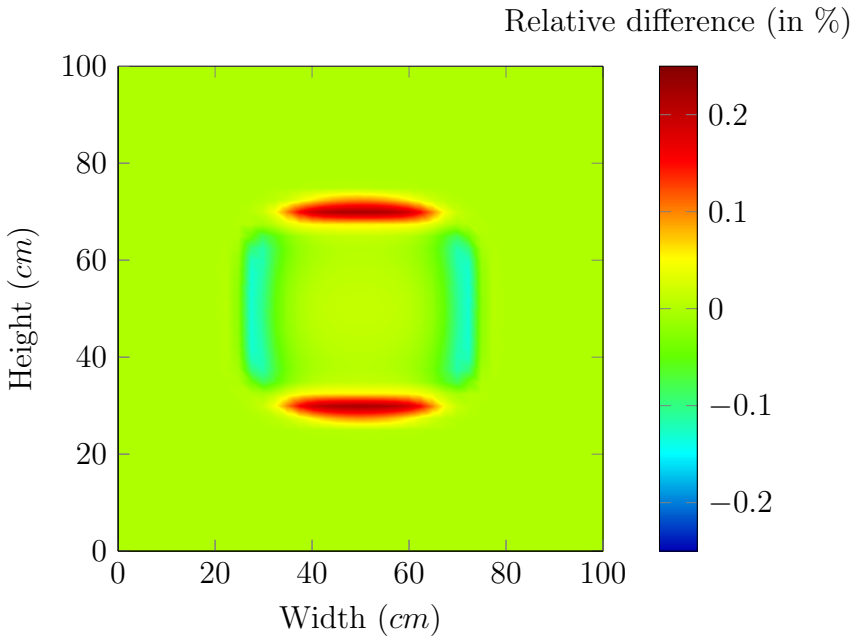

Fig. 3.17. Redistribution scenario, anisotropic soil: Relative difference (in %) of moisture content between uniform and triangular influence functions for the peridynamic model at 0.2 days. Horizon radius $\delta = 1cm$, and a point density value $m = 4$.

left, right, and top boundary conditions are no flow boundary conditions, and the bottom boundary is maintained at saturation. I simulated two variants of this example. In the first variant, I used soil S3, in Zone One and Zone Three, and soil S4 in Zone Two, all of which have an isotropic hydraulic conductivity. In the second variant I replaced soils S3 and S4 by soils S5 and S6 respectively. These soils have an anisotropic hydraulic conductivity, with the major conductivity directions parallel to the model axis.

In HYDRUS 2D/3D, the layer is simulated using the Van Genuchten soil model. The left, right, and top boundary conditions are set to zero flux, while the bottom boundary is maintained at saturation. Soil elements were assigned their respective type depending on their location. At time zero all nodes were set to saturation moisture content. Grid length is $0.5cm$ in order to remain within the maximum number of nodes of the program. Convergence criteria were set to 1E-5 for absolute change in moisture content and to $0.01cm$ for absolute change in matric potential.

For the peridynamic model, zero flux boundary conditions were assigned to the top, left and right boundaries. Because of the nonlocal nature of the formulation, the bottom boundary condition was simulated by adding an additional number of nodes from $x = 0cm$ to $x = -\delta$. The lower boundary nodes were maintained at saturation moisture content for the duration of the simulation. Moisture content was set initially to saturation everywhere, and the soil volumes were assigned their respective soil types. The time step used for these scenarios was 1E-5 hours.

3.6.2.1. Isotropic conductivity

Figure 3.18 is an image of the moisture content distribution of the isotropic redistribution scenario at 2 hours simulated using HYDRUS 2D/3D. Figures 3.19 and 3.20 are images of the moisture content distribution at 2 hours from simulations using the peridynamic model with a uniform and a triangular influence functions respectively. All three images have the same color map extents. Following

a visual inspection of the images, I observe a very good agreement between the results of the classic model and the peridynamic model for both types of influence functions.

As in my previous analysis, I will look at the relative difference of the moisture content between the results of the peridynamic model and the classic model to evaluate the level of agreement between both models and investigate the impact of the type of the influence function on the performance of the model. Figures 3.21 3.22 are the images of the relative difference at 2 hours for the uniform and linear influence functions respectively.

I note from these results that for both influence function types, the relative difference between the peridynamic and the classic models is small, and does not exceed -0.275%, with the results of the simulation using a linear influence function yielding smaller areas with large relative differences.

I also note an interesting feature near the top boundary where there is an improvement of the relative difference. This feature is attributed to a reduced conductivity compared to the rest of the domain which produces a lower moisture flow out of the soil near the boundary and leads to the high relative differences observed just below the boundary. This reduced conductivity is the result of the assumptions made when deriving the relationship between the peridynamic and the classic conductivity — specifically, the assumption that a point interacts with a full horizon, which is not the case for points located less than a horizon radius away from the boundary.

Figure 3.23 is an image of the relative difference between the results of the peridynamic model using a uniform influence function relative to a linear influence function. I note that the relative difference is in the order of $10^{-3}\%$, and that almost everywhere in the domain the uniform influence function leads to lower moisture content. This is expected, since a uniform influence function facilitates the transfer of larger amounts of moisture between points further away from the center of a horizon than a linear influence function will. The exception to this observation

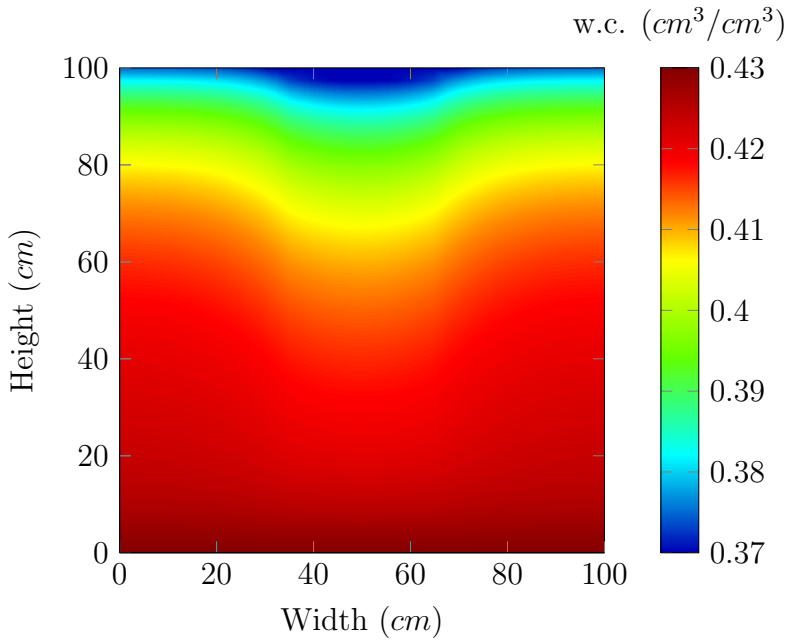

Fig. 3.18. Drainage scenario, isotropic soil: Hydrus simulation results for moisture content at 0.2 days.

are points near the top boundary. At these locations, the uniform influence function leads to higher moisture content than the linear influence function. This is also an artifact of the same derivation issue described in the previous paragraph. This effect is more pronounced when a uniform function is used instead of a linear one. This is due to that fact that, in the case of a linear function, as points get closer to the boundary, the first to be lost from the horizon are points of reduced influence. In contrast, in the case of a uniform function, where all points have equal weight, the effect on the conductivity of the horizon is more detrimental.

3.6.2.2. Anisotropic conductivity

Figure 3.24 is an image of the moisture content distribution of the anisotropic redistribution scenario at 2 hours simulated using HYDRUS 2D/3D. Figures 3.25 and 3.26 are images of the moisture content distribution at 2 hours from

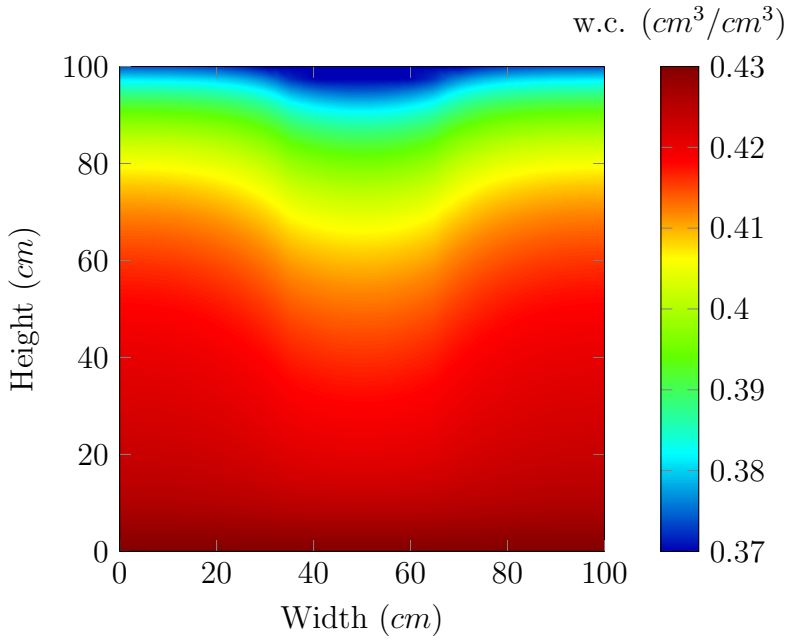

Fig. 3.19. Drainage scenario, isotropic soil: Peridynamic simulation results for moisture content at 0.2 days. Uniform influence function, $\delta = 1cm$, and a point density value $m = 4$.

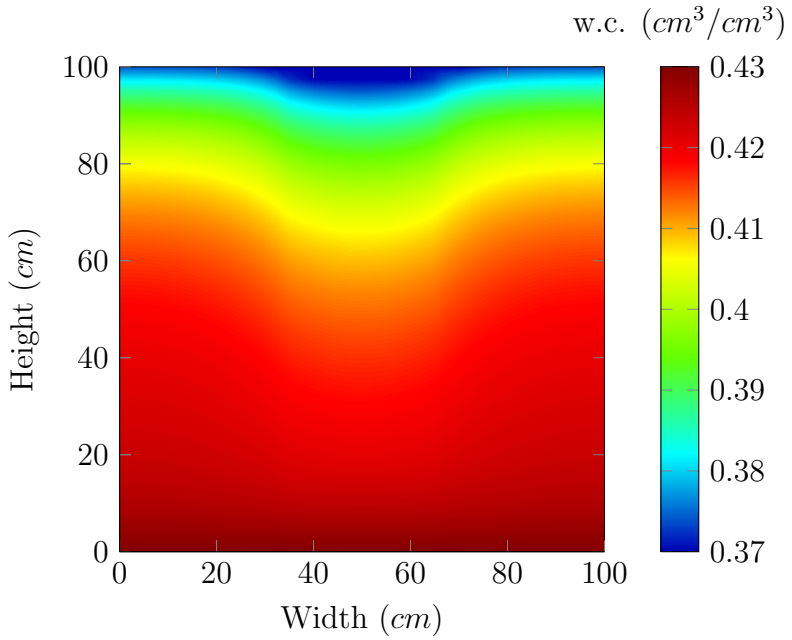

Fig. 3.20. Drainage scenario, isotropic soil: Peridynamic simulation results for moisture content at 0.2 days. Linear influence function, $\delta = 1cm$, and a point density value $m = 4$.

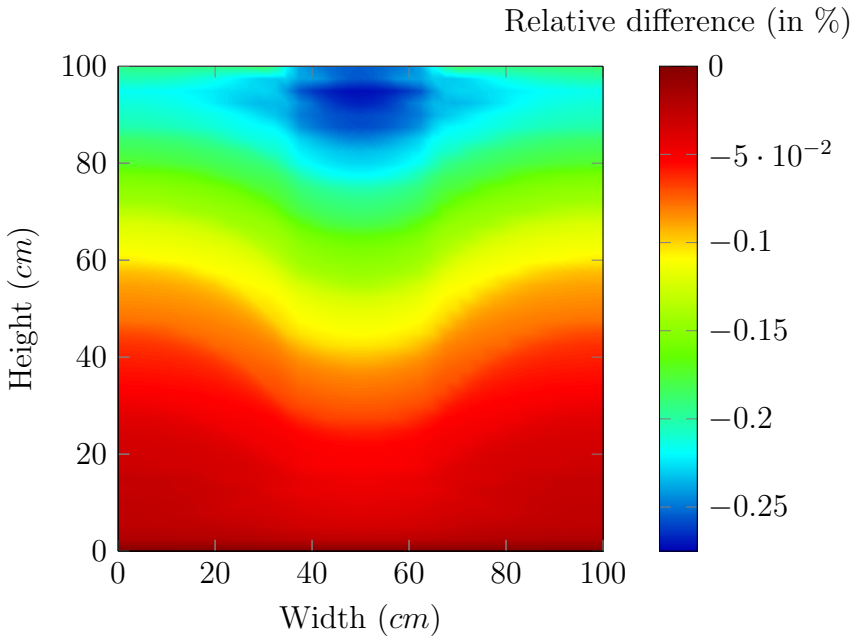

Fig. 3.21. Drainage scenario, isotropic soil: Relative difference (in %) of moisture content between the peridynamic model results and the classic model HYDRUS at 0.2 days. Uniform influence function, $\delta = 1cm$, and a point density value $m = 4$.

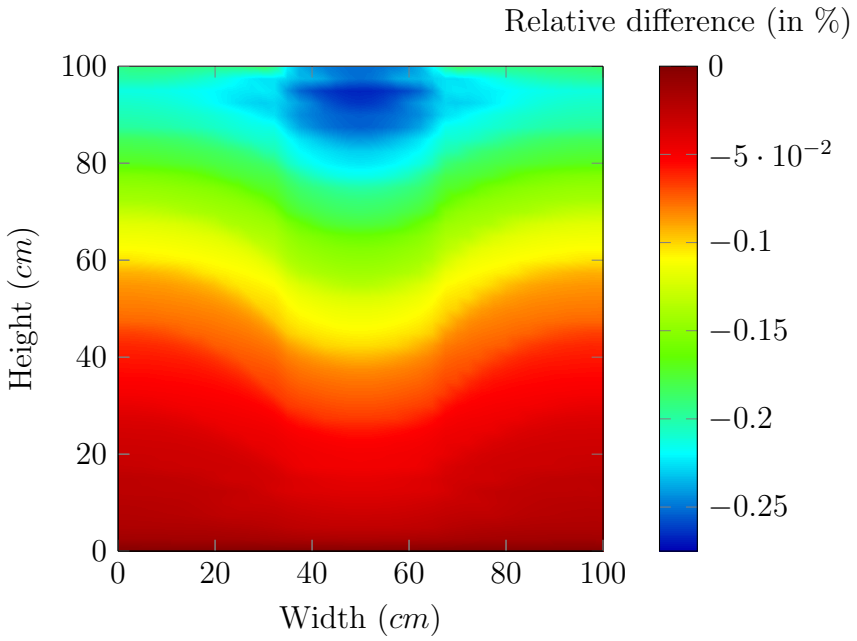

Fig. 3.22. Drainage scenario, isotropic soil: Relative difference (in %) of moisture content between the peridynamic model results and the classic model HYDRUS at 0.2 days. Linear influence function, $\delta = 1cm$, and a point density value $m = 4$.

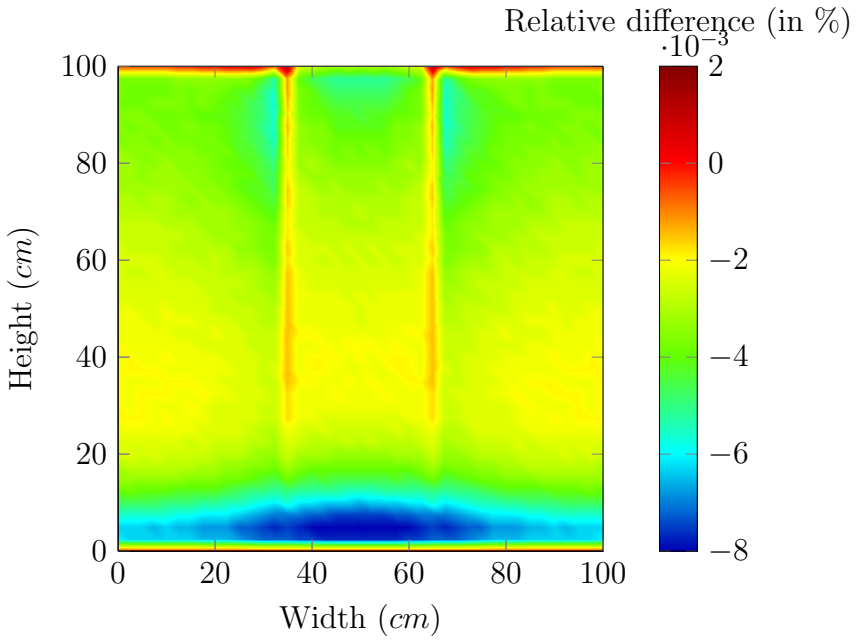

Fig. 3.23. Infiltration scenario, isotropic soil: Relative difference (in %) of moisture content between uniform and triangular influence functions for the peridynamic model at 0.2 days. Horizon radius $\delta = 1cm$, and a point density value $m = 4$.

simulations using the peridynamic model with uniform and triangular influence functions, respectively. All three images have the same color map extents. Following a visual inspection of the images, I observe a very good agreement between the results of the classic model and the peridynamic model for both types of influence functions.

As in the earlier analysis above, I will look at the relative difference of the moisture content between the results of the peridynamic model and the classic model to evaluate the level of agreement between both models and investigate the impact of the type of the influence function on the performance of the model. Figures 3.27 3.28 are the images of the relative difference at 2 hours for the uniform and linear influence functions respectively.

I note from these results that for both influence function types, the relative difference between the peridynamic and the classic models is small, and does not exceed -0.2% for the uniform influence function, and -0.16% for the linear influence function.

The same feature that is observed near the top boundary in the isotropic case is also present, but it is more stretched in the direction of the higher conductivity. I attribute this to the higher conductivity of the soil in Zone Two that is draining faster and pulling more water in from Zone One and Zone Three, which also have a higher conductivity in the horizontal direction that leads to the mobilization of an additional horizontal flow at that depth which extends the region of lower moisture content laterally.

Figure 3.29 is an image of the relative difference between the results of the peridynamic model using a uniform influence function compared to a linear influence function. When compared to the isotropic case, the difference between the results of the uniform and the linear functions are an order of magnitude larger; however, they are still of the order of $10^{-2}\%$. As expected, the uniform function yields lower moisture contents.

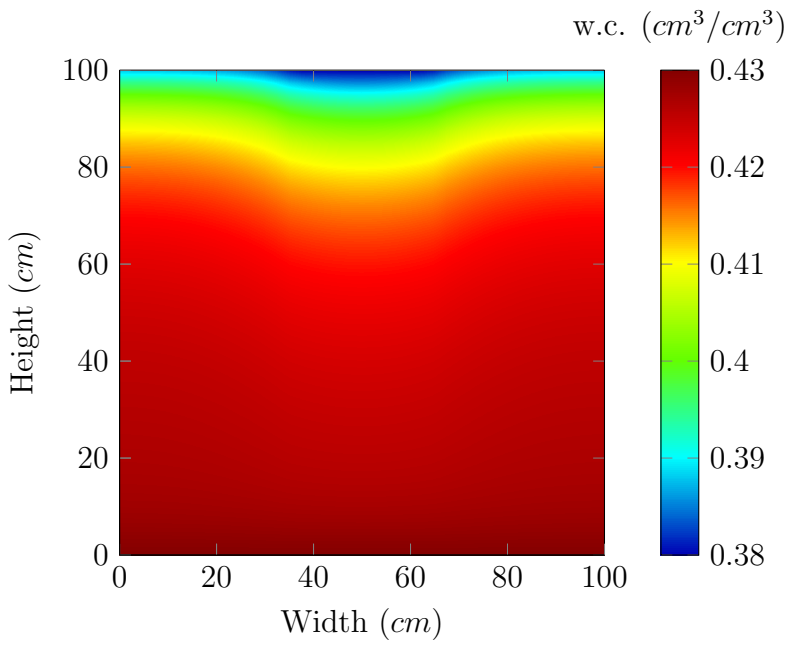

Fig. 3.24. Drainage scenario, anisotropic soil: Hydrus simulation results for moisture content at 0.2 days.

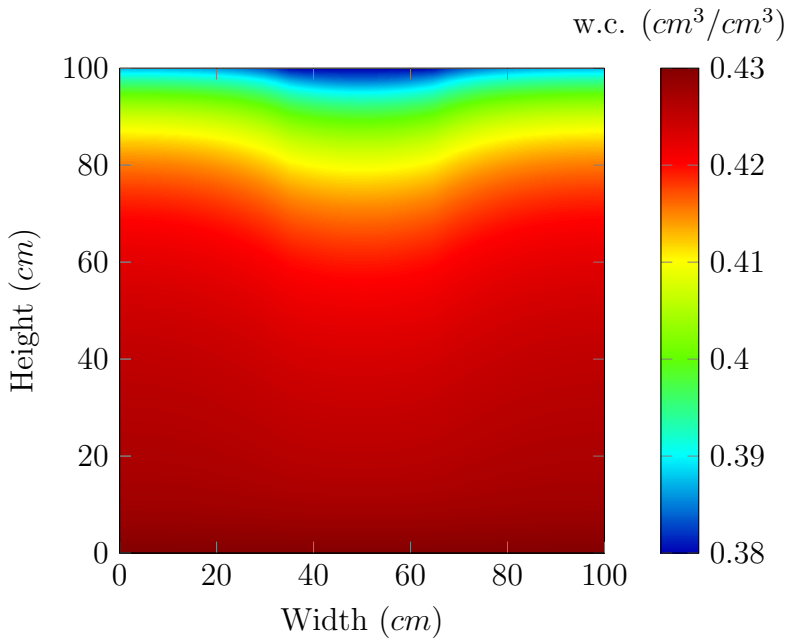

Fig. 3.25. Drainage scenario, anisotropic soil: Peridynamic simulation results for moisture content at 0.2 days. Uniform influence function, $\delta = 1cm$, and a point density value $m = 4$.

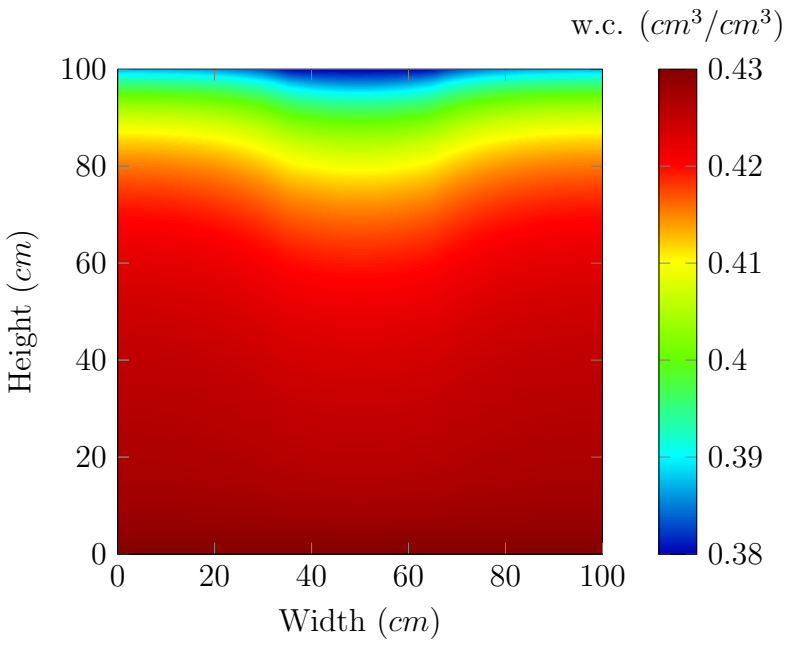

Fig. 3.26. Drainage scenario, anisotropic soil: Peridynamic simulation results for moisture content at 0.2 days. Linear influence function, $\delta = 1cm$, and a point density value $m = 4$.

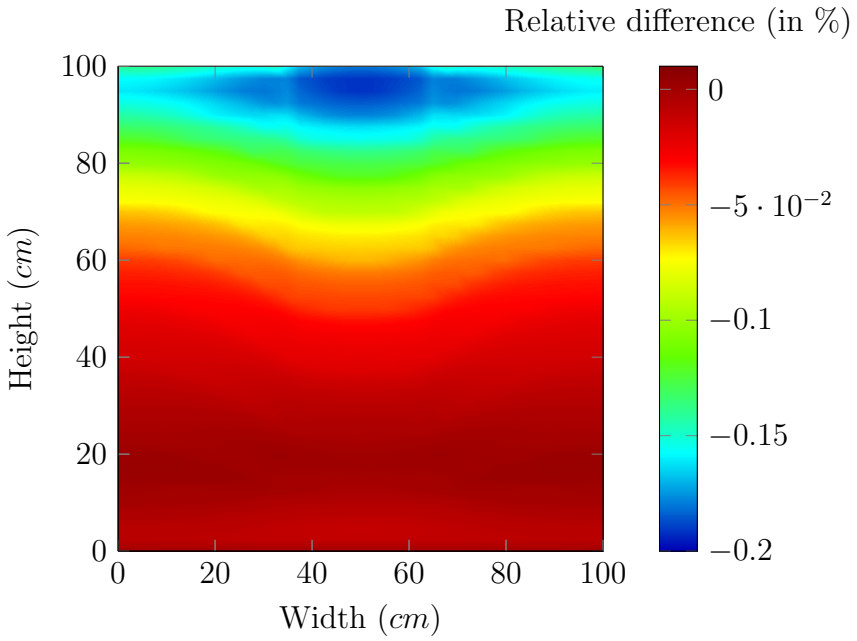

Fig. 3.27. Drainage scenario, anisotropic soil: Relative difference (in %) of moisture content between the peridynamic model results and the classic model HYDRUS at 0.2 days. Uniform influence function, $\delta = 1cm$, and a point density value $m = 4$.

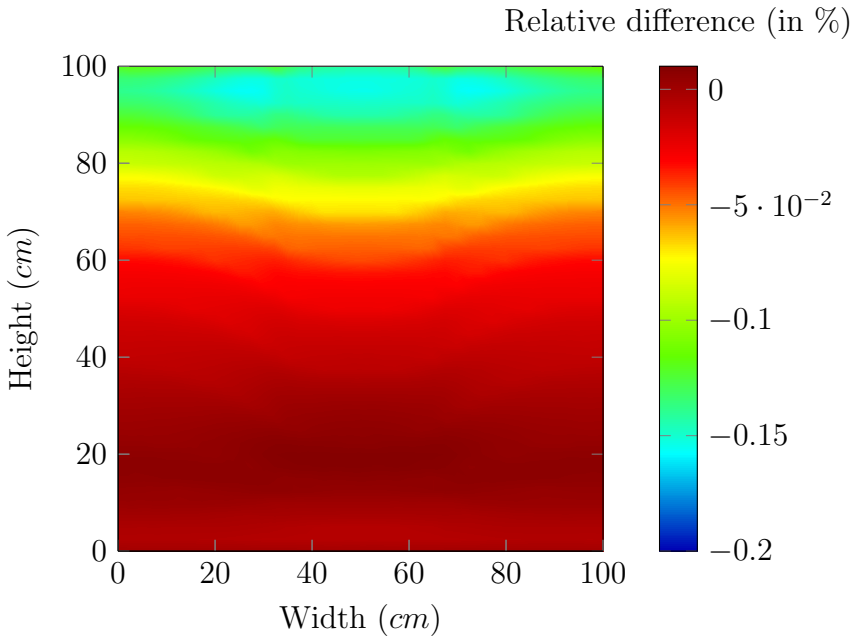

Fig. 3.28. Drainage scenario, anisotropic soil: Relative difference (in %) of moisture content between the peridynamic model results and the classic model HYDRUS at 0.2 days. Linear influence function, $\delta = 1cm$, and a point density value $m = 4$.

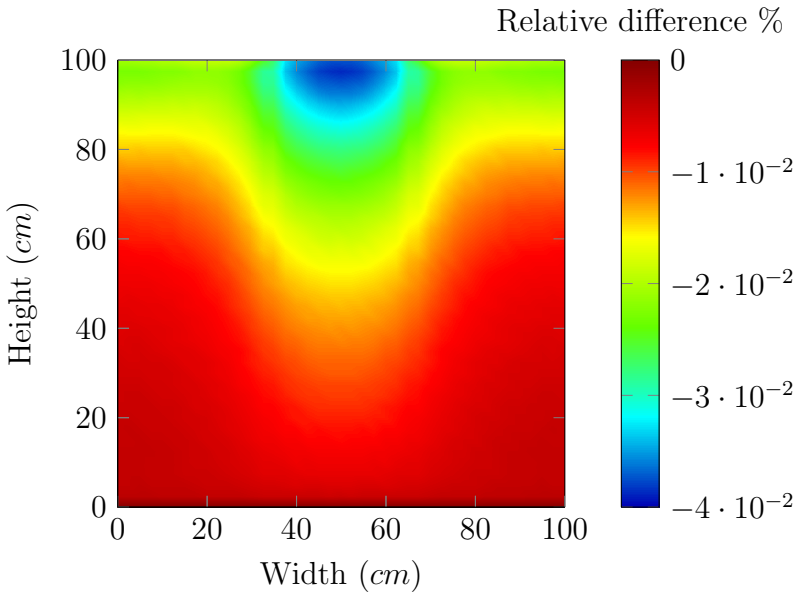

Fig. 3.29. Infiltration scenario, anisotropic soil: Relative difference (in %) of moisture content between uniform and triangular influence functions for the peridynamic model at 0.2 days. Horizon radius $\delta = 1cm$, and a point density value $m = 4$.

3.7 Conclusion

In this study I extended the peridynamic flow model from one dimension to two dimensions. I also extended the expression for the peridynamic hydraulic conductivity to allow the modeling of heterogeneous and anisotropic soils.

The validate the model I discretized the equations and implemented then in a parallel computer code as described in the chapter. Using my code, I simulated scenarios designed to evaluate the performance of the model in capturing moisture flow in homogeneous and heterogeneous soils with isotropic and anisotropic hydraulic conductivities. The same scenarios were also simulated using a classic finite element implementation of the Richard's equation, HYDRUS 2D/3D (Simunek et al., 2006).

Comparing the results of the simulations, I found an excellent agreement between the peridynamic and classic models as made evident by the small relative difference between their results. The differences in moisture content for the isotropic and anisotropic horizontal moisture redistribution scenarios are 0.4%, and 0.7% respectively. These differences are -0.275%, and -0.2% for the scenarios of isotropic and anisotropic drainage in heterogeneous soils.

3.8 References

Abou Najm, M., Mohtar, R. H., Weiss, J., and Braudeau, E. (2009). Assessing internal stress evolution in unsaturated soils. *Water Resources Research*, 45(5):n/a–n/a.

Abou Najm, M. R., Jabro, J. D., Iversen, W. M., Mohtar, R. H., and Evans, R. G. (2010). New method for the characterization of three-dimensional preferential flow paths in the field. *Water Resources Research*, 46(2):n/a–n/a.

Bobaru, F. and Duangpanya, M. (2010). The peridynamic formulation for transient heat conduction. *International Journal of Heat and Mass Transfer*, 53(19–20):4047–4059.

Bobaru, F. and Hu, W. (2012). The meaning, selection, and use of the peridynamic horizon and its relation to crack branching in brittle materials. *International Journal of Fracture*, 176(2):215–222.

Braudeau, E. and Mohtar, R. H. (2006). Modeling the swelling curve for packed soil aggregates using the pedostructure concept. *Soil Science Society of America Journal*, 70(2):494.

Braudeau, E., Mohtar, R. H., El Ghezal, N., Crayol, M., Salahat, M., and Martin, P. (2009). A multi-scale "soil water structure" model based on the pedostructure concept. *Hydrology and Earth System Sciences Discussions*, 6(1):1111–1163.

Buckingham, E. (1907). Studies on the movement of soil moisture: Ii the capillary potential of soil moisture.

Chertkov, V. Y. (2002). Modelling cracking stages of saturated soils as they dry and shrink. *European Journal of Soil Science*, 53(1):105–118.

Darcy, H. (1856). *Les fontaines publiques de la ville de dijon. Exposition et application des principes à suivre et des formules à employer dans les questions de distribution d'eau: Ouvrage terminé par un appendice relatif aux fournitures d'eau de plusieurs villes au filtrage des eaux et à la fabrication des tuyaux de fonte, de plomb, de tole et de bitume*. Dalmont.

Davidson, S. E. and Page, J. B. (1956). Factors influencing swelling and shrinking in soils. *Soil Science Society of America Journal*, 20(3):320–324.

Dinka, T. M. (2012). Review paper: Challenges and limitations in studying the shrink-swell and crack dynamics of vertisol soils. *Open Journal of Soil Science*, 02(02):82–90.

Greco, R. (2002). Preferential flow in macroporous swelling soil with internal catchment: Model development and applications. *Journal of Hydrology*, 269(3–4):150–168.

Greve, A., Andersen, M. S., and Acworth, R. I. (2010). Investigations of soil cracking and preferential flow in a weighing lysimeter filled with cracking clay soil. *Journal of Hydrology*, 393(1):105–113.

Jarvis, N. J. (2007). A review of non-equilibrium water flow and solute transport in soil macropores: Principles, controlling factors and consequences for water quality. *European Journal of Soil Science*, 58(3):523–546.

Kilic, B. and Madenci, E. (2010). Peridynamic theory for thermomechanical analysis. *Advanced Packaging, IEEE Transactions on*, 33(1):97 –105.

Lehoucq, R. and Silling, S. (2008). Force flux and the peridynamic stress tensor. *Journal of the Mechanics and Physics of Solids*, 56(4):1566–1577.

Liu, W. and Hong, J.-W. (2012). Discretized peridynamics for brittle and ductile solids. *International Journal for Numerical Methods in Engineering*, 89(8):1028–1046.

Richards, L. A. (1931). Capillary conduction of liquids through porous mediums. *Physics*, 1(5):318–333.

Sanders, E. C., Abou Najm, M. R., Mohtar, R. H., Kladivko, E., and Schulze, D. (2012). Field method for separating the contribution of surface-connected preferential flow pathways from flow through the soil matrix. *Water Resources Research*, 48(4):n/a–n/a.

Seleson, P. and Parks, M. (2011). On the role of the influence function in the peridynamic theory. *International Journal for Multiscale Computational Engineering*, 9(6):689–706.

Silling, S. (2000). Reformulation of elasticity theory for discontinuities and long-range forces. *Journal of the Mechanics and Physics of Solids*, 48(1):175–209.

Silling, S., Epton, M., Weckner, O., Xu, J., and Askari, E. (2007). Peridynamic states and constitutive modeling. *Journal of Elasticity*, 88(2):151–184.

Silling, S., Lehoucq, R., Aref, H., and van der Giessen, E. (2010). Peridynamic theory of solid mechanics. In *Advances in Applied Mechanics*, volume Volume 44, pages 73–168. Elsevier.

Simunek, J., Sejna, M., and Van Genuchten, M. (2005). The HYDRUS-1D software package for simulating the one-dimensional movement of water, heat, and multiple solutes in variably-saturated media. *University of California, Riverside, Research reports*, 240.

Simunek, J., Van Genuchten, M. T., and Sejna, M. (2006). The hydrus software package for simulating the two-and three-dimensional movement of water, heat, and multiple solutes in variably-saturated media. *Technical manual*, 1.

Van Genuchten, M. T. (1980). A closed-form equation for predicting the hydraulic conductivity of unsaturated soils. *Soil Science Society of America Journal*, 44(5):892–898.

CHAPTER 4. COUPLED MECHANICAL-FLOW PERIDYNAMIC MODEL

4.1 Abstract

A peridynamic model that couples mechanical deformations and transient moisture flow in unsaturated soils is presented. The model merges the peridynamic formulation of the elasticity theory with the peridynamic flow model developed in the previous chapters. Both models are nonlocal alternatives to the classic continuum mechanics formulations and are capable of simulating mechanical deformation and moisture flow in bodies with evolving discontinuities such as cracks. The coupled model simulates the emergence and evolution of cracks caused by the volumetric strains of the soil due to changes in its moisture distribution. The coupled model performance is tested by performing a two dimensional simulation of a soil restrained ring test and comparing the results with the results of the same test carried out in the laboratory.

4.2 Introduction

In problems of solid mechanics, the deformation of a material body is driven by the influence of out-of-balance forces at every material point in the body. The classical formulation of elasticity in continuum mechanics adopts the view that forces at a point arise from the actions of points directly adjacent to it, plus any additional body- and externally applied forces at that point. This leads to the Cauchy equation of motion which is an expression of conservation of momentum describing deformation dynamics given by Equation 4.1:

$$\rho\ddot{\mathbf{u}}(\mathbf{x},t) = \nabla.\sigma(x,t) + \mathbf{b}(x,t). \tag{4.1}$$

Where ρ is mass density, $\ddot{\mathbf{u}}$ is second temporal derivative of the displacement vector, $\mathbf{b}$ is body and external force density vector if available, $\mathbf{x}$ is the position vector, and t is time. $\nabla.\sigma$ is the divergence of the stress tensor σ.

As I mentioned in the previous chapters, the presence of spatial derivatives in Equation 4.1, which are undefined on points where the field is discontinuous, poses a difficulty in the modeling of the deformation of bodies that are prone to cracking. Cracks inside a body are discontinuities in the displacement field and its higher derivatives, and the points falling on the tips and surfaces of cracks are points of singularity of Equation 4.1.

One solution to this shortcoming is the peridynamic model for solid mechanics, a non-local reformulation of the theory of elasticity proposed by Silling (Silling, 2000, Silling et al., 2010). It is based on extending the interaction distance between points from infinitesimal to finite distances, and replacing the term featuring the spatial derivatives, the divergence of the stress ($\nabla.\sigma$), with a derivative free integral functional valid everywhere in the domain.

The peridynamic theory of solid mechanics assumes that a material body is composed of continuous matter, and therefore, falls under the theory of continuous mechanics. However, in contrast with the classic continuous mechanics theory, it assumes that interactions between material points in a body is not limited to points separated by an infinitesimal distance, but extends to points separated by a finite distance as well. This action at a distance that points can exert on each other makes the perydinamic theory a non-local one (Silling, 2000).

The simplest peridynamic model, referred to as the bond-based model (Silling, 2000), assumes pairwise interactions between points and leads to a formulation capable of modeling materials with a Poisson ratio limited to 0.25. A more general formulation of peridynamics, the state-based formulation, where the force at some points is the result of the combined deformations of all the points interacting with it, extends the capacity of the theory to more general material responses (Silling et al., 2007).

Previously, I presented the peridynamic flow model for transient moisture flow in unsaturated soils. Similar to the peridynamic model for solid mechanics in motivation and form, the flow model is a formulation that allows the modeling of transient moisture flow in unsaturated soils prone to spurious field discontinuities due to soil cracking induced by volumetric strains (i.e: shrinkage and swelling), caused by changes in moisture content (i.e.: increase and decrease). This is achieved by a non-local, derivative free reformulation of Richards Equation where an integral functional replaces the spatial derivative terms, rendering the model equations valid at every point in the domain, including points of discontinuities.

Now that I have peridynamic models for moisture flow and mechanical deformation, I can move forward with the development of a coupled flow-deformation peridynamic model. It will be based on the bond-based model for solid mechanics. The coupling between processes of moisture flow and mechanical deformation in a common medium representation allows me to incorporate the volumetric strains in the soil driven by moisture flow and changes in moisture content into the mechanical analysis to predict and localize the initiation and development of soil cracks in space and time which will be automatically incorporated in the topology of the domain altering paths of moisture flow and, in turn, steer the evolution of the mechanical analysis accordingly.

4.3 Peridynamic model of solid mechanics

The bond-based peridynamic model for solid mechanics states that between every two material points $\mathbf{x}$ and $\mathbf{x}'$, in a body, there exists a direct pairwise interaction. This is given by the vector valued function $\mathbf{f}$, which is called the pairwise force function and is a function of the displacement field relative to the reference configuration. The pairwise force function has the units of force per

volume squared, i.e.: the force that point $\mathbf{x}'$ exerts on point $\mathbf{x}$ per unit volume of $\mathbf{x}'$ per unit volume of $\mathbf{x}$ in the reference configuration (Silling, 2000):

$$\mathbf{f}(\mathbf{x}|\mathbf{x}', t) = \mathbf{f}(\mathbf{u}(\mathbf{x}', t), \mathbf{u}(\mathbf{x}, t), \mathbf{x}', \mathbf{x}). \tag{4.2}$$

where $\mathbf{f}$ is the pairwise force function, $\mathbf{u}$ is the displacement vector, $\mathbf{x}$ is the position vector in the reference configuration, and t is time.

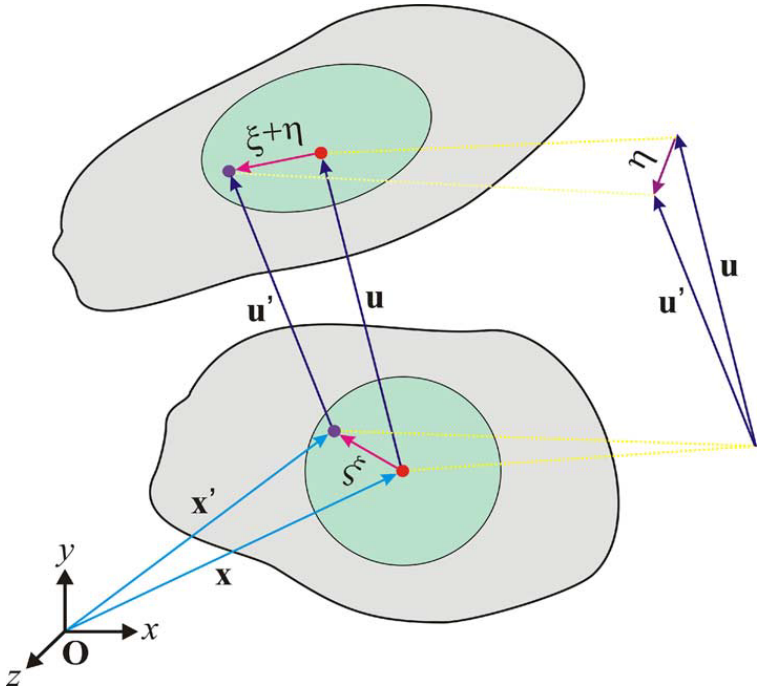

Fig. 4.1. Diagram showing a body in the reference and the deformed configurations, annotated with the peridynamic vector terminology (Kilic and Madenci, 2010).

In the case of a homogeneous material, the pairwise force becomes a function of the displacement difference and the relative position of the pair in the reference configuration (Silling, 2000):

$$\mathbf{f}(\mathbf{x}|\mathbf{x}', t) = \mathbf{f}\left(\mathbf{u}(\mathbf{x}', t) - \mathbf{u}(\mathbf{x}, t), \mathbf{x}' - \mathbf{x}\right). \tag{4.3}$$

To be consistent with the notation used in the peridynamics literature, I define the vectors $\boldsymbol{\eta}$ and $\boldsymbol{\xi}$. $\boldsymbol{\eta}$ is the relative displacement of the interacting pair, and $\boldsymbol{\xi}$ is its relative position in the reference configuration (Figure 4.1):

$$\boldsymbol{\eta} = \mathbf{u}' - \mathbf{u}, \quad \boldsymbol{\xi} = \mathbf{x}' - \mathbf{x}. \tag{4.4}$$

where, to simplify the notation, I performed the following substitutions:

$$\mathbf{u} = \mathbf{u}(\mathbf{x}, t), \quad \mathbf{u}' = \mathbf{u}(\mathbf{x}', t). \tag{4.5}$$

The pairwise force function $\mathbf{f}$ now becomes:

$$\mathbf{f}(\boldsymbol{\eta}, \boldsymbol{\xi}) = \mathbf{f}\left(\mathbf{u}(\mathbf{x}', t) - \mathbf{u}(\mathbf{x}, t), \mathbf{x}' - \mathbf{x}\right). \tag{4.6}$$

Given the definition of the pairwise function $\mathbf{f}$, it follows that the total force felt by point $\mathbf{x}$ per unit reference volume, excluding local body forces, is the total of all its pairwise interactions, and it is given by the following integral functional:

$$\mathbf{L}(\mathbf{x}, t) = \int_{\mathcal{H}_x} \mathbf{f}(\boldsymbol{\eta}, \boldsymbol{\xi}) \mathrm{d}V_{x'}. \tag{4.7}$$

where $\mathbf{L}$ is the total force at $\mathbf{x}$ per unit reference volume, the domain of integration $\mathcal{H}_x$ is the set of all points $\mathbf{x}'$ interacting with point $\mathbf{x}$ through pairwise interactions, and $\mathrm{d}V_{x'}$ is the differential volume of points $\mathbf{x}'$ in the reference configuration.

The set $\mathcal{H}_x$ could include the entire domain Ω. However, for practical purposes I assume that pairwise interactions exist only between points separated by up to a certain maximum distance δ:

$$\mathbf{f}(\boldsymbol{\eta}, \boldsymbol{\xi}) = 0 \quad if\ |\xi| > \delta. \tag{4.8}$$

This restriction on $\mathbf{f}$ would limit the extent of $\mathcal{H}_x$ to a sphere of radius δ centered on point $\mathbf{x}$.

$$\mathcal{H}_x = \left\{\boldsymbol{x'} \in \boldsymbol{\Omega} \mid 0 \leq \|\boldsymbol{x'} - \boldsymbol{x}\| \leq \delta\right\}. \tag{4.9}$$

where $\mathcal{H}_x$ is called the horizon of point $\mathbf{x}$, and δ, the maximum interaction distance, is called the radius of the horizon of $\mathbf{x}$.

Invoking the principle of conservation of linear momentum (or Newton's Second Law), the peridynamic equivalent of the differential equation of motion (Equation 4.1) for a homogeneous material can now be written as the following integro-differential equation:

$$\rho\ddot{\mathbf{u}}(\mathbf{x},t) = \int_{\mathcal{H}_x} \mathbf{f}(\boldsymbol{\eta},\boldsymbol{\xi})\mathrm{d}V_{x'} + \mathbf{b}(\mathbf{x},t). \tag{4.10}$$

where ρ is mass density, $\ddot{\mathbf{u}}$ is the acceleration, and $\mathbf{b}$ is body and external force density vector per unit reference volume if available.

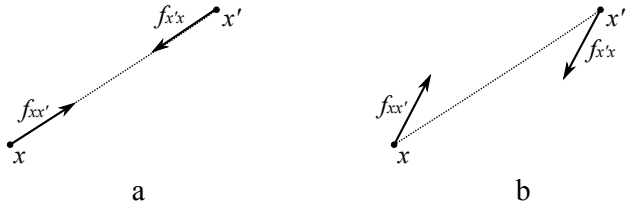

Fig. 4.2. Pairwise forces. a) Forces satisfying Newton's Third Law and conservation of angular momentum. b) Forces satisfying Newton's Third but violating conservation of angular momentum.

To comply with the laws of physics, some restrictions must be placed on the pairwise force function $\mathbf{f}$. The first restriction is that $\mathbf{f}$ is an odd function (Silling, 2000, Silling et al., 2010). This is a consequence of Newton's Third Law of motion which states that for every action there is an equal and opposite reaction, i.e.: the force exerted on a point $\mathbf{x}$ by a point $\mathbf{x}'$ is equal in magnitude and opposite in direction to the force exerted by $\mathbf{x}$ on $\mathbf{x}'$ (Figure 4.2a).

$$\mathbf{f}(\mathbf{x}|\mathbf{x}',t) = -\mathbf{f}(\mathbf{x}'|\mathbf{x},t). \tag{4.11}$$

or,

$$\mathbf{f}(-\boldsymbol{\eta},-\boldsymbol{\xi}) = -\mathbf{f}(\boldsymbol{\eta},\boldsymbol{\xi}). \tag{4.12}$$

The second restriction is due to the conservation of angular momentum which requires that $\mathbf{f}$ be collinear with the direction of the interacting pair of points in the current configuration (Silling, 2000, Silling et al., 2010). Otherwise, internal torques could be present that are unbalanced by externally applied forces (Figure 4.2b).

$$\mathbf{f}(\boldsymbol{\eta},\boldsymbol{\xi}) = F(\boldsymbol{\eta},\boldsymbol{\xi})\frac{(\boldsymbol{\xi}+\boldsymbol{\eta})}{\|\boldsymbol{\xi}+\boldsymbol{\eta}\|}. \tag{4.13}$$

where the function F is an even scalar valued function equal to the magnitude of the pairwise force:

$$F(-\boldsymbol{\eta},-\boldsymbol{\xi}) = F(\boldsymbol{\eta},\boldsymbol{\xi}). \tag{4.14}$$

Using equation 4.13 with equation 4.10 I get the following peridynamic equation of motion:

$$\rho\ddot{\mathbf{u}}(\mathbf{x},t) = \int_{\mathcal{H}_x} F(\boldsymbol{\eta},\boldsymbol{\xi})\frac{(\boldsymbol{\xi}+\boldsymbol{\eta})}{\|\boldsymbol{\xi}+\boldsymbol{\eta}\|}\,\mathrm{d}V_{x'} + \mathbf{b}(\mathbf{x},t). \tag{4.15}$$

4.3.1 Microelastic peridynamic material

In the proposed coupled flow-deformation peridynamic model, I assume the modeled peridynamic material is a proportional microelastic material when describing the behavior of the pairwise interactions. It is a model where all the work done during the deformation of a pair from its reference configuration is stored as recoverable elastic potential energy (Silling, 2000). This relationship is expressed as:

$$\mathbf{f}(\boldsymbol{\eta},\boldsymbol{\xi}) = \frac{\partial w}{\partial \boldsymbol{\eta}}(\boldsymbol{\eta},\boldsymbol{\xi}). \tag{4.16}$$

where w is the potential energy density stored in an interacting pair and has the units of energy per volume squared; it is called the micropotential (Silling, 2000, Silling et al., 2010). The usefulness of w will become evident later on in the chapter when I present the derivation of the peridynamic material constant and extend the model to include cracking.

In a sense, a microelastic material behaves as if any pairwise interaction between points $\mathbf{x}$ and $\mathbf{x}'$ were the result of an elastic spring connecting points $\mathbf{x}$ and $\mathbf{x}'$ (Equation 4.17).

$$F(\boldsymbol{\eta}, \boldsymbol{\xi}) = C(\boldsymbol{\eta}, \boldsymbol{\xi})\, s(\boldsymbol{\eta}, \boldsymbol{\xi}). \tag{4.17}$$

where C is the peridynamic material micromodulus function, and s is the stretch of $\mathbf{x}\mathbf{x}'$ defined by:

$$s(\boldsymbol{\eta}, \boldsymbol{\xi}) = \frac{|\boldsymbol{\xi} + \boldsymbol{\eta}| - |\boldsymbol{\xi}|}{|\boldsymbol{\xi}|}. \tag{4.18}$$

where $|\boldsymbol{\xi} + \boldsymbol{\eta}|$ is the length of $\mathbf{x}\mathbf{x}'$ in the current (deformed) configuration, and $|\boldsymbol{\xi}|$ is the length of $\mathbf{x}\mathbf{x}'$ in the initial configuration.

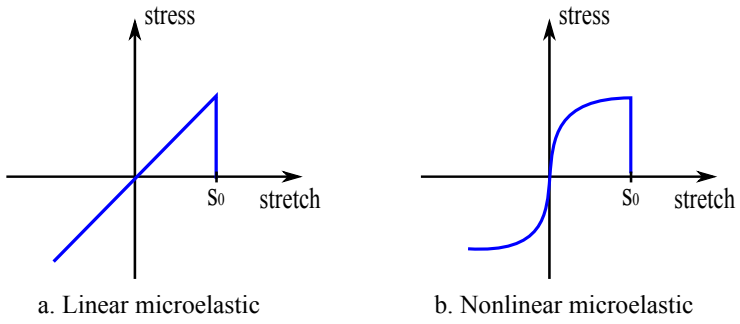

Fig. 4.3. Peridynamic material models. a) linear microelastic. b) non-linear microelastic model.

The dependence of the micromodulus C on $\boldsymbol{\eta}$ and $\boldsymbol{\xi}$ is to allow for a nonlinear response of the pairwise interaction (Figure 4.3a). However, in what follows I will restrict the material model to a linear microelastic model where the pairwise force between any pair of points $\mathbf{x}$ and $\mathbf{x}'$ is linearly proportional to the stretch of the pair (Figure 4.3b).

4.3.2 Influence functions

In addition to the radius of the horizon δ, the non-local behavior of the model can be further modulated by introducing a dependence of the magnitude of the pairwise force on the length of the peridynamic bond in the reference configuration using a scalar valued influence function (Figure 4.4). Incorporating the influence function into the definition of the micromodulus function of a homogeneous, isotropic, and linear microelastic material, I get the following:

$$C(\boldsymbol{\xi}) = \begin{cases} B(|\boldsymbol{\xi}|)Cp & \text{if } |\boldsymbol{\xi}| \leq \delta \\ 0 & \text{otherwise} \end{cases} \tag{4.19}$$

where B is an influence function that depends on the length of the peridynamic bond in the reference configuration, $|\boldsymbol{\xi}|$, and Cp is the microelastic modulus.

The simplest influence function is a uniform function, where the pairwise force is independent of the length of the bond within the horizon, and the non-locality of the model is only controlled by the radius of the horizon (Silling, 2000, Silling et al., 2010, Simunek et al., 2005, Bobaru and Duangpanya, 2010, Bobaru and Hu, 2012). The dependence could also be linear, with the influence being maximum at the center of the horizon, and drops linearly with length (Bobaru and Duangpanya, 2010, Bobaru and Hu, 2012). In developing a thermo-mechanical peridynamic model, (Kilic and Madenci, 2010) used a normal distribution, where the "internal length" of the material is modulated by the standard deviation. And, in assessing the role of influence function on wave propagation in an elastic medium, Seleson and Parks used a family of spherical influence functions (Seleson and Parks, 2011).

In the following, I will use the same influence functions utilized in developing the peridynamic flow model: a uniform influence function, and a linear influence

function that vanishes at the edge of the horizon where $|\boldsymbol{\xi}| = \delta$ (Equation 4.20 and Figure 4.4).

$$B(|\boldsymbol{\xi}|) = \begin{cases} 1 & \text{if uniform} \\ 1 - \dfrac{|\boldsymbol{\xi}|}{\delta} & \text{if linear} \end{cases} \tag{4.20}$$

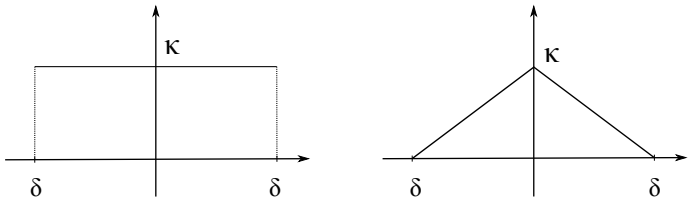

Fig. 4.4. Uniform and triangular influence functions.

Using the corresponding influence function, the peridynamic equation of motion for a uniform and a linear influence function are given by Equations 4.21 and 4.22 respectively.

$$\rho\ddot{\mathbf{u}}(\mathbf{x},t) = \int_{\mathcal{H}_x} Cp_u \, s(\boldsymbol{\eta},\boldsymbol{\xi}) \, \frac{(\boldsymbol{\xi}+\boldsymbol{\eta})}{\|\boldsymbol{\xi}+\boldsymbol{\eta}\|} \, \mathrm{d}V_{x'} + \mathbf{b}(\mathbf{x},t). \tag{4.21}$$

and for a linear influence function it becomes:

$$\rho\ddot{\mathbf{u}}(\mathbf{x},t) = \int_{\mathcal{H}_x} Cp_l \left(1 - \frac{|\boldsymbol{\xi}|}{\delta}\right) s(\boldsymbol{\eta},\boldsymbol{\xi}) \, \frac{(\boldsymbol{\xi}+\boldsymbol{\eta})}{\|\boldsymbol{\xi}+\boldsymbol{\eta}\|} \, \mathrm{d}V_{x'} + \mathbf{b}(\mathbf{x},t). \tag{4.22}$$

where Cp_u and Cp_l are the peridynamic material micromoduli for models using a uniform and a linear influence function, respectively.

4.3.3 Peridynamic micromodulus

The peridynamic micromodulus can be related to the measurable elastic constants used in the classic formulation. This relationship can be derived by equating the classic deformation energy density function with its peridynamic equivalent (Silling, 2000).

Consider a linear elastic, homogeneous and isotropic, infinite body under isotropic extension with a constant stretch $s(\boldsymbol{\eta}, \boldsymbol{\xi}) = s$. This leads to the following relationship:

$$\boldsymbol{\eta} = s\boldsymbol{\xi}. \tag{4.23}$$

and:

$$s = \frac{\eta}{\xi}. \tag{4.24}$$

with $\eta = |\boldsymbol{\eta}|$, and $\xi = |\boldsymbol{\xi}|$

Rearranging Equation 4.16 and using Equation 4.13 leads to the following equation for the change in displacement energy density per unit reference volume squared per unit relative displacement of a peridynamic bond:

$$\begin{aligned} \partial w(\boldsymbol{\eta}, \boldsymbol{\xi}) &= \mathbf{f}(\boldsymbol{\eta}, \boldsymbol{\xi}) \, . \partial \boldsymbol{\eta} \\ &= F(\boldsymbol{\eta}, \boldsymbol{\xi}) \, \partial \eta. \end{aligned} \tag{4.25}$$

Integrating Equation 4.25 from the reference configuration to a displacement η, I get the total displacement energy density stored in a bond per unit reference volume squared:

$$w(\boldsymbol{\eta}, \boldsymbol{\xi}) = \int_0^{\eta} F(\boldsymbol{\eta}, \boldsymbol{\xi}) \, \partial \eta. \tag{4.26}$$

Considering that this energy is stored in a pairwise bond, it is acceptable to treat it as if half of it is stored in each one of the points, and that the total energy density stored at some point $\mathbf{x}$ is the sum of its share of all the energy densities in all the bonds connected to it. This is given by the following functional:

$$W(\mathbf{x}, t) = \frac{1}{2} \int_{\mathcal{H}_x} w(\boldsymbol{\eta}, \boldsymbol{\xi}) \, \mathrm{d}V_{x'}. \tag{4.27}$$

where $W(\mathbf{x}, t)$ is the total elastic deformation energy density at point $\mathbf{x}$ at time t.

Plugging Equations 4.17 and 4.26 in Equation 4.19, and replacing F by the resultant function, Equation 4.26 becomes:

$$\begin{aligned} w(\boldsymbol{\eta}, \boldsymbol{\xi}) &= \int_0^{\eta} B(\boldsymbol{\xi}) Cp \frac{\boldsymbol{\eta}}{\boldsymbol{\xi}} \, \partial\eta \\ &= B(\boldsymbol{\xi}) Cp \frac{\eta^2}{2\xi} \\ &= B(\boldsymbol{\xi}) Cp \frac{s^2 \xi}{2}. \end{aligned} \tag{4.28}$$

and plugging Equation 4.28 in Equation 4.27 I get:

$$W(\mathbf{x}, t) = \frac{1}{2} \int_{\mathcal{H}_x} B(\boldsymbol{\xi}) Cp \frac{s^2 \xi}{2} \, \mathrm{d}V_{x'}. \tag{4.29}$$

The integral in Equation 4.29 is evaluated after replacing B by the corresponding function from 4.20, and performing a change of variable by selecting $\mathrm{d}V_{x'}$ by the corresponding entry from 4.30 depending on the number of dimensions of the model.

$$\mathrm{d}V_{x'} = \begin{cases} 2 \, \mathrm{d}\xi & \text{for 1D} \\ 2\pi\xi \, \mathrm{d}\xi & \text{for 2D} \\ 4\pi\xi^2 \, \mathrm{d}\xi & \text{for 3D} \end{cases} \tag{4.30}$$

For a one dimensional peridynamic model using a uniform influence function, and having a horizon radius δ, the total elastic energy density at point $\mathbf{x}$ is given by:

$$\begin{aligned} W_{u1D}(\mathbf{x}, t) &= \frac{1}{2} \int_0^{\delta} 2 Cp_{u1D} \frac{s^2 \xi}{2} \, \mathrm{d}\xi \\ &= Cp_{u1D} \frac{s^2 \delta^2}{4}. \end{aligned} \tag{4.31}$$

For a two dimensional model I have:

$$\begin{aligned} W_{u2D}(\mathbf{x}, t) &= \frac{1}{2} \int_0^{\delta} 2\pi\xi Cp_{u2D} \frac{s^2 \xi}{2} \, \mathrm{d}\xi \\ &= Cp_{u2D} \frac{\pi s^2 \delta^3}{6}. \end{aligned} \tag{4.32}$$

For a three dimensional model I have:

$$W_{u3D}(\mathbf{x},t) = \frac{1}{2}\int_0^{\delta} 4\pi\xi^2 Cp_{u3D}\frac{s^2\xi}{2}\,\mathrm{d}\xi$$
$$= Cp_{u3D}\frac{\pi s^2\delta^4}{4}. \tag{4.33}$$

where Cp_{u1D}, Cp_{u2D}, and Cp_{u3D} are the peridynamic moduli in the case of a uniform influence function, for a model in one, two, and three dimensions respectively.

Similarly, a model using a linear influence function is given by Equations 4.34 to 4.36.

$$W_{l1D}(\mathbf{x},t) = Cp_{l1D}\frac{s^2\delta^2}{12}. \tag{4.34}$$

$$W_{l2D}(\mathbf{x},t) = Cp_{l2D}\frac{\pi s^2\delta^3}{24}. \tag{4.35}$$

$$W_{l3D}(\mathbf{x},t) = Cp_{l3D}\frac{\pi s^2\delta^4}{20}. \tag{4.36}$$

where Cp_{l1D}, Cp_{l2D}, and Cp_{l3D} are the peridynamic moduli in the case of a linear influence function, for a model in one, two, and three dimensions respectively.

On the other hand, in the classic formulation of elasticity, the elastic deformation energy for a uniform and isotropic material is given by:

$$W_{Cl} = \frac{1}{2}\sigma_{ij}\epsilon_{ij}. \tag{4.37}$$

where E is Young's modulus, σ is the stress, ϵ is the strain.

Under isotropic extension, Equation 4.37 in one, two, and three dimensions is given by Equations 4.38 to 4.40 respectively.

$$W_{Cl1D} = \frac{1}{2}E\epsilon^2. \tag{4.38}$$

$$W_{Cl2D} = \frac{E}{(1-\nu)}\epsilon^2. \tag{4.39}$$

$$W_{Cl3D} = \frac{3}{2}\frac{E}{(1-2\nu)}\epsilon^2. \tag{4.40}$$

where ν is Poisson's ratio.

Setting $\epsilon = s$ and equating equations 4.31 and 4.34 with Equation 4.38, and Equations 4.32 and 4.35 with Equation 4.39, and Equations 4.33 and 4.36 with Equation 4.40, I get the peridynamic moduli in one dimension for a uniform and linear influence function, in two dimensions for a uniform and linear influence function, and in three dimensions for a uniform and linear influence function. These results are listed in table 4.1.

Table 4.1
Peridynamic moduli.

	$1D$	$2D$	$3D$
Uniform	$\frac{2E}{\delta^2}$	$\frac{6E}{\pi(1-\nu)\delta^3}$	$\frac{6E}{\pi(1-2\nu)\delta^4}$
Linear	$\frac{6E}{\delta^2}$	$\frac{24E}{\pi(1-\nu)\delta^3}$	$\frac{30E}{\pi(1-2\nu)\delta^4}$

4.3.4 Convergence to the classic formulation

At the limit of the horizon going to zero, the peridynamic equation of motion converges to the classic equation of motion (Silling, 2000, Silling et al., 2010). Specifically, for a linear elastic, homogeneous, and isotropic material I have that:

$$\lim_{\delta\to 0}\int_{\mathcal{H}_x}\mathbf{f}(\boldsymbol{\eta},\boldsymbol{\xi})\mathrm{d}V_{x'} = E\nabla^2 u(x,t). \tag{4.41}$$

Silling and Lehoucq, and Emmrich and Weckne have demonstrated the convergence of the general state based peridynamic formulation to the classic formulation at the limit of vanishing horizon (Silling and Lehoucq, 2008,

Emmrich and Weckner, 2007). In the following I will demonstrate the convergence of the peridynamic model for a proportional microelastic material using a uniform influence function in one dimension.

Consider points $\mathbf{x}$ at positon (x) and $\mathbf{x}'$ at position $(x+s)$ in a one dimensional body, with displacements $u(x)$ and $u(x+s)$. The pairwise force at $\mathbf{x}$ due to $\mathbf{x}'$ is given by:

$$\begin{aligned} f(x, x+s) &= Cp_{u1D} \frac{(u(x+s) - u(x))}{|s|} \\ &= \frac{2E}{\delta^2} \frac{(u(x+s) - u(x))}{|s|}. \end{aligned} \tag{4.42}$$

Performing a Taylor expansion of Equation 4.42 with respect to d I get the following:

$$f(x, x+s) = \frac{2E \operatorname{sgn}(s)}{\delta^2} \left(\frac{\partial u}{\partial x} + \frac{d}{2} \frac{\partial^2 u}{\partial x^2} + \frac{d^2}{6} \frac{\partial^3 u}{\partial x^3} + \frac{d^3}{24} \frac{\partial^4 u}{\partial x^4} + \frac{d^4}{120} \frac{\partial^5 u}{\partial x^5} + \frac{d^5}{720} \frac{\partial^6 u}{\partial x^6} + \mathcal{O}(d^6) \right). \tag{4.43}$$

and the total force at $\mathbf{x}$ due from all its pairwise interactions is:

$$\int_{-\delta}^{\delta} f(x, x+s) \, \mathrm{d}s = E \left(\frac{\partial^2 u}{\partial x^2} + \frac{s^2}{24} \frac{\partial^4 u}{\partial x^4} + \frac{s^4}{1080} \frac{\partial^6 u}{\partial x^6} + ... \right). \tag{4.44}$$

taking the limit of Equation 4.44 at $\delta \to 0$ I recover the classic form:

$$\lim_{\delta \to 0} \int_{-\delta}^{\delta} f(x, x+s) \, \mathrm{d}s = E \frac{\partial^2 u}{\partial x^2}. \tag{4.45}$$

4.3.5 Peridynamic stress measures in 2D

Although the peridynamic formulation is based on forces and displacement instead of stresses and strains, there is a value in deriving a peridynamic stress measure in order to relate it to the classic elasticity theory and to compare results from both theories using a common measure.

Lehoucq and Silling have proposed a definition of a peridynamic stress normal to a surface S at some point $\mathbf{x}$ as the sum of the normal components to S of all the

forces in peridynamic bonds that intersect with the surface S at $\mathbf{x}$ per unit area (Lehoucq and Silling, 2008). In other words, it is the resultant of all the actions that points on one side of S exert on points on the other side of S at point $\mathbf{x}$ per unit area.

Consider a point $\mathbf{x}$ in a material body. The pairwise forces that intersect with $\mathbf{x}$ are limited to bonds between points located within the horizon of $\mathbf{x}$. Moreover, in order for a bond $\mathbf{x}'\mathbf{x}''$ to contribute to the stress at $\mathbf{x}$, the segments $\mathbf{x}'\mathbf{x}$ and $\mathbf{x}'\mathbf{x}''$ should be parallel.

Following the same steps for deriving the moisture flux outlined in Chapter 2, Subsection 3.4.1, I get the following expression for the stress at point $\mathbf{x}$ normal to the direction ϕ for two dimensional problems:

$$\sigma_{\perp\phi}(\mathbf{x},t) = -\int_{\delta}^{0}\int_{\pi}^{2\pi}\int_{r_2}^{\delta} B(r1+r2)Cp_{U/l2D}\frac{\mathbf{u}(\mathbf{x}'')-\mathbf{u}(\mathbf{x}')}{r_1+r2}r_1 sin(\theta+\phi)\,\mathrm{d}r_1\mathrm{d}\phi_{x'}\mathrm{d}r_2. \tag{4.46}$$

with:

$$\mathbf{x} = (x,y)\,, \tag{4.47}$$

$$\mathbf{x}' = (x + r_{x'}cos(\phi_{x'}), y + r_{x'}sin(\phi_{x'}))\,, \tag{4.48}$$

$$\mathbf{x}'' = (x' + r_{x''}cos(\phi_{x'} - \pi), y' + r_{x''}sin(\phi_{x'} - \pi))\,. \tag{4.49}$$

4.3.6 Damage and critical stretch

In order to simulate damage and crack formation, I need to introduce a new function to the peridynamic formulation. The damage function μ is a function of the stretch s of a peridynamic bond and is given by:

$$\mu(\boldsymbol{\eta},\boldsymbol{\xi}) = \begin{cases} 1 & \text{if } s(\boldsymbol{\eta},\boldsymbol{\xi}) < s_0 \\ 0 & \text{otherwise} \end{cases} \tag{4.50}$$

where s_0 is a minimum valued equal to the maximum stretch a peridynamic bond can have. Beyond the critical stretch s_0, the bond breaks and the pairwise force drops to zero (Silling, 2000, Silling et al., 2010).

In other words, the recoverable deformation energy density that a peridynamic bond can store reaches a maximum at a stretch $s_m = s_0$ (Foster, 2009). When this critical energy density is exceeded, the bond fails and the energy stored in it is transferred from its previously connected points to the points they are still interacting with within their respective horizons. This release of energy triggers a reconfiguration of the domain towards one with a lower energy state. Displacements during this reconfiguration could lead to other bonds reaching their critical stretch, which leads to a propagation and coalescence of cracks in an automatic manner without the need of additional crack initiation criteria and propagation models (Silling and Askari, 2005).

Incorporating the damage function μ in the formulation, the peridynamic equation of motion becomes:

$$\rho\ddot{\mathbf{u}}(\mathbf{x},t) = \int_{\mathcal{H}_x} \mu(\boldsymbol{\eta},\boldsymbol{\xi}) B(\xi) Cp\, S_m(\boldsymbol{\eta},\boldsymbol{\xi}) \frac{(\boldsymbol{\xi}+\boldsymbol{\eta})}{\|\boldsymbol{\xi}+\boldsymbol{\eta}\|} \mathrm{d}V_{x'} + \mathbf{b}(\mathbf{x},t). \tag{4.51}$$

The critical stretch s_0 can be related to the strain energy dissipation rate G_0, which is the amount of energy dissipated during the process of formation of a new unit surface area of crack (Silling and Askari, 2005).

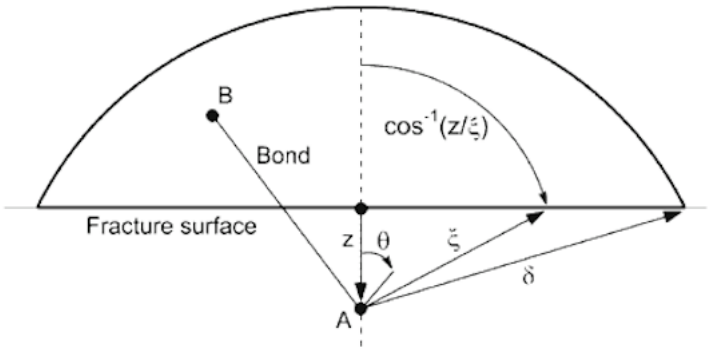

Fig. 4.5. Fracture calculation diagram (Ha and Bobaru, 2010).

Consider figure 4.5. The amount of energy required for a complete fracture along the surface S is the energy required to break all bonds connecting points

on one side of S to points on the other side; therefore, all said bonds must have a stretch of s_0. However, the amount of energy required to create a new one unit surface area of crack, which in two dimensions is one unit length, is equal to that required to break all bonds intersecting with one unit length of the surface, which is the energy required for complete separation divided by the total length of the crack. Because all the relevant bonds have the same stretch, this energy is equal to the energy in the bonds connecting points from one side of the surface that fall on a line normal to the surface, i.e.: the half-line $[OA)$, with points on the other side (Silling and Askari, 2005, Foster, 2009, Ha and Bobaru, 2010).

$$G_0 = 2\int_0^{\delta}\int_z^{\delta}\int_0^{cos^{-1}(\frac{z}{\xi})} w(\boldsymbol{\eta},\boldsymbol{\xi})\,\xi \mathrm{d}\theta \mathrm{d}\xi \mathrm{d}z. \tag{4.52}$$

Which for a homogeneous and isotropic, microelastic peridynamic material is given by:

$$G_0 = 2\int_0^{\delta}\int_z^{\delta}\int_0^{cos^{-1}(\frac{z}{\xi})} B(\boldsymbol{\xi})Cp\frac{s_0^2\xi}{2}\,\xi \mathrm{d}\theta \mathrm{d}\xi \mathrm{d}z. \tag{4.53}$$

Replacing B and Cp by their appropriate expressions for the type of influence function used: uniform or linear, the critical stretch s_0 evaluates to equations 4.54 and 4.55 respectively.

$$s_0 = \sqrt{\frac{4\pi G_0}{9E\delta}}. \tag{4.54}$$

$$s_0 = \sqrt{\frac{5\pi G_0}{9E\delta}}. \tag{4.55}$$

The strain release rate G_0 is a measurable material property. However, in the absence of an experimental measurement for the specific material used, G_0 can be calculated from the mode one stress intensity factor K_I using the following relationship:

$$G_0 = \frac{K_I^2}{E}. \tag{4.56}$$

4.4 Coupled flow-deformation model in 2D

The coupling between the presented peridynamic model for solid mechanics and the peridynamic moisture flow model developed in the previous chapter is possible due to their similar representations of media and mechanisms of interaction. Both represent the medium as a continuum of material points whose positions or moisture contents evolve due to forces or moisture flows that are transmitted via pairwise interactions represented by bonds or peripipes.

In the coupled model, the moisture flow component updates the moisture contents of points in the domain using the available peripipes topology. Changes in moisture contents of interacting points lead to changes in their volumes which creates a stretch s_w in their connecting peripipe. This stretch is passed to the mechanical model where it is added to the mechanical stretch s_m, which is calculated from the displacements of the material points. The combined stretch s (Equation 4.57) is then used to calculate the pairwise forces used to integrate the model forward and update the configuration of the body. Whenever the combined stretch of a bond exceeds the critical stretch of the material, the bond is broken and can no longer transmit neither forces nor moisture.

$$s = s_m + s_w. \tag{4.57}$$

The moisture driven stretch s_w of a bond $\mathbf{x}\mathbf{x}'$ connecting points $\mathbf{x}$ and $\mathbf{x}'$ is calculated as the arithmetic mean of the linear shrinkage values associated with the moisture contents at $\mathbf{x}$ and $\mathbf{x}'$ (Equation 4.58).

$$s_w(\mathbf{x}, \mathbf{x}') = \frac{1}{2}\left(s_w(\theta(\mathbf{x})) + s_w(\theta(\mathbf{x}'))\right). \tag{4.58}$$

where θ is moisture content.

Modifying the damage function μ (Equation 4.50) and the peridynamic equation of motion (Equation 4.51) to include the effect of the moisture caused shrinkage I end up with the following expressions:

$$\rho\ddot{\mathbf{u}}(\mathbf{x},t) = \int_{\mathcal{H}_x} \mu(\boldsymbol{\eta},\boldsymbol{\xi},\mathbf{x},\mathbf{x}')B(\xi)Cp\ \left(S_m(\boldsymbol{\eta},\boldsymbol{\xi}) + s_w(\mathbf{x},\mathbf{x}')\right)\ \frac{(\boldsymbol{\xi}+\boldsymbol{\eta})}{\|\boldsymbol{\xi}+\boldsymbol{\eta}\|}\,\mathrm{d}V_{x'}\ + \mathbf{b}(\mathbf{x},t). \tag{4.59}$$

with:

$$\mu(\boldsymbol{\eta},\boldsymbol{\xi},\mathbf{x},\mathbf{x}') = \begin{cases} 1 & \text{if } \left(S_m(\boldsymbol{\eta},\boldsymbol{\xi}) + s_w(\mathbf{x},\mathbf{x}')\right) < s_0 \\ 0 & \text{otherwise} \end{cases} \tag{4.60}$$

4.5 Numerical implementation in 2D and example simulation

For the numerical implementation of the coupled peridynamic model I made use of an available implementation of the peridynamic model for solid mechanics (Parks et al., 2008) which is an add-on module to LAMMPS (Large-scale Atomic/Molecular Massively Parallel Simulator), an open source parallel molecular dynamics simulator (Plimpton, 1995) written in C++ and used the Message Passing Interface for parallel interprocessor communication. The code was modified to include the logic for the peridynamic moisture flow model. The implementation was then used to simulate a soil restrained ring test. The results of the simulation were compared with those of the actual laboratory experiment reported by Abou Najm et al. (Abou Najm et al., 2009).

4.5.1 Numerical implementation in LAMMPS

Adjustments to LAMMPS included adding additional storage for the state variables and material properties of the flow model. The class that handles force calculations and critical stretch checking was modified to incorporate calculations of moisture flow and the stretch caused by changes in moisture content. Code was also added to the time integration class to calculate changes in moisture content.

In addition, methods that handle input processing, simulation results output, and interprocessor communications were all modified to handle the additional moisture flow model variables and results.

When setting up a two dimensional peridynamic analysis in LAMMPS, the domain discretization is similar to what I used in the flow model implementation in Chapter Two. The domain is represented by nodes placed on a regular grid with spacing Δx. Each point represents an area equal to Δx^2. Associated with each node are the state variables of the mechanical and flow processes: displacement and moisture content.

At the beginning of each timestep, displacements at the nodes are used to calculate the mechanical stretch s_m of the bonds. In addition, moisture contents are used to estimate the soil shrinkage, and to calculate their associated stretch s_w. Both type of stretches are added and compared to the critical stretch s_0. Moisture content values are also used to calculate the flow through the peripipes. Pairwise forces are evaluated using the total stretch and the peridynamic modulus. Bonds that have exceeded s_0 are marked as such and their flow and force contributions are not used. Total forces and flows are summed for each node and passed to the time integration routine.

Time integration of the mechanical model uses a Velocity Verlet Integration scheme. Velocities are updated every half time step, at the middle of a time step using the accelerations and velocities at the beginning of the timestep, and at the end of the timestep using the velocities at the middle of the timestep and the accelerations at the end of the timestep.

$$\dot{\mathbf{u}}_{n+1/2} = \dot{\mathbf{u}}_n + \ddot{\mathbf{u}}_n \frac{\Delta t}{2} \tag{4.61}$$

$$\mathbf{u}_{n+1} = \mathbf{u}_n + \dot{\mathbf{u}}_{n+1/2} \Delta t \tag{4.62}$$

$$\dot{\mathbf{u}}_{n+1} = \dot{\mathbf{u}}_{n+1/2} + \ddot{\mathbf{u}}_{n+1} \frac{\Delta t}{2} \tag{4.63}$$

As for the flow model it uses a naive forward integration scheme. Moisture contents are updated every timestep using previous moisture contents and the current moisture flow.

$$\theta_{n+1} = \theta_n + \dot{\theta}\Delta t. \tag{4.64}$$

The algorithm of the computer code for the coupled peridynamic model is presented in Figure 4.6.

4.5.2 Example simulation

To test the coupled mechanical-Flow peridynamic model I simulated a restrained ring test designed to evaluate the internal mechanical stress created by soil shrinkage due to drying and loss of moisture in the soil sample.

In this test, a ring shaped soil sample placed around a PVC ring is brought to near saturation. When left to dry, the tendency of the soil sample to shrink is opposed by the PVC restraining ring which cause buildup of stresses inside the soil sample (and the ring). As the moisture content of the soil decrease the tensile stresses inside to soil increase until they reach the soil's tensile strength limit and cracking occur (Abou Najm et al., 2009).

An illustration of the restrained ring setup is presented in figure 4.7 (from (Abou Najm et al., 2009)). Readings from the strain gages affixed to the inside surface of the PVC ring are used to continuously measure the hoop strains of the restraining ring, which are used to calculate the tensile and compressive stresses at the inner radius of the soil ring R_{ISoil}. Assuming the soil and the restraining ring are elastic, and using a polar coordinate reference system with the origin at the center of the rings, the tensile tangential stresses and the compressive radial stresses at any point $\mathbf{x} = (r, \theta)$ in the soil is given by the following equations (**?**, Abou Najm et al., 2009):

$$\sigma_\theta(r) = \epsilon E \left(\frac{R_{ORing}^2 - R_{IRing}^2}{2R_{ORing}^2} \right) \left(\frac{R_{ISoil}^2}{R_{OSoil}^2 - R_{ISoil}^2} \right) \left(1 + \frac{R_{OSoil}^2}{r^2} \right). \tag{4.65}$$

```
Read input parameters: geometry, timestep, and mechanical, hydraulic and
  shrinkage properties;
Generate matric head vs moisture content look-up table per soil type;
Generate hydraulic conductivity vs moisture content look-up table per soil
  type;
Generate shrinkage vs moisture content look-up table per soil type;
Generate grid of nodes;
Initialize all node variables to initial conditions;
Generate bonds list;
for t = 1 to Number of time steps do
    Update velocities of nodes (Equation 4.61);
    Update positions of nodes (Equation 4.62);
    Update moisture content of nodes (Equation 4.64);
    for i = 1 to Number of nodes do in parallel
        for all particles j sharing unbroken bond with particle i do
            Look up shrinkage values for nodes i and j;
            Calculate stretch s_θ;
            Calculate stretch s_m using relative displacement;
            Calculate total stretch s;
            Calculate bond force using the stretch;
            Accumulate forces at node i;
            look up matric head of nodes i and j;
            Calculate hydraulic head difference across bond/pipe;
            Calculate change in moisture content at node i due to bond/pipe;
            Accumulate change in moisture content at node i;
            if total stretch s > crtitical stretch s_0 then
                Mark bond of node i with node j as broken
            end
        end
    end
    Update velocities of nodes (Equation 4.63);
    Write results of timestep t to file;
end
```

Fig. 4.6. Implementation algorithm of the coupled peridynamic model. Adapted from (Parks et al.,) and modified to reflect moisture flow component.

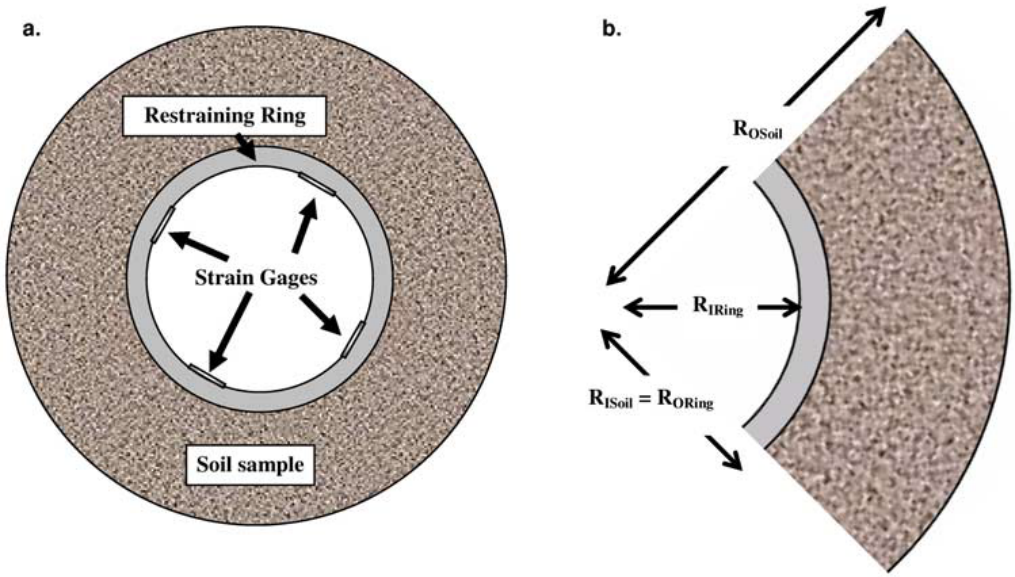

Fig. 4.7. Restrained ring illustration (Abou Najm et al., 2009).

$$\sigma_r(r) = \epsilon E \left(\frac{R_{ORing}^2 - R_{IRing}^2}{2R_{ORing}^2} \right) \left(\frac{R_{ISoil}^2}{R_{OSoil}^2 - R_{ISoil}^2} \right) \left(1 - \frac{R_{OSoil}^2}{r^2} \right). \tag{4.66}$$

where σ_r and σ_θ are the radial and tangential stresses at position r, ϵ is the strain recorded by the strain gages on the inside wall of the restraining ring, E is the restraining ring's Young's modulus, R_{IRing} and R_{ORing} are the inside and outside radii of the restraining ring respectively, and R_{ISoil} and R_{OSoil} are the inside and outside radii of the soil ring.

The dimensions and properties of the experimental setup and the soil used in the experiment are listed in tables 4.2 and 4.3 respectively. The soil volumetric moisture content at the beginning of the test was 44.95%, and cracking occurred at a volumetric moisture content around 35.9% with a maximum tensile stress of $65.9KPa$ located at the inner side of the soil ring. Details of the test procedure, setup and the specific results of the specific experiment used in the following simulation can be found in (Abou Najm et al., 2009).

In the experiment, tracking of the evolution of the moisture content of the soil sample was achieved by continuous measurement of the setup weight using a high

Table 4.2
Setup dimensions and properties (Abou Najm et al., 2009)

Restraining ring material	PVC, schedule 21
Restraining ring Young's modulus (GPa)	2.9
Restraining ring inner radius, R_{IRing} (cm)	1.95
Restraining ring outer radius, R_{ORingt} (cm)	2.11
Soil ring inner radius, R_{ISoil} (cm)	2.11
Soil ring outer radius, R_{OSoil} (cm)	5.30
Soil ring hight (cm)	3.81

Table 4.3
Soil properties (Abou Najm et al., 2009).

Percent sand	15
percent silt	45
Percent clay	40
Soil textural class	clay loam
Water holding capacity (gravimetric)	
at saturation (%)	45.72
at 1/3 bar (%)	32
at 1 bar (%)	24.87
at 15 bar (%)	12.5
Organic matter (%)	4.3
pH	5.7-6.5
CEC	24.1-28.8
Phosphorous (ppm)	88-106 (very high)
Magnesium (ppm)	810-825 (very high)
Potassium (ppm)	215-226 (high)

precision balance to monitor the amount of moisture evaporated. The unrestrained shrinkage behavior of the soil used in the experiment was characterized in another study by Abou Najm (Abou Najm, 2009). Figure 4.8 is the plot of the shrinkage curve as specific volume versus gravimetric moisture content spanning the entire moisture content range.

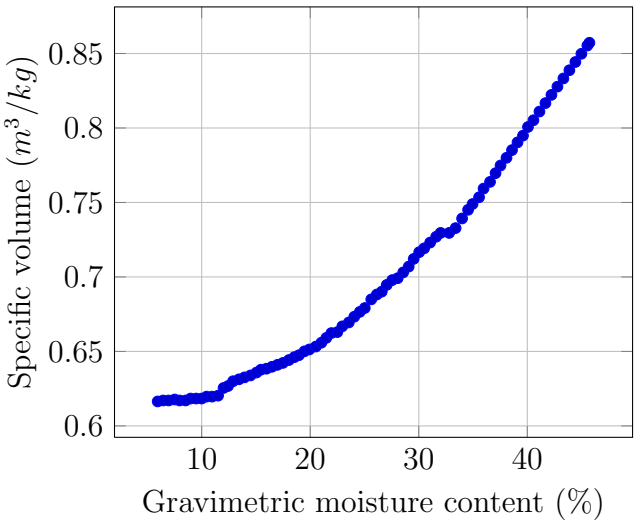

Fig. 4.8. Soil shrinkage curve. Specific volume (m^3/kg) versus gravimetric moisture content (%) (Abou Najm et al., 2009).

Figure 4.9 is also a plot of the shrinkage behavior of the soil plotted as volumetric strain versus volumetric moisture content, with a volumetric strain of zero at saturation.

In addition, because the moisture content at the beginning of the test was below saturation, I recalculated the soil shrinkage curve setting the shrinkage at the starting moisture content to zero. Figure 4.10 is a plot of the linear shrinkage versus the volumetric moisture content.

For the peridynamic model, I used a horizon $\delta = 0.004m$, a grid size $\Delta x = 0.001m$, and I opted for a uniform influence function. Nodes were generated inside a circular region with an inner radius of $0.017m$ and an outer radius of $0.053m$. Nodes falling between $0.017m$ and $0.021m$ were not allowed to move in order to

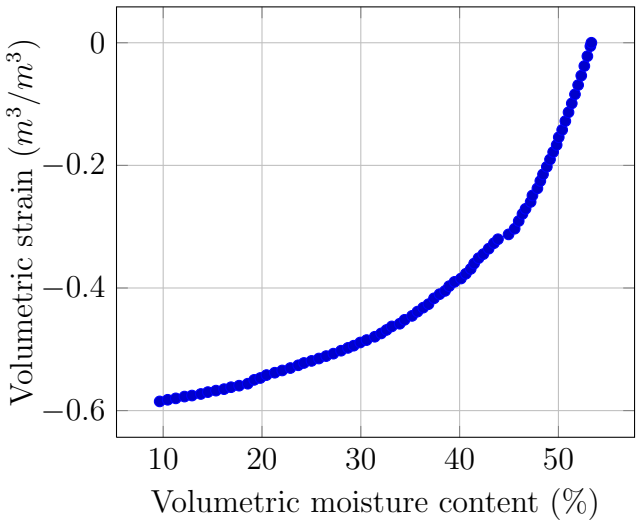

Fig. 4.9. Soil shrinkage curve. Volumetric strain (m^3/m^3) versus volumetric moisture content (%).

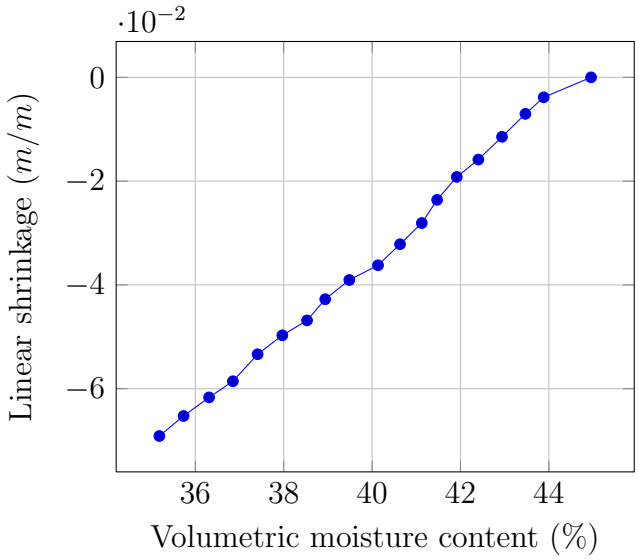

Fig. 4.10. Soil shrinkage curve. Linear shrinkage (m/m) versus volumetric moisture content (%).

simulate the rigid restraining ring. I used a small timestep of $7.5 \times E^{-7} sec.$ to accommodate the timescale of the mechanical process. I also introduced a normal noise with a standard deviation equal to 0.05 to the pairwise forces to simulate

natural imperfections and provide the medium with crack nucleations sites. Moisture content was set to the initial value of 44.95% volumetric and reduced at regular intervals to simulate evaporation until failure occurred. Due to the difference in timescales between the mechanical and the moisture flow process, the moisture content was changed every $1 \times E^5$ timesteps to allow the kinetic energy to drain and the model to reach mechanical equilibrium. To calculate the stretch caused by moisture, I used the data presented in Figure 4.10. Table 4.4 lists the parameter values used in the peridynamic simulation.

Two important properties that are required for the simulation are still required: the soil's Young modulus, and the critical stretch. The Young's modulus was using a finite element simulation, and the critical stretch was calculated using its relationship the the strain energy release rate.

The estimation of the Young's modulus proceeded as follows. Using the value of the shrinkage that corresponds to the moisture content at failure I scaled the dimensions of the soil ring accordingly. I then applied a Dirichlet boundary condition to the inner boundary of the soil ring with a positive radial displacement value that would bring the inner radius of the ring to its original value. I then iteratively searched for the value of the Young's modulus that would result in a tangential tensile stress that matches the value of the stress at failure in the experiment. This value turned out to be around $1200KPa$.

For a two dimensional peridynamic model using a uniform influence function, the peridynamic elastic modulus is calculated using the appropriate equation from table 4.1 and setting ν to 1/3 for plane stress and the horizon radius δ to $0.004m$:

$$\begin{aligned} C_p &= \frac{6E}{\pi(1-\nu)\delta^3} \\ &= 5.38e13kPa/m^3. \end{aligned} \tag{4.67}$$

To estimate the critical stretch s_0 I used the following equation from fracture mechanics:

$$K_I = \sigma_t\sqrt{(\pi l)}. \tag{4.68}$$

Table 4.4
Peridynamic simulation parameters

Horizon radius (δ)	$0.004m$
Grid size (Δx)	$0.001m$
Peridynamic modulus (C_p)	$5.38E10kPa/m^3$
Critical stretch (s_0)	0.057

where K_I is the mode one stress intensity factor, σ_t is the tensile stress perpendicular to the crack, and l is the length of the crack.

I know that at failure $\sigma_t = 65.9KPa$. I also know that $\Delta x = 0.001m$, which I considered as the length of the crack at crack nucleation $l = 0.001m$. Plugging in these values in equation 4.68 I get:

$$\begin{aligned} K_I &= \sigma_t \sqrt{(\pi l)} \\ &= 65.9E3\sqrt{(0.001\pi)} \\ &= 3.69KPa.m^{0.5}. \end{aligned} \tag{4.69}$$

I then use the relationship between strain energy release rate and K_I (Equation 4.56) and calculated G_0:

$$\begin{aligned} G_0 &= \frac{K_I^2}{E} \\ &= 11.35m^{0.5}. \end{aligned} \tag{4.70}$$

from that I calculated s_0 using Equation 4.54:

$$\begin{aligned} s_0 &= \sqrt{\frac{4\pi G_0}{9E\delta}} \\ &= 0.057. \end{aligned} \tag{4.71}$$

Figure 4.11 is a comparison of tangential tensile stresses σ_θ between the laboratory experiment and the peridynamic model. The stresses reported are at $r = 0.022m$, the inner radius of the soil sample. I observe an excellent agreement

between the model and the experimental results in the moisture content and stress at failure, they both fail at a moisture content value of 36.2% and at a tensile stress value of $61.5kPa$. Despite some deviations, there is an acceptable agreement in the evolution of the stress with decreasing moisture content. The observed deviations are due to the assumption of linear elasticity in modeling the soil which produced a straight line until cracking; whereas the experimental data exhibit a slight hardening which is expected as the elastic modulus of soils usually increases with decreasing moisture content, a feature that is not in the current implementation of the model and that I am planning on including in future work.

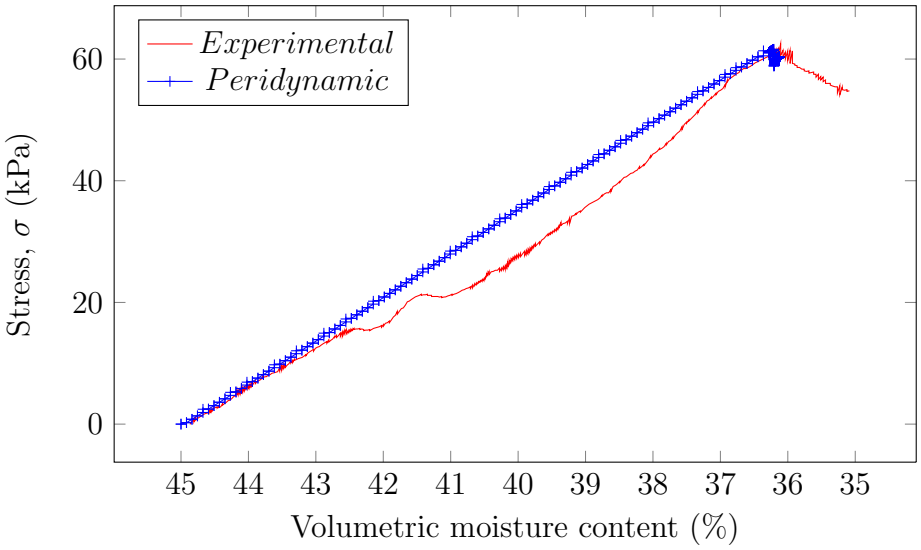

Fig. 4.11. Tensile stress versus moisture content at inner radius of restrained ring. Experimental data in red, simulation results in blue.

Figure 4.12 is a comparison between the experimental results and the peridynamic model of the tangential tensile stress σ_θ at failure between $r = 0.022m$ and $r = 0.053m$. Here I also observe a good agreement between the experiment and the peridynamic model. Figure 4.13 is a plot of the experimental data for the tensile stress versus the simulation results, a linear least square analysis yielded an $r^2 = 0.9679$. The differences observed towards the outer boundary of the soil in Figures 4.12 and 4.12 are caused by the way stress is calculated in the peridynamic

model. According to Equation 4.46, the stress is calculated over an entire horizon; however, points that are located less than a horizon radius away from a boundary have incomplete horizons, leading to inaccuracies in the values of the calculated stress near the boundary.

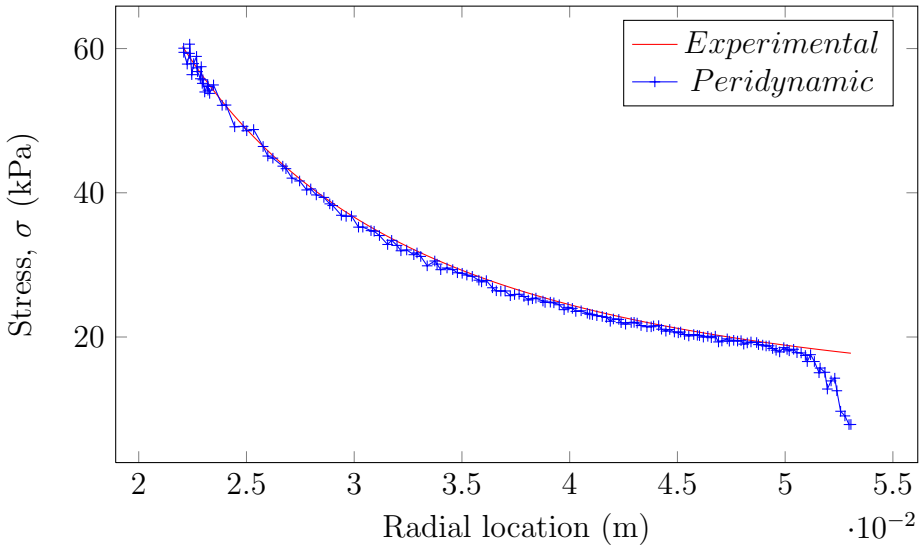

Fig. 4.12. Tensile stress versus radial position at the onset of failure of restrained ring. Experimental data in red, simulation results in blue.

Figure 4.14 shows the evolution of the crack from its onset. The color code is an indication of damage, where a damage of zero indicates no damage at all, and an index of 0.5 indicates that half of the bonds connected to a point have been severed. Points lying on the surface of a crack should have a damage index equal to 0.5. I observe that at the start of the cracking process, the majority of the points that fall on what will obviously become a crack surface have a damage lower than 0.5, and as the crack develops they eventually reach a value of 0.5. This behavior is expected because the bonds connecting points one side of the crack to points on the other side do not necessarily reach their critical stretch at the same time.

Figure 4.15 shows the evolution of the tangential tensile stress with the progression of the cracking process. Here I can observe the expected drop of the

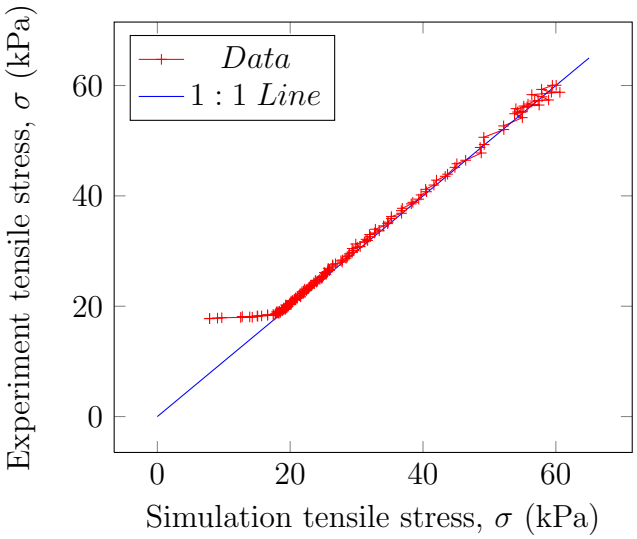

Fig. 4.13. Plot of the experimental versus simulation tangential tensile stress between $r = 0.022m$ and $r = 0.053m$.

tensile stress behind the crack tip, and the concentration of stress ahead of the crack which was an implicit result of the simulation.

In both figures, I also observe that the crack did not develop and evolve in a perfect radial direction. Instead, the crack shows a deviation from the radial direction and a slight change in direction observable in the middle panels. This is mainly due to the normal noise I added to the pairwise forces in order to mimic the slight variabilities and small imperfections in the soil mechanical properties. These variations will result in cracks deviating from the radial direction and occasionally changing direction. Figure 4.16 is an image showing two restrained ring tests post-failure, where I can observe cracks that deviate from the radial direction.

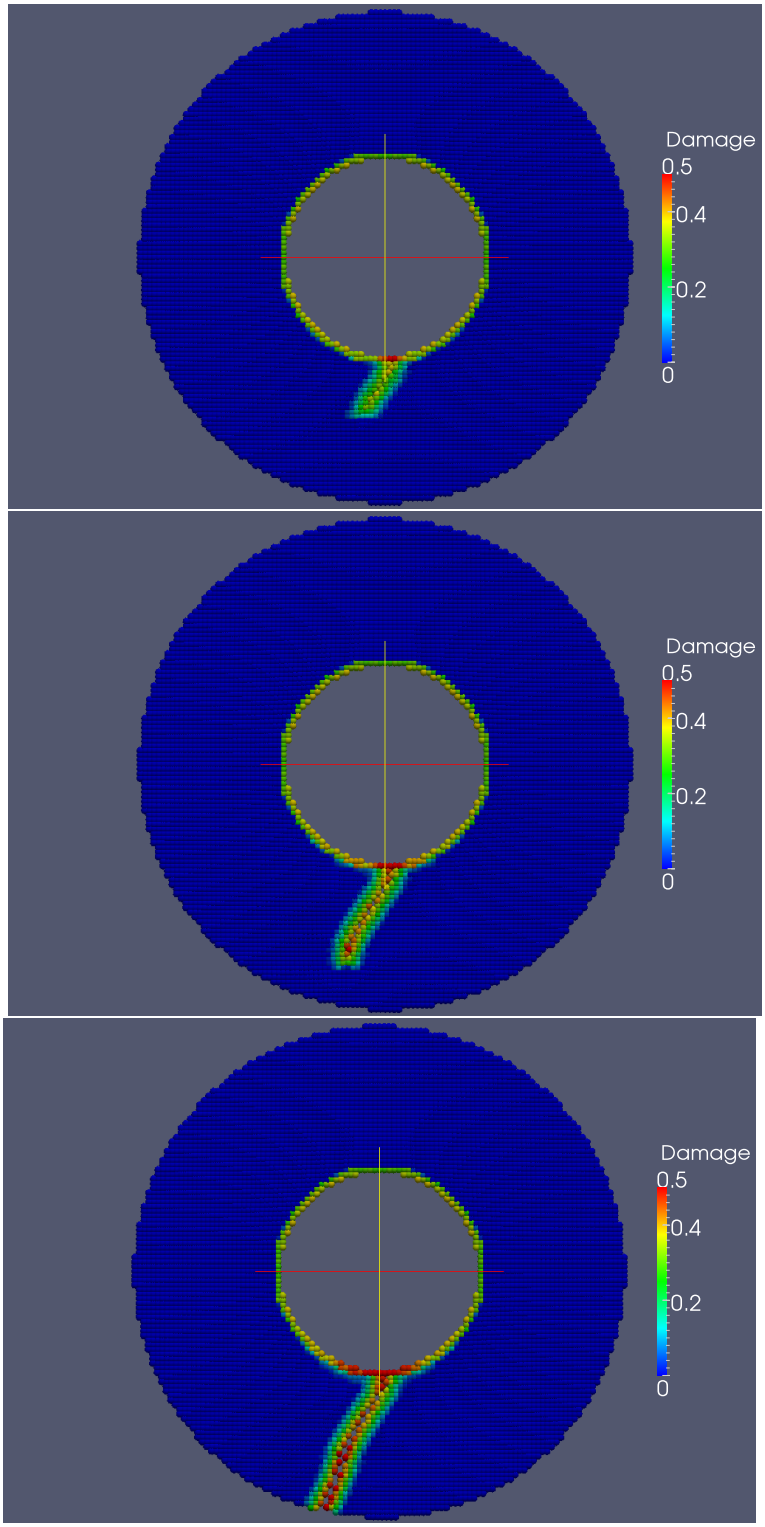

Fig. 4.14. Peridynamic simulation results. Damage index during crack evolution.

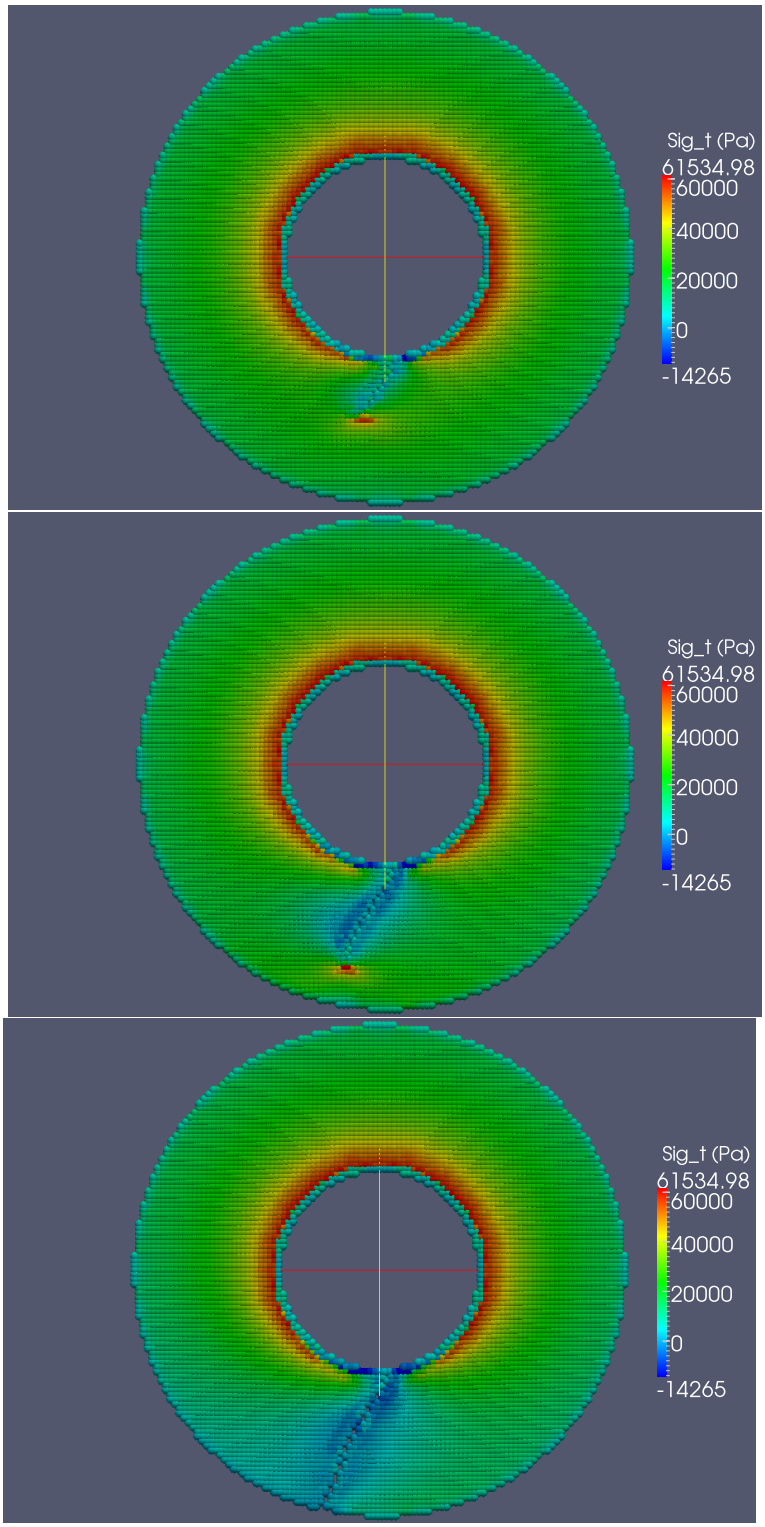

Fig. 4.15. Peridynamic simulation results. Tangential tensile stress during crack evolution (Pa).

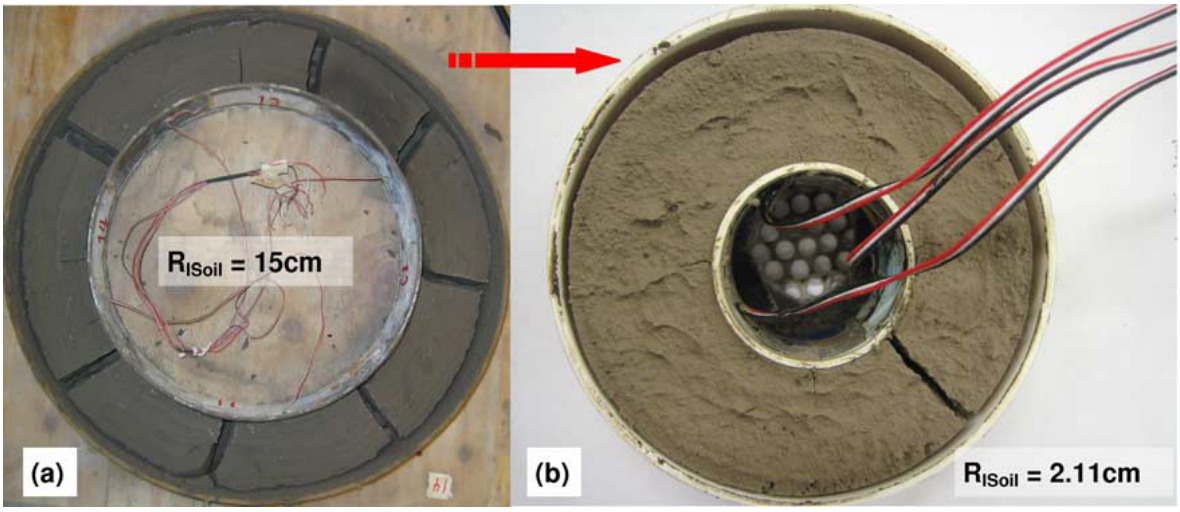

Fig. 4.16. Cracking patterns in two restrained ring tests (Abou Najm et al., 2009).

4.6 Conclusion

In this study, I built upon the peridynamic moisture flow model that I developed earlier and merged it with the peridynamic model for solid mechanics (Silling, 2000, Silling et al., 2010). The resultant coupled model is designed to integrate the effects of the soil volumetric strains that are caused by changes in moisture content into the mechanical submodel to simulate the nucleation and evolution of dessication cracks which are a feature of soils with a high shrink/swell potential.

Using the derived model, I simulated a soil restrained ring test and compared the results with actual experimental results (Abou Najm et al., 2009).

When conducting a restrained ring test, a ring of soil, near or at saturation, is allowed to dry while restraining the movement of its inner surface using a rigid pipe. This results in the buildup of internal stresses with decreasing moisture content until soil failure occurs. Stresses at the interface between the soil and the pipe are recorded using a strain gage placed on the inner wall of the pipe, and are used to calculate the stresses within the soil by assuming elastic behavior. The evolution of moisture content is captured by measuring the amount of evaporated water by placing the setup on a precision balance.

The coupled peridynamic model successfully predicted the values of moisture content and tensile stress at failure at the inner radius of the soil ring, and an excellent agreement of the tensile stress diagrams between the simulation results and the experimental data ($r^2 = 0.9679$).

4.7 References

Abou Najm, M., Mohtar, R. H., Weiss, J., and Braudeau, E. (2009). Assessing internal stress evolution in unsaturated soils. *Water Resources Research*, 45(5):n/a–n/a.

Abou Najm, M. R. (2009). Soil-water interaction: Lessons across scales. *ETD Collection for Purdue University*, pages 1–257.

Bobaru, F. and Duangpanya, M. (2010). The peridynamic formulation for transient heat conduction. *International Journal of Heat and Mass Transfer*, 53(19–20):4047–4059.

Bobaru, F. and Hu, W. (2012). The meaning, selection, and use of the peridynamic horizon and its relation to crack branching in brittle materials. *International Journal of Fracture*, 176(2):215–222.

Emmrich, E. and Weckner, O. (2007). On the well-posedness of the linear peridynamic model and its convergence towards the navier equation of linear elasticity. *Communications in Mathematical Sciences*, 5(4):851–864. Mathematical Reviews number (MathSciNet): MR2375050; Zentralblatt MATH identifier: 1133.35098.

Foster, J. T. (2009). Dynamic crack initiation toughness: Experiments and peridynamic modeling. *ETD Collection for Purdue University*, pages 1–165.

Ha, Y. D. and Bobaru, F. (2010). Studies of dynamic crack propagation and crack branching with peridynamics. *International Journal of Fracture*, 162(1-2):229–244.

Kilic, B. and Madenci, E. (2010). Peridynamic theory for thermomechanical analysis. *Advanced Packaging, IEEE Transactions on*, 33(1):97 –105.

Lehoucq, R. and Silling, S. (2008). Force flux and the peridynamic stress tensor. *Journal of the Mechanics and Physics of Solids*, 56(4):1566–1577.

Parks, M. L., Lehoucq, R. B., Plimpton, S. J., and Silling, S. A. (2008). Implementing peridynamics within a molecular dynamics code. *Computer Physics Communications*, 179(11):777–783.

Parks, M. L., Seleson, P., Plimpton, S. J., Lehoucq, R. B., and Silling, S. A. Peridynamics with lammps: A user guide v0. 2 beta.

Plimpton, S. (1995). Fast parallel algorithms for short-range molecular dynamics. *Journal of Computational Physics*, 117:1–19.

Seleson, P. and Parks, M. (2011). On the role of the influence function in the peridynamic theory. *International Journal for Multiscale Computational Engineering*, 9(6):689–706.

Silling, S. (2000). Reformulation of elasticity theory for discontinuities and long-range forces. *Journal of the Mechanics and Physics of Solids*, 48(1):175–209.

Silling, S. and Askari, E. (2005). A meshfree method based on the peridynamic model of solid mechanics. *Computers & Structures*, 83(17–18):1526–1535.

Silling, S., Epton, M., Weckner, O., Xu, J., and Askari, E. (2007). Peridynamic states and constitutive modeling. *Journal of Elasticity*, 88(2):151–184.

Silling, S., Lehoucq, R., Aref, H., and van der Giessen, E. (2010). Peridynamic theory of solid mechanics. In *Advances in Applied Mechanics*, volume Volume 44, pages 73–168. Elsevier.

Silling, S. A. and Lehoucq, R. B. (2008). Convergence of peridynamics to classical elasticity theory. *Journal of Elasticity*, 93(1):13–37.

Simunek, J., Sejna, M., and Van Genuchten, M. (2005). The HYDRUS-1D software package for simulating the one-dimensional movement of water, heat, and multiple solutes in variably-saturated media. *University of California, Riverside, Research reports*, 240.

Weiss, W., Yang, W., and Shah, S. (1998). Shrinkage cracking of restrained concrete slabs. *Journal of Engineering Mechanics*, 124(7):765–774.

CHAPTER 5. RESEARCH OUTCOMES AND FUTURE WORK

5.1 Research outcomes

In this research, I developed a model for transient moisture flow in unsaturated soils valid at every point in the computational domain regardless of discontinuities. This peridynamic flow model was coupled with the peridynamic model for solid mechanics to simultaneously model moisture flow processes and mechanical deformation and cracking processes in unsaturated soils. I have therefore, met both objectives that I set for my project.

Concerning the peridynamic flow model, my first objective, I developed expressions for the peridynamic hydraulic conductivity as a function of the horizon radius and the classic measurable hydraulic conductivity for isotropic and anisotropic soils, as well as expressions for moisture flux and flow power. All equations were derived for models with a uniform, or constant, influence function, and for models with a linear, or triangular, influence function.

Validation of the model was carried out by comparing peridynamic simulations results to results using a classic flow model. The simulations covered infiltration and drainage in a one dimensional homogeneous soil column, horizontal moisture redistribution in a horizontal two dimensional homogeneous soil with isotropic and anisotropic hydraulic conductivity, and vertical drainage in a two dimensional homogeneous and heterogeneous soil with isotropic and anisotropic soil.

For the infiltration scenarios, I used the depth of the infiltration front as a benchmark variable; for all other scenarios I used the moisture content. I found excellent agreement between the results of the peridynamic and classic models, where, after selecting an adequate horizon radius (δ) and point density (m), the

relative difference of the variables of interest between the two models did not exceed 1.0% for all the simulated scenarios.

As part of the validation of the model in one dimension, I performed a model sensitivity analysis to the values of the horizon radius and the horizon point density. I found that the relative difference is inversely proportional to the horizon radius, which is expected given that at the limit of vanishing horizon the peridynamic model equation converges to the classic flow equation. On the other hand, the relative difference is directly proportional to the horizon point density, also expected, since the state of the horizon is captured more accurately with a larger number of points. There is no reason to expect a different trend for models in two and three dimensions.

In my work I found that the type of influence function may have an impact on the performance of the model. Using a linear function could lead to a reduction of the relative error obtained when using a uniform function. however, This finding is not problematic since a linear function gives a higher weight to shorter interactions bringing the model closer to being local than non-local.

For my second objective, I presented the bond based peridynamic model of solid mechanics, including the derivation of the peridynamic equation of motion, going into detail about the simple case of a homogeneous, isotropic, and linear elastic material. The derivation of the expressions for the deformation energy density and the mechanical stress, and of the relationship between the peridynamic elastic modulus and Young's modulus were presented, in addition to how damage is modeled and represented using the concept of bond critical stretch.

The coupled model was implemented by incorporating the code for the peridynamic flow model into an existing implementation of the bond based peridynamic model, which is an add-on module to the open source parallel molecular dynamics simulator LAMMPS (Large-scale Atomic/Molecular Massively Parallel Simulator) (Plimpton, 1995, Parks et al., 2008).

The validation of the coupled model was carried out by simulating a laboratory soil restrained ring test reported in (Abou Najm et al., 2009, Abou Najm, 2009) and comparing the results. I found that the coupled model successfully predicted the values of moisture content and tensile stress at the onset of failure, and an excellent agreement of the tensile stress diagrams between the simulation results and the experimental data ($r^2 = 0.9679$).

5.2 Future work

While conducting this project, and after evaluating the research outcomes and the results of the simulations, I identified five areas of improvement that I consider of high priority to improve my confidence in the proposed model's validity and increase its versatility.

5.2.1 Calculation of the peridynamic hydraulic conductivity

The calculation of the peridynamic hydraulic conductivity assumes a full horizon. However, points located at a distance less than half a horizon radius away from a boundary have incomplete horizons. Using the derived expression for the hydraulic conductivity at these points leads to inaccurate moisture exchange values. This is clearly evident in the results of the drainage scenarios in Chapter 2, where the maximum errors are located at or near the top boundary. Although the resultant differences have no consequence on my simulations ($< 0.2\%$), I need to generalize the expression of the peridynamic hydraulic conductivity to be valid at points with incomplete horizons.

5.2.2 Boundary conditions

In my infiltration simulations I assumed a soil controlled infiltration scenario, and the boundary condition was applied as a constant moisture content equal to

saturation. However, for rain controlled infiltration or evaporation scenarios, a rate boundary condition needs to be applied, which I did not derive and is still a pending matter.

5.2.3 Infiltraction post cracking

Another important aspect of modeling moisture flow in soils that I did not address in this research is infiltration post cracking, where cracks connected to the surface become preferential flow paths towards deeper soil layers. If my model is to develop into a useful tool, I need to include this capacity. This requires the implementation of a method to automatically represent coalescing cracks and detect those that are connected to the surface.

5.2.4 Moisture dependent mechanical properties

When modeling the restrained ring experiment, I used a linear model for the soil elastic modulus that is independent from the moisture content. However, soil stiffness usually exhibits a dependence on moisture, increasing with decreasing moisture content. The impact of this assumption can be observed in Figure 4.11 where the plot of the experimental results exhibits a positive curvature whereas the plot of the simulated results exhibits a linear trend. In addition, the tensile strength of the soil is also dependent on the moisture content, a characteristic that I ignored since I knew beforehand the location of the failure point in the moisture content-tensile stress plane for the specific ring geometry modeled. In order to model more general scenarios, I need to modify the model to include a dependence of the mechanical properties on the moisture content.

5.2.5 Experimental data

In addition, to further evaluate the model, I need to conduct experiments of moisture flow in cracking soil with well characterized mechanical and hydraulic properties to produce detailed and reliable data about the progress of the moisture flow and mechanical processes simultaneously.

5.3 References

Abou Najm, M., Mohtar, R. H., Weiss, J., and Braudeau, E. (2009). Assessing internal stress evolution in unsaturated soils. *Water Resources Research*, 45(5):n/a–n/a.

Abou Najm, M. R. (2009). Soil-water interaction: Lessons across scales. *ETD Collection for Purdue University*, pages 1–257.

Parks, M. L., Lehoucq, R. B., Plimpton, S. J., and Silling, S. A. (2008). Implementing peridynamics within a molecular dynamics code. *Computer Physics Communications*, 179(11):777–783.

Plimpton, S. (1995). Fast parallel algorithms for short-range molecular dynamics. *Journal of Computational Physics*, 117:1–19.

VITA

VITA

Rami was born in Tripoli, Lebanon. He earned his B.E. and M.E. in Civil Engineering from the American University of Beirut (AUB) in 1996 and 1998 respectively.

After graduating, the author worked in the sectors of construction and microfinance. Between 2003 and 2004, Rami was a predoctoral fellow at the Fineberg School of Medicine at Northwestern University where he worked on research related to chronic pain. In 2005, he returned to Lebanon and worked in social and economic development in both the public and private sectors, and was an instructor at the departments of Civil and Environmental Engineering, and Mechanical Engineering at AUB. In 2008, Rami joined the department of Agricultural and Biological Engineering at Purdue University.